UNIVERSITY OF LIVERPOOL

High Spin Studies of ^{156}Er and ^{130}Ce

by

Masood Akmali

Thesis submitted in accordance with the requirements of the University of Liverpool for the degree of Doctor of Philosophy

Oliver Lodge Laboratory

May 2010

Abstract

The high spin structure of the two rare-earth nuclei ^{156}Er and ^{130}Ce have been studied using the fusion-evaporation reactions. At the highest values of angular momentum ^{156}Er undergoes a Coriolis-induced shape transition from a deformed (prolate) state of collective rotation to a non-collective (oblate) configuration. Several weak high energy γ-rays have been newly identified feeding the terminating state in ^{156}Er. The high-lying levels from which these γ-rays arise are predicted to represent weakly deformed core-breaking configurations involving energetically expensive 1-particle-1-hole and 2-particle-2-hole proton excitations across the spherical Z = 64 shell gap. In the case of ^{130}Ce, through quadruples analysis (γ^4) of the data several bands have been identied for the first time and the previously reported structures have been extended to high spin. Nucleonic congurations for the newly observed structures have been suggested on the basis of comparison with Cranked Nilsson-Strutinsky and with a geometrical model (the semi classical model of Dönau and Frauendorf).

Acknowledgements

به نام خالق یکتا

دل هر ذره که بشکافی آفتابیش در میان بینی

I would like to thank Prof. P.J. Nolan for all his support throughout my four years as a PhD student, Dr Eddie Paul for his often puzzling but profound answers to my naive questions, Dr. John Cresswell, Janet Sampson and Mark Norman for all their support in computing. Last, but not least, my long suffering parents and my wife for all their support both financially and emotionally and for being there when I've needed them. Without these people the writing of this thesis would not
have been possible.

Thank you . . .

Contents

Abstract i

Acknowledgements ii

List of Figures vi

List of Tables xi

1 Introduction 1

2 Nuclear Models 2
- 2.1 Introduction . . . 2
- 2.2 The Spherical Shell Model . . . 3
- 2.3 Nuclear Deformation . . . 5
- 2.4 The Anistropic Harmonic Oscillator Potential . . . 6
- 2.5 The Nilsson Model . . . 8
- 2.6 The Strutinsky shell Correction Procedure . . . 11
- 2.7 Pairing . . . 12
- 2.8 Quasi particles . . . 13

3 Nuclear Rotation 14
- 3.1 Introduction . . . 14
- 3.2 Non-Collective single Particle Excitation . . . 14
- 3.3 Collective Rotation . . . 15
- 3.4 Moment of Inertia . . . 17
- 3.5 The Coriolis Anti-Pairing (CAP) Effect . . . 18
  - 3.5.1 The Cranking model . . . 19
- 3.6 Nuclear Symmetries . . . 20

4 Experimental Details 22
- 4.1 Introduction . . . 22
  - 4.1.1 Heavy Ion Fusion Evaporation Reaction . . . 22
- 4.2 Gamma Decay . . . 25
- 4.3 DCO Analysis . . . 26
- 4.4 Gamma Interaction With Matter . . . 26

4.5 High-Purity Germanium (HPGe) Detectors 27
4.5.1 Compton Suppression 27
4.5.2 Bismuth Germanate (BGO) Detectors 28

5 High Spin study of ^{156}Er **30**
5.1 Introduction 30
5.2 Motivation 30
5.3 The Experimental Details 32
5.4 ^{156}Er Results 33
5.5 Low Spin Structure 33
5.5.1 Band 1 (+,0) 33
5.5.2 Band 2 (-,1) 36
5.5.3 Band 3 (-,1) 37
5.5.4 Band 4 (-,1) 37
5.5.5 Band 5 (+,1) 38
5.6 High Spin Structure 40
5.6.1 Band 1 (0,+) 40
5.6.2 Band 2 (-,1) 43
5.6.3 Band 3 (-,0) 43
5.6.4 Band 4 (-,1) 45
5.7 Discussion 45
5.7.1 Introduction 45
5.7.2 Band 1, (+,0) 46
5.7.3 The Side Bands 50
5.7.4 Beyond Band Termination State 52
5.7.5 Conclusion 52

6 High Spin study of ^{130}Ce **54**
6.1 Introduction 54
6.1.1 Experimental Details 55
6.2 Data Analysis Techniques 56
6.3 Experimental Results 58
6.3.1 The ΔI=2 bands 58
6.3.2 Ground state band(+,0) 58
6.3.3 Band 11- the gamma band(+,0) 65
6.3.4 Band 10 (-,1) 67
6.3.5 Band 9 (-,0) 67
6.4 ΔI=1 bands 67
6.4.1 Bands 5 and 6 (-,0) 67
6.4.2 Bands 7 and 8 (-,0) 70
6.4.3 Bands 1 and 2 (+,0) 78
6.4.4 Bands 3 and 4 (+,0) 79

7 Discussion of ^{130}Ce Results **83**
7.1 Introduction 83

7.2 ΔI=2 bands 84
7.2.1 Ground state band GSB 86
7.2.2 The Band 11- the Gamma Band 88
7.2.3 The Band 9 and 10 88
7.3 ΔI=1 bands 88
7.3.1 The Bands 5 and 6 88
7.3.2 The Bands 7 and 8 89
7.3.3 The Bands 1 and 2 92
7.3.4 The Bands 3 and 4 93
7.3.5 Electromagnetic Transitions Strengths 93
7.3.6 Conclusion 98

Bibliography **99**

List of Figures

2.1 An illustration of three potential wells used to model the nuclear potential. V_0 is the well depth, r the distance from the origin and r_o the nuclear radius 3

2.2 The Lund convention for nuclear shapes. The parameters β_2 and γ are, respectively, measures the elongation of the axially symmetric shape and triaxiality, taken from [1]. 7

2.3 Nilsson diagram of single-neutron energies (50$\leq$ N $\leq$82). Full and dashed lines corresponds to positive and negative parity orbitals respectively[2]. 9

2.4 Nilsson diagram of single-proton energies (50$\leq$ Z $\leq$82) . Full and dashed lines corresponds to positive and negative parity orbitals respectively[2]. 10

2.5 Two identical nucleons in time-reversed orbits,(a), scattering into new time- reversed orbits,(b).[3]. 13

3.1 A deformed nucleus rotating about an axis perpendicular to the symmetry axis and its angular momentum projections 15

3.2 Single particle and collective modes of excitation [3] 15

3.3 Particle coupling scheme; Deformations aligned (a) and Rotational alignment(b) 19

4.1 Schematic illustration of different impact parameters b, (assuming projectile nucleus has negligible size). 23

4.2 The modes of de-excitation of a compound nucleus following a heavy-ion fusion evaporation reaction [1]. 24

4.3 Schematic diagram of an escape-suppressed HPGe detector as used in the Gammasphere arrays. [1]. 28

4.4 Spectra obtained using the escaped-suppressed Ge detector of the Gammasphere array for 1173 and 1332 keV γ-rays of ^{60}Co 29

5.1 Typical measured DCO ratio values, in order to validate the result some of the previously know γ rays are also included such as 291, 688 keV. 34

5.2 Low spin part of the level scheme for ^{156}Er illustrating the states below spin 30$\hbar$. Transition Energies are given in keV and the width of the arrows is proportional to the intensity of the γ rays 35

5.3 Spectrum illustrating the 924, 946 and 957 keV transitions feeding in 16, 18 and 20$\hbar$ states in band 1(x=781 y=544 z=522 keV). . . . 36
5.4 The spectrum illustrating the 560, 586, 557, 521 and 460 keV transitions feeding in 18$\hbar$ and 20$\hbar$ states in band 1(x= 687 y=675 z=682 keV). . . . 37
5.5 The spectrum illustrating the 875 keV transition in band 3(x= 639 y=570 z=704 keV). . . . 38
5.6 The spectrum illustrating the 235 and 422 keV transitions decaying into 24^- and 28^- states of band 3(x= 704 y=761 z=682 keV). . . . 38
5.7 The spectrum illustrating the 306 keV transition decaying from 22^+ into the 21^- state in band 2(x= 781 y=536 keV). . . . 39
5.8 High spin part of the level scheme for ^{156}Er illustrating the states above spin 30$\hbar$. Transition Energies are given in keV and the width of the arrows is proportional to the intensity of the γ rays. . . . 41
5.9 The spectrum illustrating three newly identified transitions feeding into 42^+ transitions in band 1. The part of the spectrum is magnified in order to illustrate the the transitions beyond terminating state(x= 218, y= 720, z= 799,664,682). . . . 42
5.10 The spectrum illustrating the new γ-rays at energies of 917 keV in band 1(x= 773 y=765 z=799 keV). . . . 43
5.11 The spectrum illustrating the new γ ray at energy of 1081 keV ($33^- \rightarrow 31^-$) in band 2(x= 735 y=689 z=908 keV. . . . 44
5.12 The spectrum illustrating the new γ-ray at energy of 668 keV in band 3(triple gated spectrum of list of gates including all clean gates from band 3) . . . 44
5.13 The spectrum illustrating the new γ rays at energy of 1214 and 1048 keV in band 4(x= 596 y=742 z=895 keV). . . . 45
5.14 Calculated states in the yrast region of ^{156}Er with the configuration terminating at 42^+ specially marked (double circled). The calculated aligned states and the corresponding observed states are encircled. Two circles are used for the calculated fully aligned states. The plot is taken from [4]. . . . 47
5.15 Experimental rigid rotor versus spin, I$\hbar$ (top) and alignment ,i versus rotational frequency $\hbar\omega$ for the bands in ^{156}Er. The band crossing which is illustrated in the bottom plot corresponds to first $i_{13/2}$ neutron crossing. The Harris parameters of J_0= 15 MeV^{-1} $\hbar^2$ and J_1= 90 MeV^{-3} $\hbar^4$ have been used. . . . 48
5.16 Experimental rigid rotor plot of bands in ^{156}Er deduced through current work (left) and the experimental rigid rotor plot of positive parity bands in ^{156}Er and ^{154}Dy (right) in the I$\geqq$30 spin region is depicted in Figure. One can observe the striking similarities beween two isotones, the plot is taken from [5]. . . . 50

5.17 Experimental alignment, i versus rotational frequency $\hbar\omega$ for the negative parity bands in ^{156}Er. The band crossing which is illustrated in the plot corresponds to first $i_{13/2}$ neutron crossing. The Harris parameters of J_0= 15 MeV^{-1} $\hbar^2$ and J_1= 90 MeV^{-3} $\hbar^4$ have been used. 51

6.1 Typical measured DCO ratio values from the investigation, in order to validate the result some of the previously know γ rays are also included. 57
6.2 The level scheme for ^{130}Ce . Transition Energies are given in keV and the width of the arrows is proportional to the intensity of the γ rays 59
6.3 The triple gated spectrum (x = 730, y = 615 and z = 458) illustrating the new γ ray at energy of 994 keV in ground state band 60
6.4 The double gated spectrum (x = 267 and y = 550) illustrating the new γ rays at energy of 994 and 236 keV in ground state band. . . . 60
6.5 Sum-of-Triple-gates spectrum, gated on each of the transitions illustrating the band 11(gamma band). 66
6.6 The double gated spectrum (x = 664 and y = 488) illustrating the new γ ray at energy of 728 keV in the band 11. 66
6.7 The double gated spectrum (x = 359 and y = 448) illustrating the newly found band 10. 68
6.8 The triple gated spectrum (x = 448, y = 359 and z = 776) illustrating the newly found band 10. 69
6.9 The double gated spectrum (x = 708 and y = 593)illustrating the new γ rays at in the band 10 including the 183 keV γ ray. 69
6.10 The double gated spectrum (x = 991 and y = 837)illustrating the new γ ray energy of 1026 keV. 70
6.11 The double gated spectrum (x = 708 and y = 428)illustrating the new γ rays at energy of 465 kev. 70
6.12 The double gated spectrum (x = 264 and y = 428)illustrating the newly found γ rays in the band 9. 71
6.13 The triple gated spectrum (x = 699, y = 722 and z = 428)illustrating the newly found γ rays in the band 9. 72
6.14 The double gated spectrum (x = 810 and y = 612)illustrating the newly found γ rays in the band 9. 72
6.15 Sum-of-Triple-gated spectra, gated on each of the transitions in band 9 illustrating the newly found γ rays in the band 9. 73
6.16 The triple gated spectrum (x ,y = list of γs in band 5 and z = 1187) illustrating the newly found γ ray at energy of 1258 keV in band 5. 74
6.17 The triple gated spectrum (x ,y = list of γs in bands 5 and 6 and z = 1232) illustrating the newly found γ ray at energy of 1341 keV in band 6. 75
6.18 The triple gated spectrum (x =531 and y = 498) illustrating the newly found γ rays at energy of 587 keV in band 5. 76

6.19 Sum-of-Triple-gated spectrum, gated on transitions each of the transitions in band 8 illustrating the newly found γ rays at energy of 1205 and 1219 keV in band 8. 77
6.20 The triple gated spectrum (x = 264 and y = 428) illustrating the newly found γ rays at energy of 323 and 1350 keV in band 7. 78
6.21 The double gated spectrum (x = 323 and y = 264) illustrating the newly found γ ray at energy of 1350. 78
6.22 Sum-of-Triple-gates spectrum, gated on each of the transitions in band 7(below 20$\hbar$) illustrating the newly found γ rays at energy of 962,1068,1140 and 1196 keV in band 7. 79
6.23 The double gated spectrum (x = 323 and y = 264) illustrating the newly found γ rays belonging to four four-quasiparticle configurations 1 and 2 (top panel) and 3 and 4 (bottom panel). 80
6.24 The double gated spectrum (x = 320 and y = 274) illustrating the newly found linking transition from band 1 to the GSB. 81
6.25 The double gated spectrum (x = 274 and y=1139). 81
6.26 The triple gated spectrum (x = 255, y = 238 and z= 292) illustrating the newly found linking transition from band 3 to the GSB. 81
6.27 The double gated spectrum (x = 274 and y = 204) illustrating the newly found linking transition from band 1 to the GSB. 82
6.28 The double gated spectrum (x = 232 and y = 204) illustrating the newly found linking transition from band 1 to the GSB. 82

7.1 Single-particle neutron calculation using deformation using deformation parameters relevant (γ=0,β_2=0.246) 85
7.2 Single-particle proton calculation using deformation using deformation parameters (γ=0,β_2=0.246) 85
7.3 Experimental alignment, i versus rotational frequencyω for the positive parity bands in ^{130}Ce. The Harris parameters of $\Im_0$= 17 MeV^{-1} $\hbar^2$ and $\Im_1$= 25.8 MeV^{-3} $\hbar^4$ have been used. 87
7.4 Experimental routhian, e' versus rotational frequency ω for the positive parity bands in ^{130}Ce. The Harris parameters of $\Im_0$= 17 MeV^{-1} $\hbar^2$ and $\Im_1$= 25.8 MeV^{-3} $\hbar^4$ have been used. 87
7.5 Experimental alignment, i versus rotational frequencyω for the bands 5 and 6 in ^{130}Ce. The Harris parameters of $\Im_0$= 17 MeV^{-1} $\hbar^2$ and $\Im_1$= 25.8 MeV^{-3} $\hbar^4$ have been used. 89
7.6 Experimental routhian, e' versus rotational frequency ω for the bands 5 and 6 in ^{130}Ce. See Fig7.5 for Harris parameters. 90
7.7 Experimental alignment, i versus rotational frequencyω for the bands 7 and 8 in ^{130}Ce. The Harris parameters of $\Im_0$= 17 Mev^{-1} $\hbar^2$ and $\Im_1$= 25.8 Mev^{-3} $\hbar^4$ have been used. 91
7.8 Experimental routhian, e' versus rotational frequency ω for the bands 7 and 8 in ^{130}Ce. See Fig7.7 for Harris parameters 91

7.9 Experimental alignment, i versus rotational frequencyω for the positive parity bands in ^{130}Ce. The Harris parameters of $\Im_0$= 17 Mev^{-1} $\hbar^2$ and $\Im_1$= 25.8 Mev^{-3} $\hbar^4$ have been used. 92
7.10 Experimental routhian, e' versus rotational frequency ω for the positive parity bands in ^{130}Ce. The Harris parameters of $\Im_0$= 17 MeV^{-1} $\hbar^2$ and $\Im_1$= 25.8 MeV^{-3} $\hbar^4$ have been used. 93
7.11 Experimental B(M1)/B(E2) ratios of reduced transition probabilities for the bands in ^{130}Ce. The lines show theoretical estimates obtained for the given configurations 5 and 6 in ^{130}Ce. 95
7.12 Experimental B(M1)/B(E2) ratios of reduced transition probabilities for the bands in ^{130}Ce. The lines show theoretical estimates obtained for the given configurations 7 and 8 in ^{130}Ce. 95
7.13 Experimental B(M1)/B(E2) ratios of reduced transition probabilities for the bands in ^{130}Ce. The lines show theoretical estimates obtained for the given configurations 1, 2, 3 and 4 in ^{130}Ce. 96

List of Tables

2.1 Occupation of harmonic oscillator shells 5

5.1 Typical measured DCO ratio of γ rays as illustrated in Figure 5.1. . 34

5.2 Measured properties of γ ray transitions feeding the 42^+ state in band 1. The intensities (I_γ) are measured relative to 555 keV ($42^+ \rightarrow 40^+$) γ ray 40

6.1 The yields of the nuclei are measured relative to 254 keV ($2^+ \rightarrow 0^+$) γ-ray in ^{130}Ce. 56

6.2 Measured properties of γ ray transitions ^{130}Ce. The intensities (I_γ) are measured relative to 254 keV ($2^+ \rightarrow 0^+$) γ ray. The γ-ray energy accuracy is of $\pm$0.3 keV in energy for strong transitions and $\pm$0.6 keV for weaker transitions. The intensities less than 1% of 254 keV($\equiv$100%) are neglected. The errors on the intensities are %5 of the obtained values for strong transitions and for the weaker transitions to be %10 of the obtained values. 65

7.1 Quasiparticle labels regarding to ^{130}Ce including the dominant Nilsson components and their parity and signature, (π,α). 86

7.2 Quasiparticle configuration regarding to ^{130}Ce including the experimental and theoretical crossing frequency in each. 86

7.3 Parameters were used in B(M1)/B(E2) estimation. 95

7.4 Energy intensities were used in B(M1)/B(E2) calculations. The energies are in KeV and in order to measure the intensity of the transitions gates were put above the level of interest. 98

Chapter 1

Introduction

Recent developments in heavy ion accelerators and gamma-ray detection systems have made the study of nuclear structure at high angular momentum feasible. Two separate experiments have been performed in order to study the discrete level schemes of two nuclei ^{156}Er and ^{130}Ce, in region of so called deformed nuclei. Through γ-ray spectroscopy excited states have been established for ^{130}Ce which fit into rotational band structures. The previously known band structures in ^{156}Er have been examined and number of new gamma-rays have been identified feeding the band terminating state in this nucleus. The experimental results have been interpreted and understood within the framework of the Cranked Shell Model. Following this brief introduction chapter 2, is devoted to an overview of nuclear models comprising the Spherical Shell Model, nuclear deformation and the Nilsson Model. After briefly mentioning nuclear models, the nuclear rotation and consequently the Cranked Shell Model have been briefly traced in Chapter 3. In Chapter 4 common experimental details to both experiments are discussed. Chapter 5 deals with the results extracted from the analysis of ^{156}Er and its relevant discussion. The second experiment, ^{130}Ce along with its analysis results have been presented in Chapter 6. Finally Chapter 7 is devoted to interpretation of results gained for ^{130}Ce which is performed within the Cranked Nilsson-Strutinsky model.

Chapter 2

Nuclear Models

2.1 Introduction

The past century has seen the rapid development in nuclear models and consequently enormous improvement in our knowledge about the structure of nuclei. In the history of the development of nuclear models, the Liquid Drop Model (LDM) has been thought of as a key factor in nuclear structure information. The LDM specifies an expression for the binding energy of nucleus and considers the nucleus as an incompressible macroscopic drop of liquid. In 1935 Weiszäcker [6] formulated the famous semi empirical mass formula to calculate the total binding energy of the nucleus. Despite this success, experimental results show a number of discrepancies. The model describes a smooth change in nuclear properties as their atomic number changes. This is in contrary with the experimental results which have identified a number of discontinuities in behaviour at certain values of neutrons and proton nucleus. The LDM failed to explain and reproduce these discrepancies and therefore the Shell model was established.

2.2 The Spherical Shell Model

After the remarkable success of the atomic shell model, the nuclear shell model is used to explain the discrepancies in nuclear binding energies. Analogous to the atomic case where we fill the shells with electrons in order of increasing energy, the nucleons are filled into the shells with specific quantum numbers and consistent with the Pauli exclusion principle.(i.e. no identical fermions can occupy the same state). According to the nuclear shell model nucleons move independently and smoothly within a potential created from all other nucleons in the nucleus. In the absence of empty levels within the range of an interaction, the interaction can not occur and the nucleons would orbit.

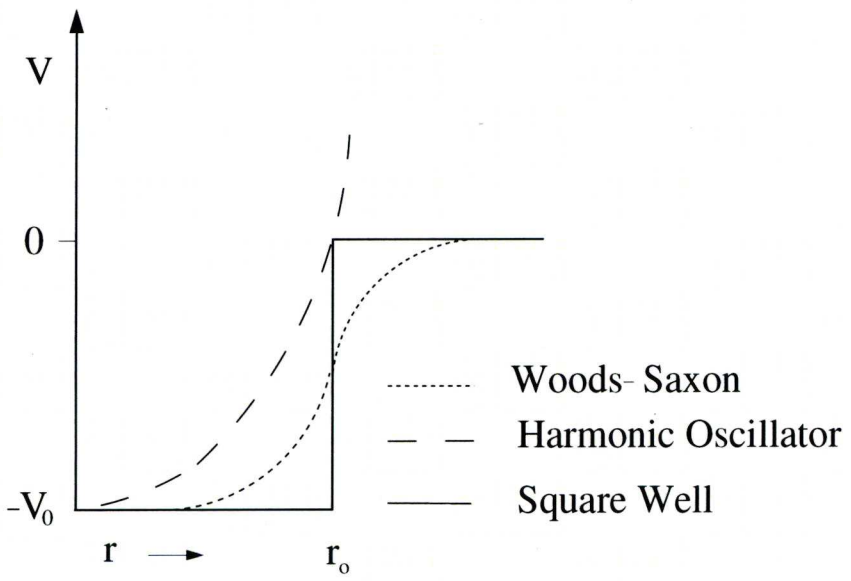

FIGURE 2.1: An illustration of three potential wells used to model the nuclear potential. V_0 is the well depth, r the distance from the origin and r_o the nuclear radius

In order to explain the observed energy levels and occurrence of so called magic numbers which correspond to the filling of major shells, many studies have been carried out to construct the potential wells (see figure 2.1). The form of the potential for a spherical nucleus must be spherically symmetric and dependent on the distance from the centre of the nucleus. The spherical oscillator potential, despite

some successes could not be a good approximation to the nuclear potential, as it tends to infinity outside the nucleus. Having this potential in place, an intermediate form of nuclear potential, the so called Wood-Saxon potential was chosen. It is the most realistic form of the potential as it approximates the nuclear matter distribution, as it represents the constant charge and mass distribution distribution within the nuclear radius and also a smooth distribution to zero outside the nucleus[7]:

$$V_{WS}(r) = \frac{-V_o}{1 + e^{\frac{r-R}{\alpha}}} \tag{2.1}$$

where V_o is potential depth, R is the mean nuclear radius and α is the surface thickness of nucleus. However the Wood-Saxon model is more difficult to solve than the harmonic oscillator. Hence, in nuclear physics the harmonic oscillator often is more used as it is more easily solvable. The harmonic oscillator potential can be written as [8]:

$$V_{SHO}(r) = -V_o + \frac{1}{2}M\omega_0^2 r^2 \tag{2.2}$$

where the M and ω_o are respectively, the mass of a nucleon and the frequency of simple harmonic motion of the particle. The resulting equally spaced energy levels would be as:

$$E_N = (N + \frac{3}{2})\hbar\omega - V_o \tag{2.3}$$

where each N shell has a degenerate group of different l shells, given by l<N. Even N corresponds to an even set of l levels and odd N to an odd set of l levels. The maximum number of nucleons which can be placed in each N shell will be (N + 1)(N + 2). Each oscillator shell contain only states with same parity, where the parity of each levels is given by :

$$\pi = (-1)^l = (-1)^N \tag{2.4}$$

N	Allowed l	Level Label	$E_N(\hbar\omega)$	Occupation	Total
0	0	1s	3/2	2	2
1	1	1p	5/2	6	8
2	2,0	1d,2s	7/2	12	20
3	3,1	1f,2p	9/2	20	40
4	4,2,0	1g,2d,3s	11/2	30	70
5	5,3,1	1h,2f,3p	13/2	42	112

TABLE 2.1: Occupation of harmonic oscillator shells .

The harmonic oscillator potential alone is unable to predict all the magic particle numbers. Two additions have been made to the model in order to reproduce the experimental magic numbers. The spin-orbit interaction [9] has been added which splits the levels into two components J= $l\pm1/2$, leading to J=l+1/2 lower in energy than J =l-1/2. For large J values, the interaction is large and therefore these energy levels will intrude into the major shell below, which is the (N-1) shell and with opposite parity. A maximum of 2J+1 identical particles can be held in each J state. Another major refinement to the model is the addition of attractive (l^2) term. It tends to flatten the harmonic oscillator potential by adding a term which is proportional to orbital angular momentum l^2, resulting in the correct experimental magic numbers.

2.3 Nuclear Deformation

The main limitation of the spherical shell model, despite all its success in theoretical predictions for spherical ground state nuclei (or near a closed shell), however, is dealing with deformed nuclei. Recent developments in nuclear detection systems and heavy ion acceleration facilities have led to dramatic growth in nuclear data and experimental evidence of rotational bands and large quadrupole moments. The existence of static nuclear deformation between closed shells, such as nuclei with mass number A $\simeq$ 25 (i.e.Al, Mg) and 120$\leq$A$\leq$170 (rare earth nuclei such as Er and Ce which are the main focus of this thesis), leads to the choice of a

deformed potential rather than a spherical potential. The shape of a deformed nucleus can be reproduced through expansion of the nuclear radius R(θ, ϕ) in terms of $Y_{\lambda,\mu}(\theta, \phi)$.

$$R(\theta, \phi) = R_o(1 + \sum_{\lambda=0}^{\infty} \sum_{\mu=-\lambda}^{\lambda} \alpha_{\lambda\mu} Y_{\lambda\mu}(\theta, \phi)) \tag{2.5}$$

where R_o , that is the radius of a sphere of the same volume and α the shape parameters. The $\alpha_{\alpha\mu}$ is the multipole expansion of multipolarity λ and for quadrupole deformation (λ=2) can be written as:

$$\alpha_{20} = \beta_2 cos\gamma \quad \alpha_{21} = \alpha_{2-1} = 0 \quad \alpha_{22} = \alpha_{2-2} = \frac{1}{\sqrt{2}} \beta_2 sin\gamma \tag{2.6}$$

where parameters β_2 and γ, respectively, measure the elongation of the axially symmetric shape and triaxiality. Figure 2.2 depicts the various shapes in terms of various (β_2 and γ) coordinates, for quadrupole deformation (λ=2).

The representation is given by the Lund convention where γ=0^o, -120^o corresponds to prolate shape (Rugby football shape), γ= 60^o , -60^o are oblate shapes (disc shape) and intermediate values of γ (it is not a multiple of 60) correspond to a triaxial shape.

2.4 The Anistropic Harmonic Oscillator Potential

The deformed harmonic oscillator potential for an axially deformed nucleus with deformation along the z axis (i.e. x = y $\neq$ z) can be written as[10]:

$$V_{AHO} = \frac{1}{2} M[\omega_{\perp}^2 (x^2 + y^2) + \omega_z^2 z^2] \tag{2.7}$$

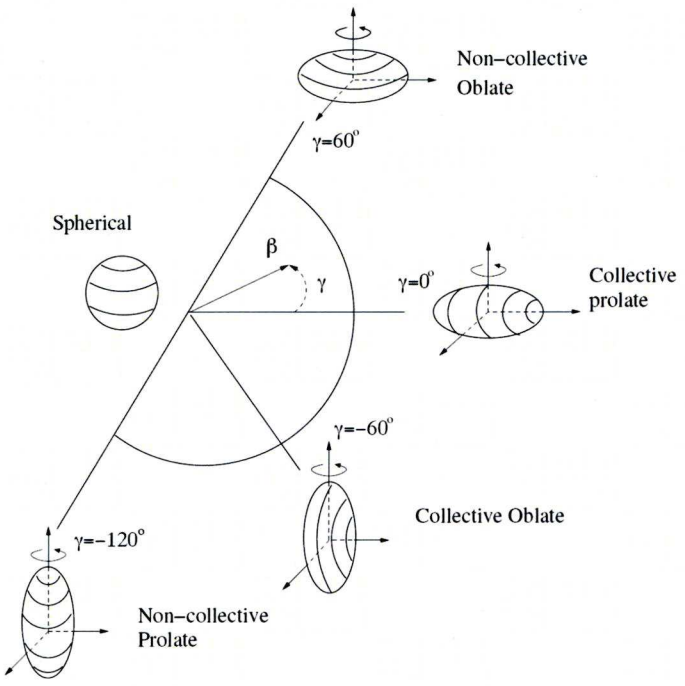

FIGURE 2.2: The Lund convention for nuclear shapes. The parameters β_2 and γ are, respectively, measures the elongation of the axially symmetric shape and triaxiality, taken from [1].

where $\omega_\perp$ and ω_z are respectively, one dimensional oscillator frequencies perpendicular and parallel to the symmetry axis. These can be described in terms of the deformation parameter δ, as the following:

$$\omega_z \approx \omega_0[1 - \tfrac{2}{3}\delta], \quad \omega_\perp \approx \omega_0[1 + \tfrac{1}{3}\delta] \tag{2.8}$$

where ω_0 is the spherical nucleon's oscillator frequency and has an isospin dependance :

$$\hbar\omega_0 \approx 41A^{-\frac{1}{3}}(MeV) \tag{2.9}$$

such that negative and positive signs are respectively for protons and neutrons. The introduction of stretched coordinates by Nilsson [12] led to the definition of a new set of deformation parameters ϵ_2[11][13] which allow the oscillator potential to be described by:

$$V_{AHO} = \frac{1}{2}\hbar\omega(\epsilon_2)\rho^2[1 - \frac{2}{3}\epsilon_2 P_2(cos\theta_t)] \tag{2.10}$$

where the relationship between two deformation parameters is given by [8](λ =2, for quadrupole deformation)

$$\epsilon_2 \approx 0.95\beta_2 \tag{2.11}$$

and in equation 2.10 ρ represents the sum of the stretched coordinates and the angle in the stretched coordinates is represented by θ_t.

2.5 The Nilsson Model

Similarly to the shell model, for the anharmonic oscillaor potential the two terms, l^2 and l.s were added by Nilsson in order to produce the correct shell structure [12](i.e. the Nilsson model or the deformed shell model). Therefore the Nilsson potential or Modified Harmonic Oscillator (MHO) can be written as:

$$V_{MHO} = V_{AHO} - \kappa\hbar\omega[2l.s + \mu(l^2 - \langle l^2\rangle_N)] \tag{2.12}$$

where κ and μ are adjustable coupling parameters which can be extracted from fits to experimental energy levels. These parameters are different for each major oscillator shell. The following asymptotic quantum numbers are used to label the level energies produced by the model:

$$[Nn_z\Lambda]\Omega^\pi \tag{2.13}$$

where N,n_z and Λ are respectivle, the major oscillator shell, number of the nodes in wavefuntion along the z direction and orbital angular momentum's projection on the symmetry axis. The projection of the total angular momentum on the symmetry axis Ω can be written as: Ω=$\Lambda \pm \Sigma = \Lambda \pm \frac{1}{2}$ where Σ is the nuclear

spin projection on the symmetry axis. Nilsson diagrams depicted in Figure 2.3 and 2.4 show the single particle energies as a function of the quadrupole deformation parameter, ϵ_2 for neutrons and protons.

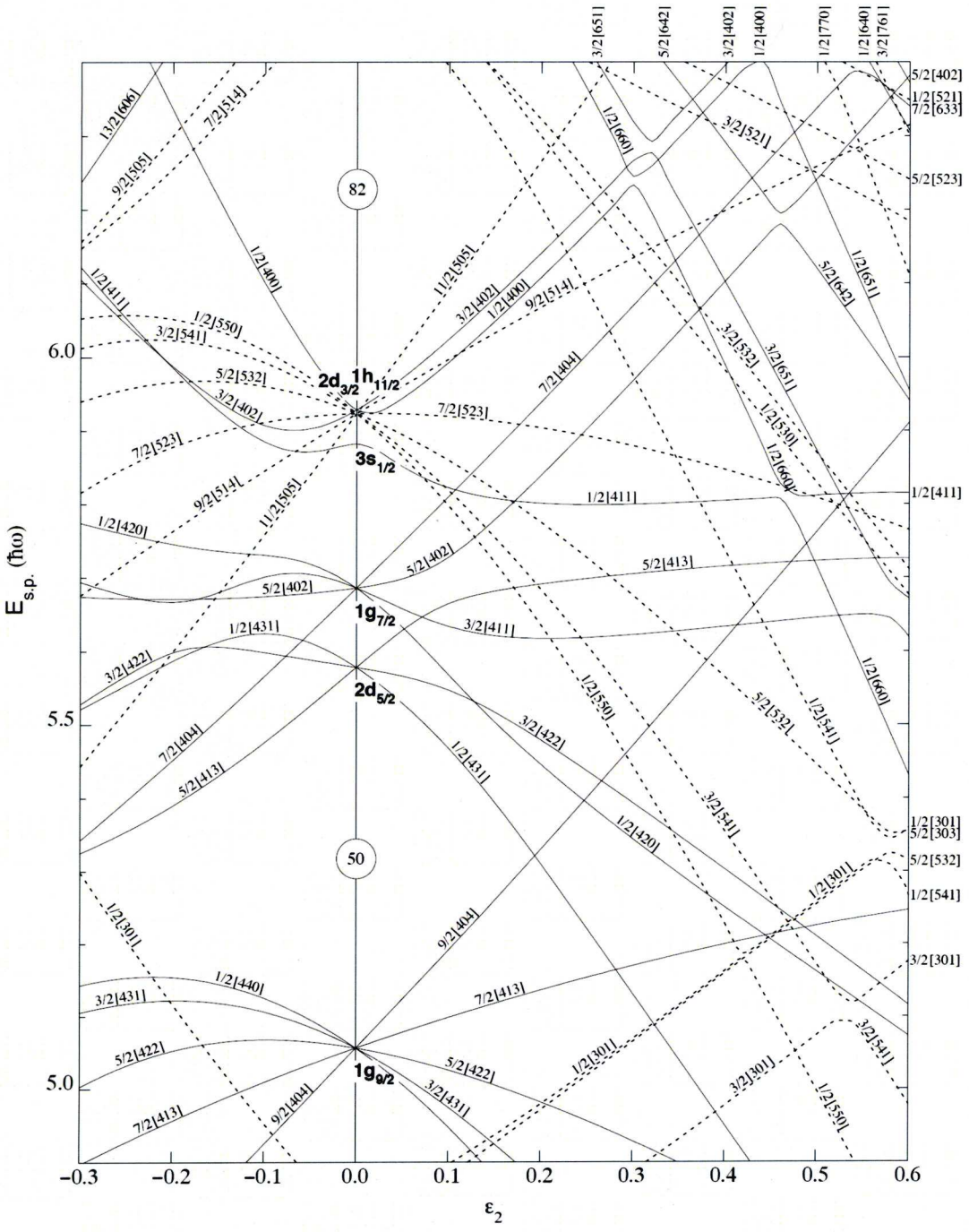

FIGURE 2.3: Nilsson diagram of single-neutron energies ($50 \leq N \leq 82$). Full and dashed lines corresponds to positive and negative parity orbitals respectively[2].

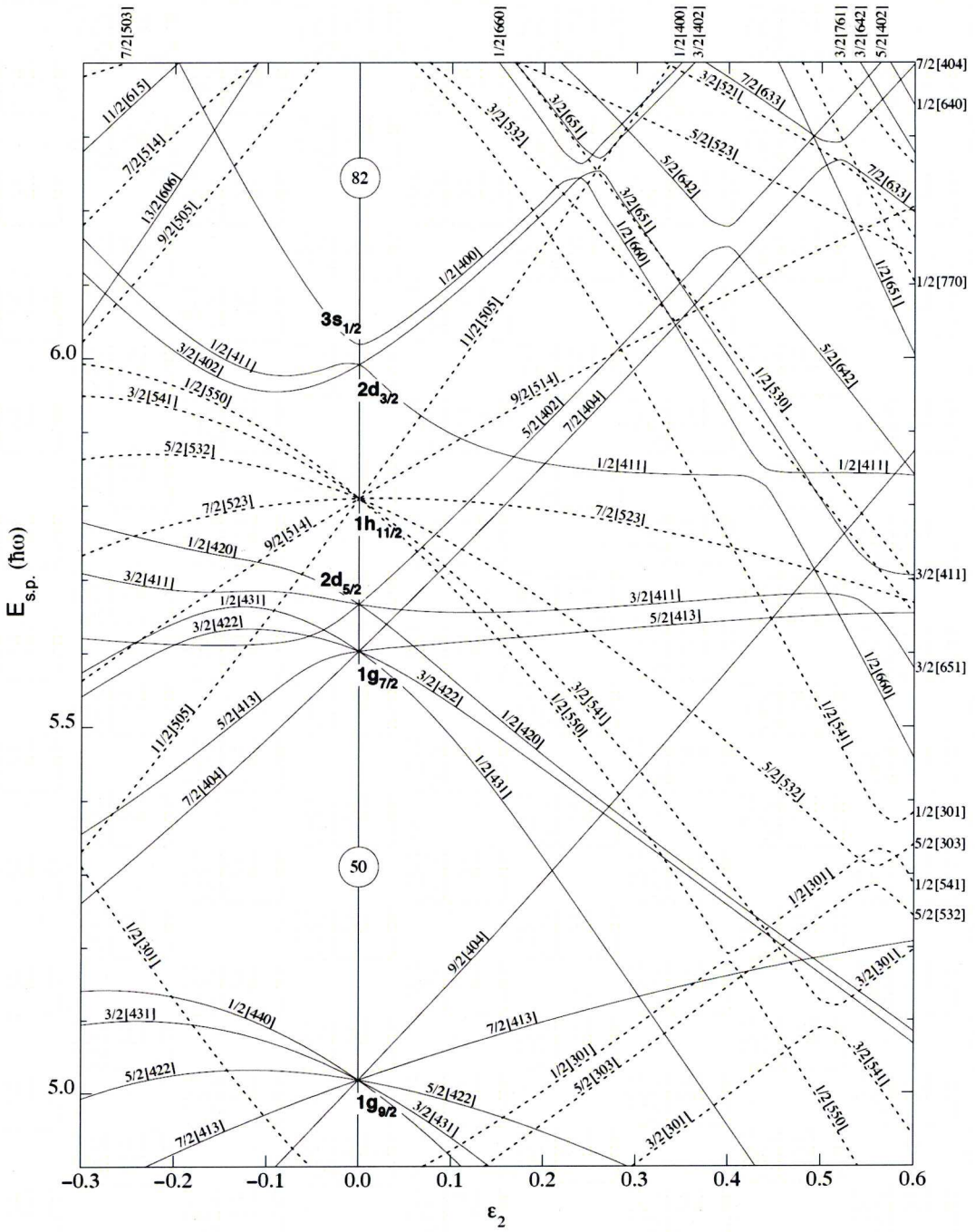

FIGURE 2.4: Nilsson diagram of single-proton energies ($50 \leq Z \leq 82$) . Full and dashed lines corresponds to positive and negative parity orbitals respectively[2].

The orbital anglar momentum l and total angular momentum j are no longer good quantum numbers and the parity and K (the angular momentum projection on the symmetry axis) are the only conserved quantum numbers. In the Nilsson model low Ω-value orbitals have a large spatial overlap with a prolate deformed core, and thus, these equatorial orbits are lowered in energy with increasing prolate deformation. In the case of oblate deformed core, the high Ω-value orbitals have a large spatial overlap with the core and orbitals are lowered in energy with increasing oblate deformation. According to the Pauli exclusion principle, quantum mechanically it is forbidden for any two levels with same quantum numbers to cross and in the Nilsson diagram such levels do not cross but exchange their characteristics and the wavefunction properties. The correct magic numbers appear at zero deformation, regions of low level density. For different neutron and proton numbers, however, these low level density regions disappear and new regions (magic numbers) appear as the deformation increases.

2.6 The Strutinsky shell Correction Procedure

The shell model has been successful in the prediction of particular nuclear properties when nucleons near the Fermi surface are involved. However it fails to reproduce the bulk properties such as nuclear binding energy where all the nucleons contribute. Consequently, the Strutinsky shell correction procedure[14][15]was introduced to combine the successful features of each model. The idea was to separate the total energy of nucleus into two parts; an oscillatory part ΔE_{shell} from the microscopic shell model and the liquid-drop part E_{LDM}:

$$E = E_{LDM} + \Delta E_{shell} \tag{2.14}$$

The liquid-drop part is calculated from Liquid Drop Model(macroscopic) and the oscillatory part(microscopic) is calculated from the shell model. The oscillatory part arises from the fact that the binding energy of the nucleus is dependent on

the level densities near the Fermi surface.Therfore, the nucleus for which the Fermi surface appears in a region of low density will be more strongly bound.

2.7 Pairing

The pairing interaction is the short-range, attractive component of the nucleon-nucleon force which tends to couple the particle's angular momentum to zero. It was introduced to explain experimental features which could not be explained within the framework of the Shell model. Some of the experimental evidence for the pairing interaction are the following:

- The even-even nuclei invariably have ground state spin and parity of $I^{\pi}=0^{+}$. (as pairing tends to orient the pair of nucleons such that their angular momentum cancel out)
- Appearance of an energy gap ($\approx$ 1.5 MeV) in non-collective excitation energies of even-even nuclei which is absent in neighbouring nuclei.
- The last nucleons in even-even nuclei are more strongly bound compared to neighbouring odd mass nuclei and therefore the total binding energies of odd A nuclei are less than even A nuclei.
- The moments of inertia for deformed nuclei are approximately one third of expected value for a rigid-body at low spins.

The Pauli exclusion principle forbids the scattering of nucleons below Fermi surface where there are no free orbits available. However, near the Fermi surface due to existence of unoccupied orbitals the scattering can take place resulting in a smeared Fermi surface.

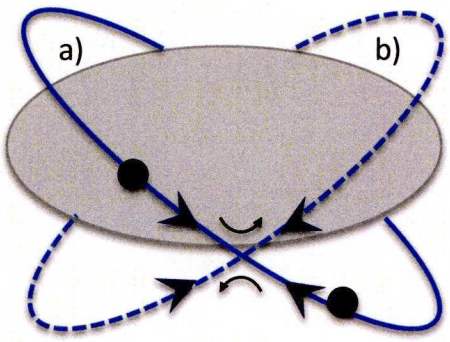

FIGURE 2.5: Two identical nucleons in time-reversed orbits,(a), scattering into new time- reversed orbits,(b).[3].

2.8 Quasi particles

A quasi particle is considered as a mixture of particle (occupied) and holes (unoccupied) states. Consequently the particle-hole excitation can be introduced by simultaneous creation and annihilation of quasiparticles. The quasi particle energy of state i can be given by:

$$E_i = \sqrt{(\epsilon_i - \lambda)^2 + \Delta^2} \tag{2.15}$$

where E_i is single particle energy, λ, Fermi energy, ϵ_i is single particle separation energy and Δ corresponds to the pair gap. The term (ϵ_i - λ) corresponds to single particle excitation energy and in the presence of the pairing correction it will be replaced by E_i.

Chapter 3

Nuclear Rotation

3.1 Introduction

The generation of angular momentum in the nucleus can be through either collective rotation or single particle excitations (Figure 3.1).

3.2 Non-Collective single Particle Excitation

Near closed shells, ground state of nuclei are found to be spherical or near spherical (Figure 3.2). In these types of nuclei as the system possesses spherical symmetry, quantum mechanics states that the collective rotation is not allowed. Such systems can only generate angular momentum through the rearrangement of the valence particles. In this way, the rest of the nucleus (the core) makes no contribution and the sum of the spins of valence nucleons that are not coupled to spin zero will be the total angular momentum.

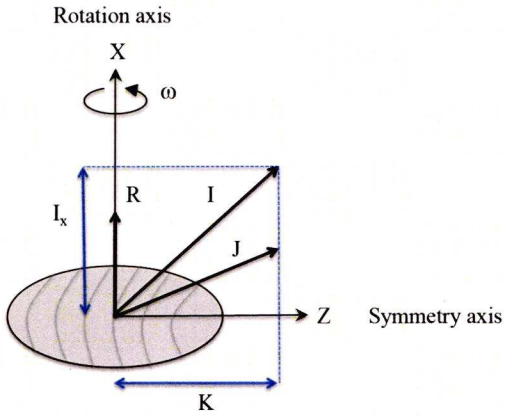

FIGURE 3.1: A deformed nucleus rotating about an axis perpendicular to the symmetry axis and its angular momentum projections

3.3 Collective Rotation

The angular momentum in non-spherical axially deformed nuclei can be generated through collective rotation. The rotation is perpendicular to the symmetry axis, with all of the nucleons contributing to the angular momentum coherently.

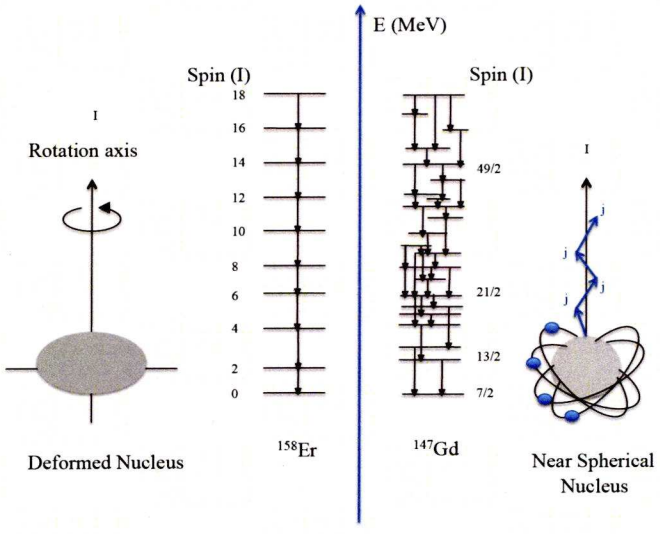

FIGURE 3.2: Single particle and collective modes of excitation [3]

The total angular momentum I, is composed of two parts, the angular momentum generated from the core R and J, that is the sum of the single particle contributions.

$$\vec{I} = \vec{R} + \vec{J} \tag{3.1}$$

where

$$\vec{J} = \sum_{i=1}^{valence} \vec{j_i} \tag{3.2}$$

The projection of the total angular momentum on the rotational axis (aligned angular momentum) is I_x :

$$I_x = \sqrt{I(I+1) - K^2} \tag{3.3}$$

where K is the projection of the total angular momentum onto the symmetry axis z. In the ground state band of an even-even deformed nucleus, the angular momentum will have no contribution from the valence nucleons as they are paired off at low spin (i.e. I = R).

The energy associated with the rotation in deformed nuclei arises from a coherent contribution from many nucleons:

$$E(I) = \frac{\hbar^2}{2J} I(I+1) \tag{3.4}$$

where J is static moment of inertia and gives rise to a series of levels with energies proportional to I(I+1). The expression 3.4 defines the energies of a nucleus rotating collectively with no single-particle excitation involved (K=0). The rotating nucleus would exhibit set of excited states, transitions from which cascade down towards the ground state through a sequence of enhanced stretched electric quadrupole transitions. If however a single particle excitation were involved in the establishment of a rotational band the equation 3.4 will change to:

$$E(I) = \frac{\hbar^2}{2J} [I(I+1) - K^2] \tag{3.5}$$

The energy of a transition in the rotational band, between two successive levels (I →I-2) is given by:

$$E_\gamma = E(I) - E(I-2) = \frac{\hbar^2}{2J}(4I-2) \tag{3.6}$$

which possesses the linear relationship between E_γ and I.

3.4 Moment of Inertia

The rotational frequency ω can be defined [3] as:

$$\hbar\omega = \frac{dE}{dI_x} \simeq \frac{E_\gamma}{2} \tag{3.7}$$

Two possible definitions for the moment of inertia for a rotating nucleus have been introduced [16] in order to report two different classes of nuclear dynamical properties. First the kinematic moment of inertia:

$$J^{(1)} = \frac{\hbar^2}{2}\left[\frac{dE}{dI_x}\right]^{-1} = \hbar\frac{I}{\omega} \tag{3.8}$$

and secondly the dynamic moment of inertia which can be defined as:

$$J^{(2)} = \hbar^2\left[\frac{d^2E(I)}{dI_x^2}\right]^{-1} = \hbar\frac{dI}{d\omega} \tag{3.9}$$

These two proposed moments of inertia experimentally can be defined by:

$$J^{(1)} = \hbar^2\frac{(2I-1)}{E_\gamma} \tag{3.10}$$

$$J^{(2)} = \frac{4\hbar^2}{\Delta E_\gamma} \tag{3.11}$$

The dynamic moment of inertia $J^{(2)}$ is independent of the spins of the levels in the rotational band and depends only on the energy differences between gamma transitions (ΔE_γ) which makes it sensitive to structural changes taking place within the band.

3.5 The Coriolis Anti-Pairing (CAP) Effect

The internal force in any rotating system can be separated into coriolis and centrifugal forces. The coriolis force tends to quench the pairing correlation through decoupling pairs from J = zero and classically can be written as[16]:

$$\vec{F}_{cor} = -2m[\vec{\omega} \times \vec{v}] \tag{3.12}$$

where m is the mass, v is the velocity of the particle and ω is the rotational frequency. Superfluidity manifests itself in nuclei at low spin through Cooper pairs where two nucleons are combined together in time-reversed orbits. As the rotational frequency ω increases the coriolis interaction will be increased, resulting in a gradual decrease in Δ(pairing gap parameter) and an increase in the nuclear moments of inertia. This effect acts differently on each of time-reversed orbitals is called Coriolis Anti-pairing effect (CAP).

At low rotational frequency the coriolis force is not strong and with a sufficiently deformed nuclear field the motion of nucleon will be coupled to the deformation of the core. Therefore the angular momentum of the valence particles will be aligned with axis of symmetry (known as strong-deformation aligned scheme), see Figure.3.3.

The coriolis effects at spins of about 12-14 $\hbar$ in Er nuclei (and slightly lower range for lighter mass regions) are strong enough to overcome the paring force. It will eventually lead to break a specific pair of valence nucleons and the alignment of

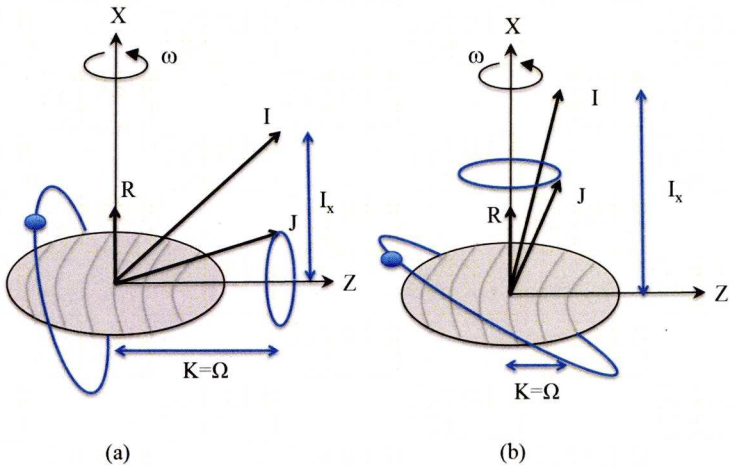

FIGURE 3.3: Particle coupling scheme; Deformations aligned (a) and Rotational alignment(b)

their angular momenta along the rotation axis.

$$E_{cor} = \frac{\hbar^2}{J} j.I \tag{3.13}$$

where I, j and J are total angular momentum, angular momentum of valence particle and moment of inertia respectively. From equation 3.13 high J low Ω orbitals are effected and aligned first. The paring strength can face sudden drops following the breaking of a specific pair of particles.

3.5.1 The Cranking model

In order to explain the behaviour of nuclei at high angular momentum the Cranked Shell model (CSM) is used. The idea of rotation (cranking) about an axis x, perpendicular to the symmetry axis was first brought up by D.R. Inglis in 1954-1956 [17][18], and developed by Bengtsson and Frauendorf in 1979 [19]. The CSM treats the nucleons independently as it takes into account th effect of rotation on the single particle energies of the Nilsson model. The total cranking hamiltonian

,H^{ω} which is sum of the single-particle hamiltonians is given by:

$$H^{\omega} = H_{int} - \hbar\omega I_x \tag{3.14}$$

where H_{int} and ωI_x are intrinsic single particle hamiltonian and analogous to the coriolis and centrifugal forces respectively.

3.6 Nuclear Symmetries

Parity and Signature are the only two remaining symmetries after the introduction of rotation to an axially deformed nuclei. The parity (π) corresponds to the behaviour of the spatial wavefunction after a reflection of all coordinates through the origin. The results of the translation of the wavefunction, imposed by the parity operator, are:

$$\psi(-\vec{r}) = +\psi(\vec{r}) \tag{3.15}$$

corresponding to even parity and

$$\psi(-\vec{r}) = -\psi(\vec{r}) \tag{3.16}$$

for odd parity.

Under reflection symmetry the stationary state of the wavefunction must be either even or odd and the parity of the nucleon state is given by the product of the parities of the unoccupied single-particle orbitals:

$$\pi_{state} = -\prod_{occ} \pi_i \tag{3.17}$$

Signature (α) originates from the eigenvalue of rotation operator $\hat{R}$, the rotation through 180^o about the rotational axis x,

$$\hat{R}_x = exp^{-i\pi I_x} \tag{3.18}$$

where r is eigenvalues of the rotation operator $\hat{R}$ and may be defined as:

$$r \equiv exp^{-i\pi\alpha} \tag{3.19}$$

where α is the signature exponent quantum number, and for integer spin I :

$$r = (-1)^I \tag{3.20}$$

where I is the spin and results in following set of selection rules for rotational bands:

$$I = 0, 2, 4, ... \quad K = 0 \quad r = +1 \tag{3.21}$$

$$I = 1, 3, 5, ... \quad K = 0 \quad r = -1 \tag{3.22}$$

Chapter 4

Experimental Details

4.1 Introduction

The following chapter underlines the techniques have been employed in this work. In order to study the structure of the nucleus a heavy ion fusion reaction has been used. In these reactions, high spin (before fission) states were populated.

4.1.1 Heavy Ion Fusion Evaporation Reaction

The heavy-ion fusion evaporation reaction provides the most efficient way to transfer to the nucleus highest possible angular momentum and cross section. Through this reaction mechanism, the incident projectile nucleus fuses with a target nucleus which leads to a compound nucleus formation. In order to fuse two nuclei together, the projectile nucleus should have sufficient energy in order to overcome the Coulomb barrier which is defined as [20].:

$$E_{CB} = \frac{Z_p Z_t}{R_{CB}} MeV \tag{4.1}$$

R_{CB} denotes the Coulomb radius which may be approximated [20] as:

$$R_{CB} = [1.36(A_p^{1/3} + A_t^{1/3}) + 0.5]fm \tag{4.2}$$

where Z_p, A_p and Z_t,A_t are atomic and mass number of the projectile and the target respectively. The reaction mechanism brings the maximum angular momentum to the compound nucleus when the impact parameter b is equivalent to the separation distance R (see Fig 4.1).

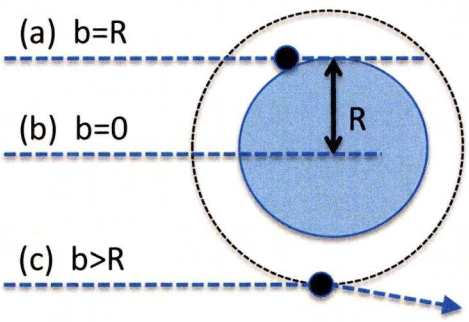

FIGURE 4.1: Schematic illustration of different impact parameters b, (assuming projectile nucleus has negligible size).

According to N.Bohr in 1936 [21], the reaction occurs at two distinct stages of formation and decay. The lifetime of composite system (for nuclei with $Z \geqslant 30$) is large compared to the time it takes for projectile particle to travel distance equal to diameter of the target nucleus. This delay will allow the composite system to reach thermodynamic equilibrium in which the kinetic energy of compound system is distributed equally within its constituents and said to lose its "memory" of how it was formed. Once the fusion of the projectile and target occurs, the compound nucleus will be formed (e.g ^{162}Er and ^{134}Ce in our work) at very high excitation energy with a large amount angular momentum. After a relatively short period of time ($\approx 10^{-19}$ s) the compound nucleus decays. The decay involves evaporating particles such as protons , neutrons and α particles which tend to carry away large amount of energy but little angular momentum. Figure 4.2 illustrates the modes of de-excitation of a compound nucleus following a heavy-ion fusion evaporation reaction.

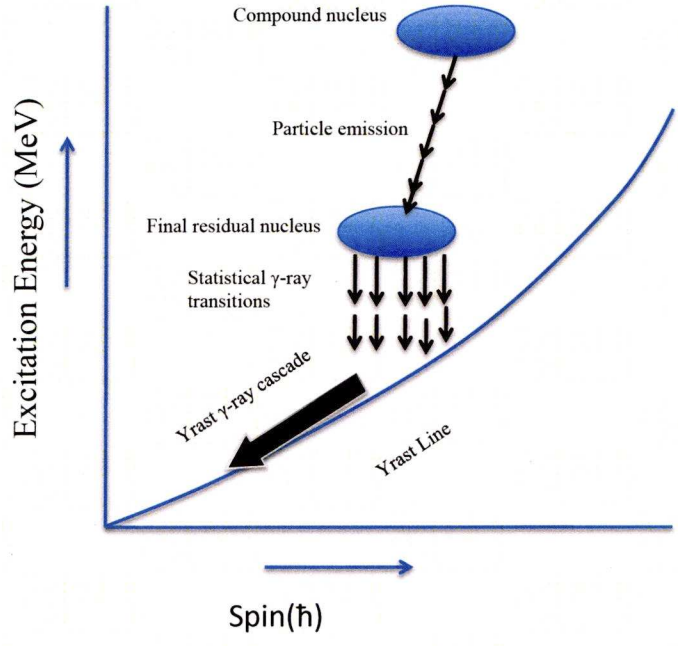

FIGURE 4.2: The modes of de-excitation of a compound nucleus following a heavy-ion fusion evaporation reaction [1].

For every particle (n,p,α) which is evaporated the amount of energy at least equal to its separation energy is removed from the system. Particle evaporation continues until the excitation energy remaining in the system falls below the one nucleon separation energy above the yrast line ($\approx$ 8 MeV). At this point as the particle emission is energetically unfavourable the nucleus decays via γ -ray emission. A continuum of statistical γ -rays may proceed due to high density of states at this point. When the excitation energy of system is within 2-3 MeV of yrast line , the level density is low enough for discrete decays (e.g. stretched quadrupole (E2) transitions) to be observed. The spectroscopic study of these γ-rays give information about the structure of the nucleus[22]. These γ -rays can carry away a large amount of angular momentum, for instance 70-80 $\hbar$ angular momentum may be dissipated through emission of a cascade of 30-40 γ-rays. Using the techniques such as coincidence spectroscopy (γ-γ matrices, γ -γ-γ cubes or even γ-γ-γ-γ hypercubes) the excitation pathway and level schemes regarding to these γ-rays can be constructed and studied.

4.2 Gamma Decay

The emission of electromagnetic radiation in the form of photons or γ-rays can tell us about the properties of initial and final energy states (E_i and E_f) -as the emitted radiation would be the energy difference between two states. Conservation laws and electromagnetic selection rules are mostly used in order to measure and study the electromagnetic radiation properties. The properties which can be measured are: excitation energy, angular momentum (or spin) and parity. In order to measure the angular momentum carried by the electromagnetic radiation transition from an initial nuclear state with spin and parity I_i^π to a state with final spin and parity ,I_f^π, the following electromagnetic selection rule can be imposed:

$$|I_i - I_f| \geq L \geq I_i + I_f \tag{4.3}$$

where L is the possible multipole order of the emitted photon. As the internal spin of the photon is $1\hbar$, the electromagnetic radiation between two 0^+ states is forbidden and the decay can only proceed via internal conversion. The parity conservation laws also imply that the electric or magnetic nature of electromagnetic radiation should follow the expression:

$$\pi_{EL} = (-1)^L \tag{4.4}$$

$$\pi_{EM} = (-1)^{L+1} \tag{4.5}$$

In order to have initial and final states with the same parity, the electromagnetic radiation between them must have even parity. This means between states of same parity, transitions of types M1,E2,M3, etc. and between states of opposite parity E1, M2, E3,etc. can be proceed.

4.3 DCO Analysis

Following the fusion evaporation reaction the angular momentum of the compound nucleus is oriented perpendicular to the beam axis. The multipolarity of the emitted transitions from the compound nucleus in such a state affects the angular distribution of relative intensity of transitions with respect to the beam axis. The Directional Correlation of Oriented states method (DCO) [23] can be performed in order to gain information on the multipolarity of the transitions. As the detectors are distributed approximately isotropically within the array(e.g Gammasphere[24] and Eurogam [25]) the transitions can be gated(selected) in any detector and the angular correlation effect can be studied. The angular intensity ratio is defined as :

$$R = \frac{I(157°/22°)}{I(90°)}, \tag{4.6}$$

where I is the intensity of γ-ray . The reason behind the choice of these detector angles(extreme angles) is to obtain the largest difference in the DCO ratios, to distinguish the dipoles and quadrupoles. The dipole or quadrupole character of transition can be determined through this method. A typical value of this ratio (R) for pure dipole transition is ≈ 0.5 while for a stretched quadrupole transition it is ≈ 1.

4.4 Gamma Interaction With Matter

Photoelectric absorption, Compton scattering and pair production are the three major interaction mechanisms of γ-rays with matter i.e. our detection system. In the lowest energy regime ($E_\gamma \leq 200$ keV), the photoelectric absorption is the most probable interaction. In this interaction the incident photon interacts with an atomic electron and is absorbed. Compton scattering is the most probable interaction for 200 keV $\leqslant E_\gamma \leqslant$ 10 MeV , in which , the incident photon partly

transfer its energy to an atomic electron and the electron recoils. The Compton scattering formula can be written as:

$$\acute{E_\gamma} = \frac{E_\gamma}{1+\frac{E_\gamma}{m_o c^2}(1-cos\theta)} \tag{4.7}$$

where E_γ and $\acute{E_\gamma}$ are the energy of the incident photon and scattered photon respectively, m_o is the mass of electron , c is the speed of light and θ is the angle of the scatter. The third interaction, pair production, involves the total disappearance of a photon and its replacement by a negative and positive(positron) electron. For this purpose the energy of the incident photon should be at least equivalent to the rest mass of created positron and electron (511 keV each). The interaction probability increases for $E_\gamma \geqslant 1022$ keV and begins to be most probable at around $E_\gamma \approx 10$ MeV, depending on the atomic number of absorber material.

4.5 High-Purity Germanium (HPGe) Detectors

Germanium semiconductor detectors are popular in high spin γ-ray spectroscopy. One of the main reasons for this popularity lies in their higher intrinsic energy resolution. The HPGe detectors are cooled with liquid nitrogen, as at room temperature the small band gap of Germanium results in the appearance of thermal noise. The HPGe detectors have $\approx$2 keV energy resolution for a 1332 MeV γ-ray emitted from a ^{60}Co radioactive source.

4.5.1 Compton Suppression

A major limitation of the HPGe is Compton scattering of the incident radiation within the detector volume, leading to a partial deposition of its energy. Consequently, a spectrum consisting of a sharp photopeak and a continuum background below it, will manifest. In order to overcome this problem, a Compton suppression shield made of a high Z material which surrounds the germanium detector can be

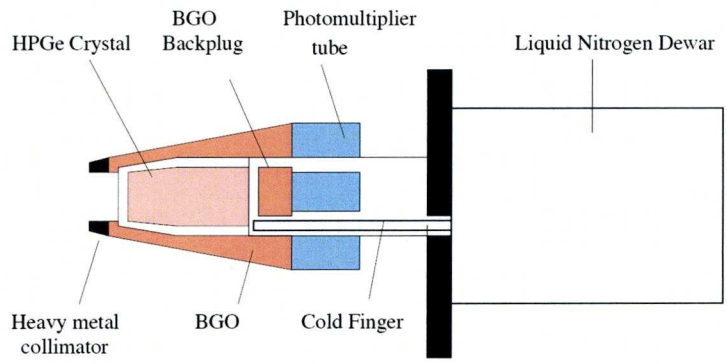

FIGURE 4.3: Schematic diagram of an escape-suppressed HPGe detector as used in the Gammasphere arrays. [1].

used. In this way, photons which scatter from germanium crystals can be detected and the event can be vetoed, thus lowering the background in the spectrum. In modern detector arrays such as Gammasphere [24] and Eurogam [8] the Compton suppression shields (CSS) are Bismuth Germanate (BGO) scintillator detectors.

4.5.2 Bismuth Germanate (BGO) Detectors

BGO detectors are an example of a scintillation detection in which, the energy of incident γ-ray is converted into visible light. The visible light then is converted into an electric signal by a photomultiplier tube. The advantage of the BGO is high gamma-ray detection efficiency due to the high atomic number and its high density. However, a disadvantage is poor resolution due to the lower light output of the detectors compared to other scintillator materials. For more information on the scintillator detectors the reader is referred to [26].

The effectiveness of CSS is often defined by the peak-to-total (PT) ratio which is defined as:

$$PT = \frac{(Number-of-counts-in-photopeak)}{(Total-number-of-counts)} \tag{4.8}$$

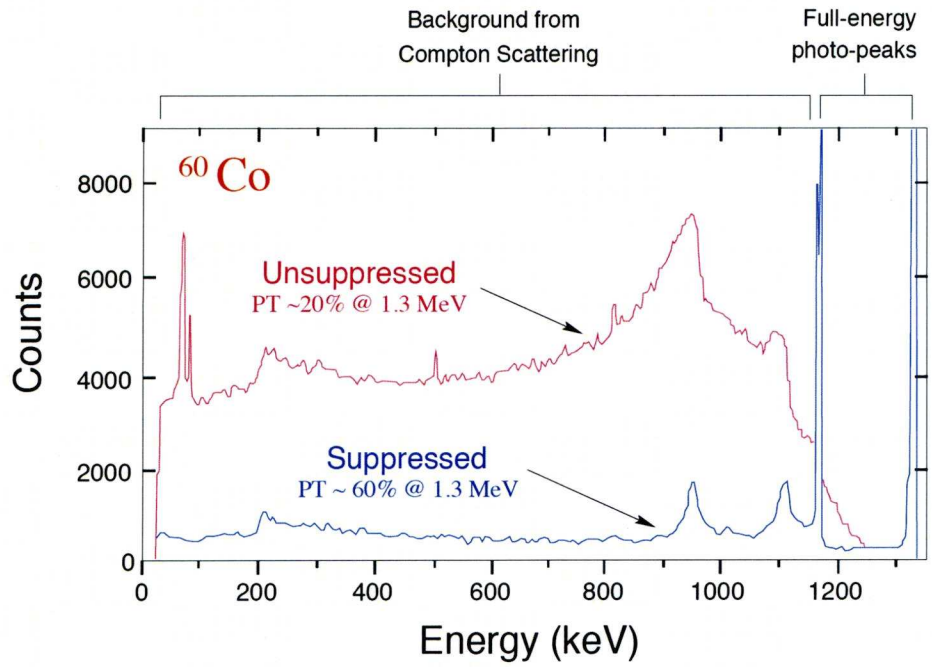

FIGURE 4.4: Spectra obtained using the escaped-suppressed Ge detector of the Gammasphere array for 1173 and 1332 keV γ-rays of ^{60}Co , suppressed and unsuppressed spectra. The spectra are taken from [1]

PT is used to characterise the background in the spectrum. A Single HPGe detector without the CSS will have a PT ratio of ~20% level, where 20% of the counts are in the photopeak and the remaining 80% are in the background. However, once the CSS is used and the HPGe detectors are surrounded by them, the ratio will be $\sim$ 60% for a 1.3 MeV γ-ray.

In γ-ray coincidence spectroscopy this ratio is very important, as the probability of photopeak coincidence follows the PT^n relationship where n is number of coincidence fold. Therefore, the coincidence detection can be improved dramatically by a factor of 9 for doubles, 27 for triples and so on [27].

Chapter 5

High Spin study of ^{156}Er

5.1 Introduction

The Erbium isotopes have been textbook examples of the properties of a deformed nucleus which can exhibit the transformation from collective motion to single particle configurations. The high spin structure of ^{156}Er has been investigated using the Gammasphere array and the reaction ^{114}Cd (^{48}Ca, 6n) at 215 MeV. Similar to the results obtained for the neighbouring ^{157,158}Er isotopes [28] [1], several weak high-energy γ rays have been newly identifed feeding the terminating state in ^{156}Er. The high-lying levels from which these γ rays arise are predicted to represent weakly deformed core-breaking configurations involving energetically expensive 1-particle-1-hole and 2-particle-2-hole proton excitations across the spherical Z =64 shell gap [28] [1].

5.2 Motivation

The generation of angular momentum at extreme values has been studied for over thirty years. These investigations are now more feasible with large, efficient detector arrays such as Gammasphere and heavy-ion beam accelerators. In order

to study the deformed level structure ($\beta \geq 0.2$), the heavy rare earth nuclei (N $\geq$ 90) are some of the best cases.

In the transitional rare earth nuclei regime (N $\sim$ 90), the prolate nucleus can generate angular momentum through collective rotational motion where the rotation occurs is perpendicular to the symmetry axis. The collectively rotating nucleus manifests regular rotational sequences (bands) and I(I + 1) quantum rotor systematics. As the spin increases, the Coriolis-induced alignment of the outermost nucleons occurs, which results in alignment of their spin vectors with the axis of rotation. Therefore, a fraction of the spin will be generated by the single particle contributions of aligned protons and neutrons. Eventually the entire angular momentum is generated by single particle contributions and regular rotational bands terminate [29] (termination in gamma-ray emission spectra) in an oblate non-collective state. The band termination state happens where all the valence particles (outside the $^{146}_{64}Gd_{82}$ doubly magic core in this case) have their spin vectors fully aligned with the rotational axis [30]. In ^{156}Er the band termination occurs at 42 $\hbar$ where all the valence single-particle spins have been aligned.

A high spin study of the Erbium isotopes ^{157,158}Er [1] [31] which were populated during this experiment, confirm the band termination states and the very weakly populated states beyond those states. The Cranked Nilsson Strutinsky calculations which were performed for these nuclei suggest that the high-lying levels from which these γ rays arise represent weakly deformed core-breaking congurations involving energetically expensive 1-particle-1-hole and 2-particle-2-hole proton excitations across the spherical Z =64 shell gap [28].

The main aim of this investigation is to establish states up to and beyond the band termination and also to probe the modes and configurations used by nuclei to generate higher spins. The previous work on ^{156}Er [32] has established the bands of (parity,signature)= (+,0) ,(-,1), (-,0) and (-,1) up to 42, 33(35 tentatively), 40 and 35$\hbar$ respectively.

5.3 The Experimental Details

The high spin structure of the rare-earth nucleus $^{156}_{68}Er_{88}$ has been studied using the ^{114}Cd (^{48}Ca, 6n) fusion evaporation reaction. A 215-MeV ^{48}Ca beam, provided by the 88 Inch Cyclotron accelerator at the Lawrence Berkeley National Laboratory (USA), was used to bombard two stacked thin self- supporting foils of ^{114} Cd, of total thickness of 1.1 mg/cm^2 . The Gammasphere spectrometer, containing 102 HPGe detectors was used to record high-fold γ-ray coincidence events. A total of 1.2$\times$ 10^9 events were collected under the trigger condition that at least seven Compton-suppressed HPGe detectors red in prompt coincidence (γ ^{n}, n$\geq$7). These events were unfolded off-line into 6.5$\times 10^{10}$ quadruple (γ^4) coincidences and replayed into a four-dimensional hypercube for subsequent level-scheme construction.

The 5n and 4n reaction channels of this experiment had been studied in the past [1] [31] and in this thesis the 6n channel was investigated.

The recorded data were previously unfolded into quadruple events (γ^4) coincidence events. In order to study the level scheme of ^{156}Er, the quadruple events were replayed into a Radware format [33] four-dimentional hypercube. The total number of 6.5 $\times$ 10^{10} events (approximately 48 quadruples per event) were incremented to the hypercube which required $\simeq$ 23 GB of Disk space. In this thesis, the 4DG8R program developed by D.C Radford [33] has been used to analyse the γ^4 data. Such analysis is performed through setting the gates on the three of hypercube axes (x,y,z, axes) and the events in coincidence projected out onto the fourth axis. The projected coincidence events will be in the form of a triple gated spectrum which is 1 dimensional spectrum. Lists of the gates as well as 3 dimensional cubes can be constructed and used to enhance the weak structures.

New form of background subtraction [34] was incorporated in the program and was implemented by K.Lagergren [35] is used in this gamma-ray analysis. In order to assign the multipolarities of transitions in ^{156}Er DCO ratio measurements were

carried out. The intensity of γ-rays is measured at a specific fixed angle to the direction of the beam and therefore the angular ratio intensity is defined as:

$$R = \frac{I(35°/145°)}{I(90°)}, \tag{5.1}$$

where I is the intensity of γ-ray .

5.4 ^{156}Er Results

The result of the ^{156}Er level scheme investigation will be discussed in two parts, low spin and high spin. The transitions are ordered based on coincidence, crossover and intensity arguments. The low spin part of the results is up to spin $30\hbar$ where new transitions will be discussed, however the majority of transitions were previously identified [32]. The new very weak transitions feeding into the band terminating state of $42\hbar$ of the ground state band have been observed for the first time.

5.5 Low Spin Structure

The partial level scheme illustrating the low spin (below $30\hbar$) is shown in Figure [5.2]. The DCO ratio measurements were performed and the results confirmed the majority of spin/parity assignment of the previous work on ^{156}Er [32]. The plot illustrating typical DCO ratio values for a number of transitions is displayed in Figure.5.1 and in Table 5.1.

For states weakly populated where the DCO ratio measurement are not feasible, the spin/parity of a state is based on a logical assignment.

5.5.1 Band 1 (+,0)

Band 1 or the ground state band, is previously well established by Stephens et al [32] and the majority of the ordering has been investigated. Moreover, three

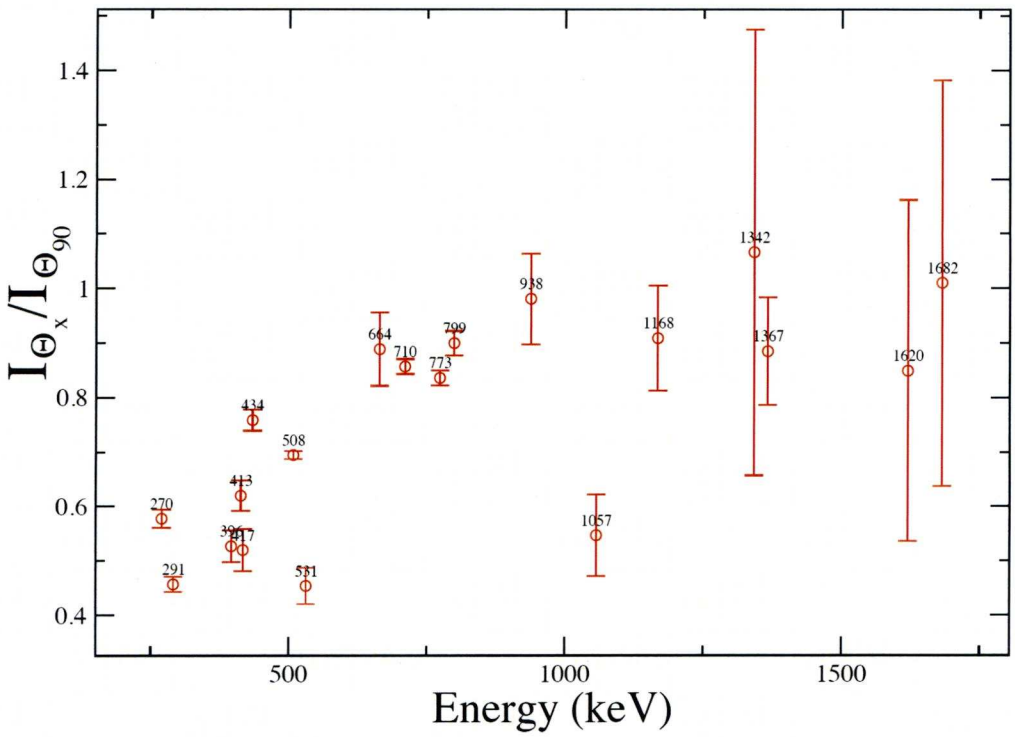

FIGURE 5.1: Typical measured DCO ratio values, in order to validate the result some of the previously know γ rays are also included such as 291, 688 keV.

E_γ (keV)	R	Multipolaritiy	$I_i \rightarrow I_f$	Band
1057	0.54(0.08)	M1	$43^+ \rightarrow 42^+$	$\rightarrow$1
1345	1.06(0.40)	E2	$44^+ \rightarrow 42^+$	$\rightarrow$1
1620	0.84(0.31)	E2	$44^+ \rightarrow 42^+$	$\rightarrow$1
1685	1.01(0.37)	E2	$44^+ \rightarrow 42^+$	$\rightarrow$1
291	0.46(0.02)	E1	$11^- \rightarrow 10^+$	2$\rightarrow$1
270	0.58(0.02)	E1	$10^- \rightarrow 10^+$	3$\rightarrow$1
413	0.52(0.04)	M1	$10^- \rightarrow 9^-$	3$\rightarrow$2
531	0.45(0.03)	E1	$9^- \rightarrow 8^-$	2$\rightarrow$1
509	0.68(0.01)	E2	$13^- \rightarrow 11^-$	2
664	0.89(0.07)	E2	$40^+ \rightarrow 38^+$	1
710	0.86(0.01)	E2	$20^+ \rightarrow 18^+$	1
938	0.98(0.08)	E2	$36^+ \rightarrow 34^+$	1
1168	0.90(0.09)	E2	$38^+ \rightarrow 36^+$	1

TABLE 5.1: Typical measured DCO ratio of γ rays as illustrated in Figure 5.1.

feeding transitions of energies 946, 924 and 957 keV from $22\hbar$, 20 and $18\hbar$ states in band 5 into 20, 18 and $16\hbar$ respectively have also been observed (see Figure 5.3). The states decay via stretched quadrupole transitions (924:R=1.03(0.1) and

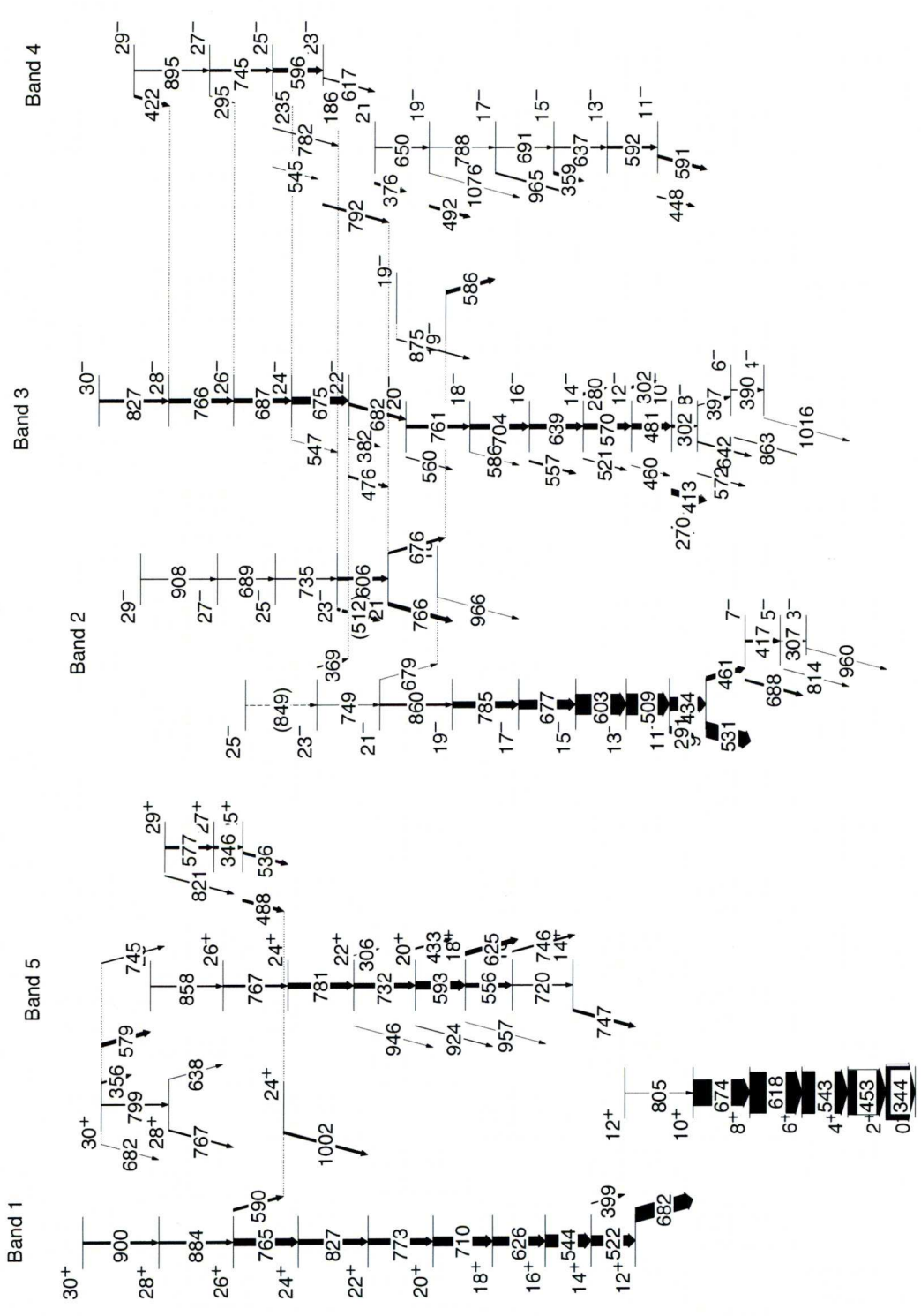

FIGURE 5.2: Low spin part of the level scheme for ^{156}Er illustrating the states below spin $30\hbar$. Transition Energies are given in keV and the width of the arrows is proportional to the intensity of the γ rays .

946:R=1.05(0.53)).

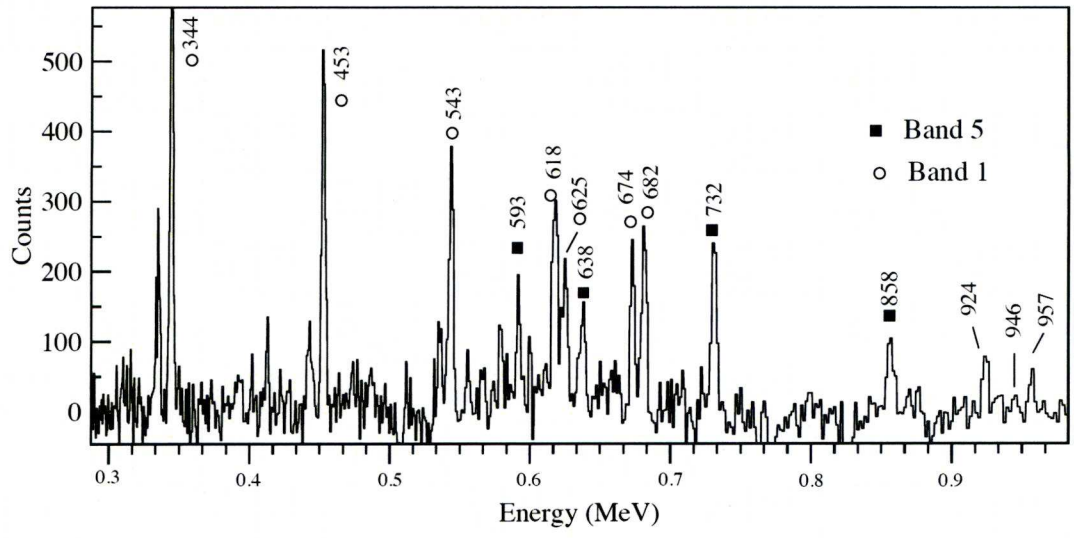

FIGURE 5.3: Spectrum illustrating the 924, 946 and 957 keV transitions feeding in 16, 18 and 20$\hbar$ states in band 1(x=781 y=544 z=522 keV).

Based on an intensity argument (as the spin increases the intensity within a band decreases), the 799 keV transition decaying from 30$\hbar$ state to 28$\hbar$ state is believed to be in band 1.The value of DCO ratio of transitions in band 1 are consistent with that of quadrupole transitions and previously reported spectrum Ref. [32](see Figure 5.1) .

5.5.2 Band 2 (-,1)

Band 2 has been extended down from the previously established band head spin of 7^- [32] to 5^- with the addition of a quadrupole transition of 417 keV. This 5^- decays to 4^+ yrast state of band 1 via a dipole transition of energy 814 keV .

In addition a number of γ rays of energies 560, 586, 557, 521 and 460 keV, decaying from band 3 at spins 20^-, 18^-, 16^-, 14^-, 12^- states respectively have been identified.

5.5.3 Band 3 (-,1)

Band 3 has been extended down from previously reported Ref [32] band head of 6^- to 4^- with the addition of a quadrupole transition of 390 keV. This 4^- state decays to 4^+ yrast state of band 1 via 1016 keV gamma-ray transition. As mentioned in the previous section, the five new γ rays decaying from band 3 into band 2 have been identified. The 521, 557, 562 and 586 keV transitions are displayed in the spectrum in Figure 5.4 which is single triple gated spectrum (x= 687 y=675 z=682 keV).

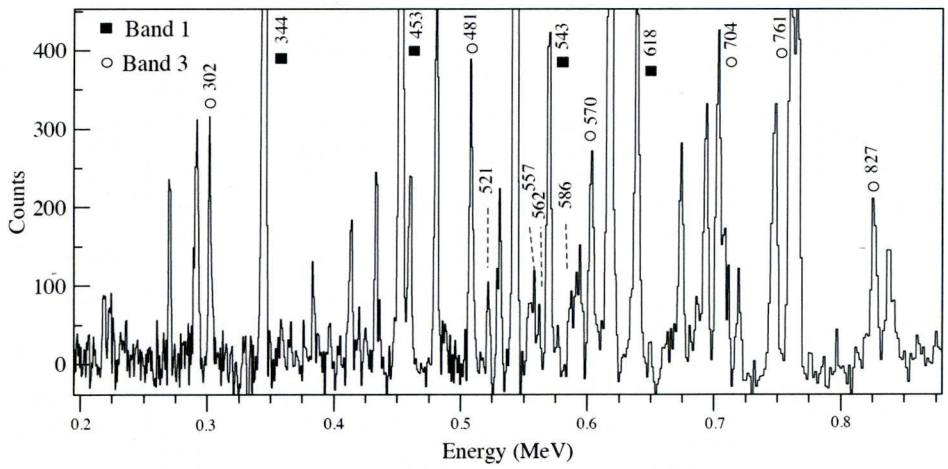

FIGURE 5.4: The spectrum illustrating the 560, 586, 557, 521 and 460 keV transitions feeding in $18\hbar$ and $20\hbar$ states in band 1(x= 687 y=675 z=682 keV).

A new γ ray at an energy of 875 keV has been identified decaying to 18^- state in band 3 from a new 22^- state(see Figure 5.5). A new γ ray at energy of 547 keV has been observed feeding from the 24^- state band 3 to the 23^- state in band 2.

5.5.4 Band 4 (-,1)

A new γ-ray at energy 1076 keV has been identified decaying out of the 19^- state in band 4 into the 17^- state in band 2. Two new γ rays at energies 586, 676 keV have been identified decaying into 17^- state in band 4 from a new 19^- state and 21^- in band 2. Furthermore two γ rays at energies of 235 and 422 keV decaying into

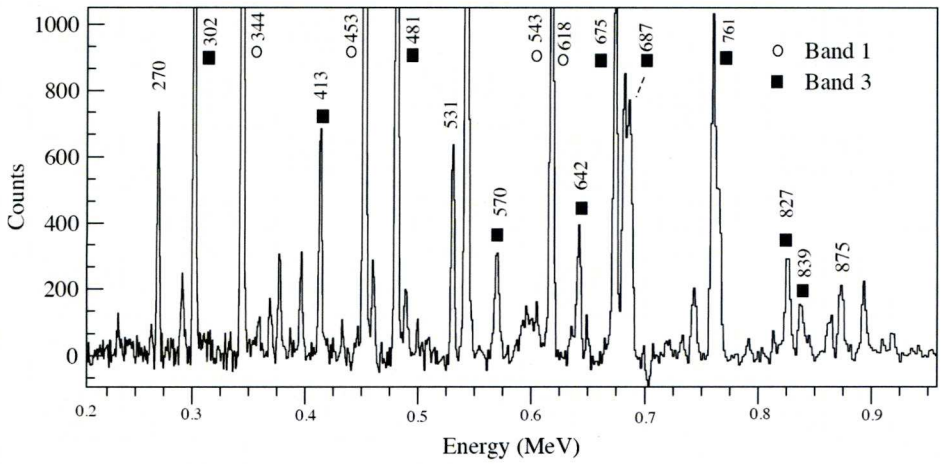

FIGURE 5.5: The spectrum illustrating the 875 keV transition in band 3(x= 639 y=570 z=704 keV).

the 24^- and 28^- states of band 3 have been identified. Some of these transitions are displayed in the spectrum shown in Figure 5.6.

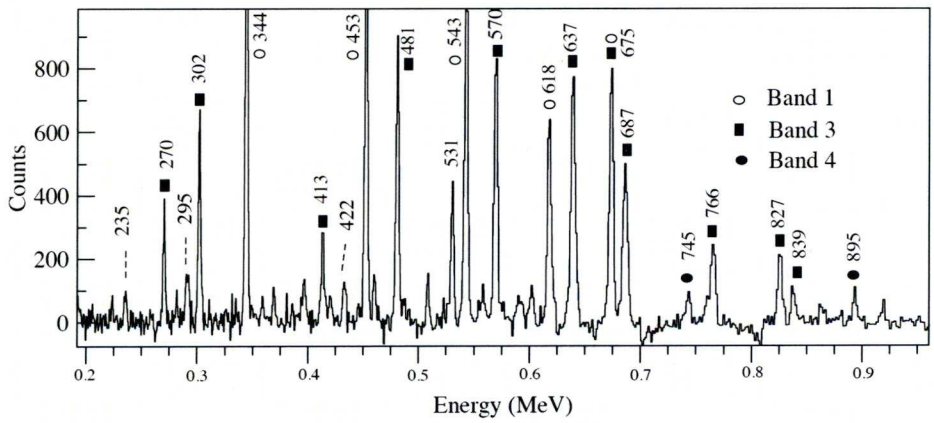

FIGURE 5.6: The spectrum illustrating the 235 and 422 keV transitions decaying into 24^- and 28^- states of band 3(x= 704 y=761 z=682 keV).

5.5.5 Band 5 (+,1)

Band 5 was previously established in Ref. [32] up to $28\hbar$ and the structure and ordering have been confirmed. Three new transitions have been observed decaying into 20^+ and 18^+ states in band 1. Further investigations led to identification of

one more new γ rays at energy of 306 keV decaying from 22^+ into 21^- states in band 2. The spectrum containing the γ ray is shown in Figure 5.7.

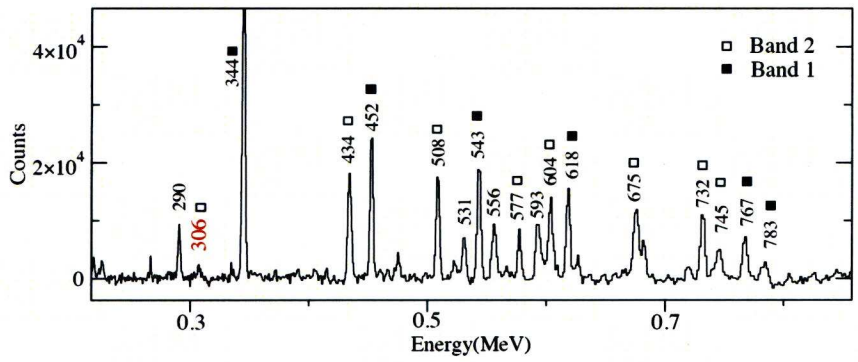

FIGURE 5.7: The spectrum illustrating the 306 keV transition decaying from 22^+ into the 21^- state in band 2(x= 781 y=536 keV).

5.6 High Spin Structure

The partial high spin level scheme of ^{156}Er is shown in Figure 5.6. In the present study, a few weakly populated states beyond band termination states in band 1 and possible band termination states in other bands are identified.

5.6.1 Band 1 (0,+)

Band 1 was previously established up to a 43^+ state (Ref.[32]). In addition, a further four states have been identified feeding to the $42\hbar$ state. Figure 5.6.1 is a sum of triple gated (x= 218, y= 720, z= 799,664,682) quadruple coincidence spectrum of γ-rays.

In order to assign the multipolarities of these transitions the DCO ratio measurement have been performed. The measured properties of those transitions are illustrated in Table 5.2.

Measured properties of γ rays beyond the 42^+ state					
E_γ (keV)	I_γ (%)	R	Multipolaritiy	$I_i \rightarrow I_f$	Band
1057	14.3	0.54(0.08)	M1	$43^+ \rightarrow 42^+$	$\rightarrow$1
1342	4.5	1.07(0.40)	E2	$44^+ \rightarrow 42^+$	$\rightarrow$1
1620	3.9	0.85(0.31)	E2	$(44^+) \rightarrow (42^+)$	$\rightarrow$1
1682	2.1	1.01(0.37)	E2	$(44^+) \rightarrow (42^+)$	$\rightarrow$1
2162	1.9	—	E2	$44^+ \rightarrow 42^+$	$\rightarrow$1

TABLE 5.2: Measured properties of γ ray transitions feeding the 42^+ state in band 1. The intensities (I_γ) are measured relative to 555 keV ($42^+ \rightarrow 40^+$) γ ray .

Above the 32^+ state, this band branches into two decay paths giving two 34^+ states. A new γ ray at energy of 917 keV is identified decaying from the higher lying 34^+ state. The spectrum showing the γ ray is depicted in Figure 5.10.

Above the yrast 36^+state, the band branches into two decay paths. Through the investigation the γ rays in band 1 between spin 38^+ and 40^+ from the previous work Ref. [32] are reordered. The second 38^+ state is believed to decay into the

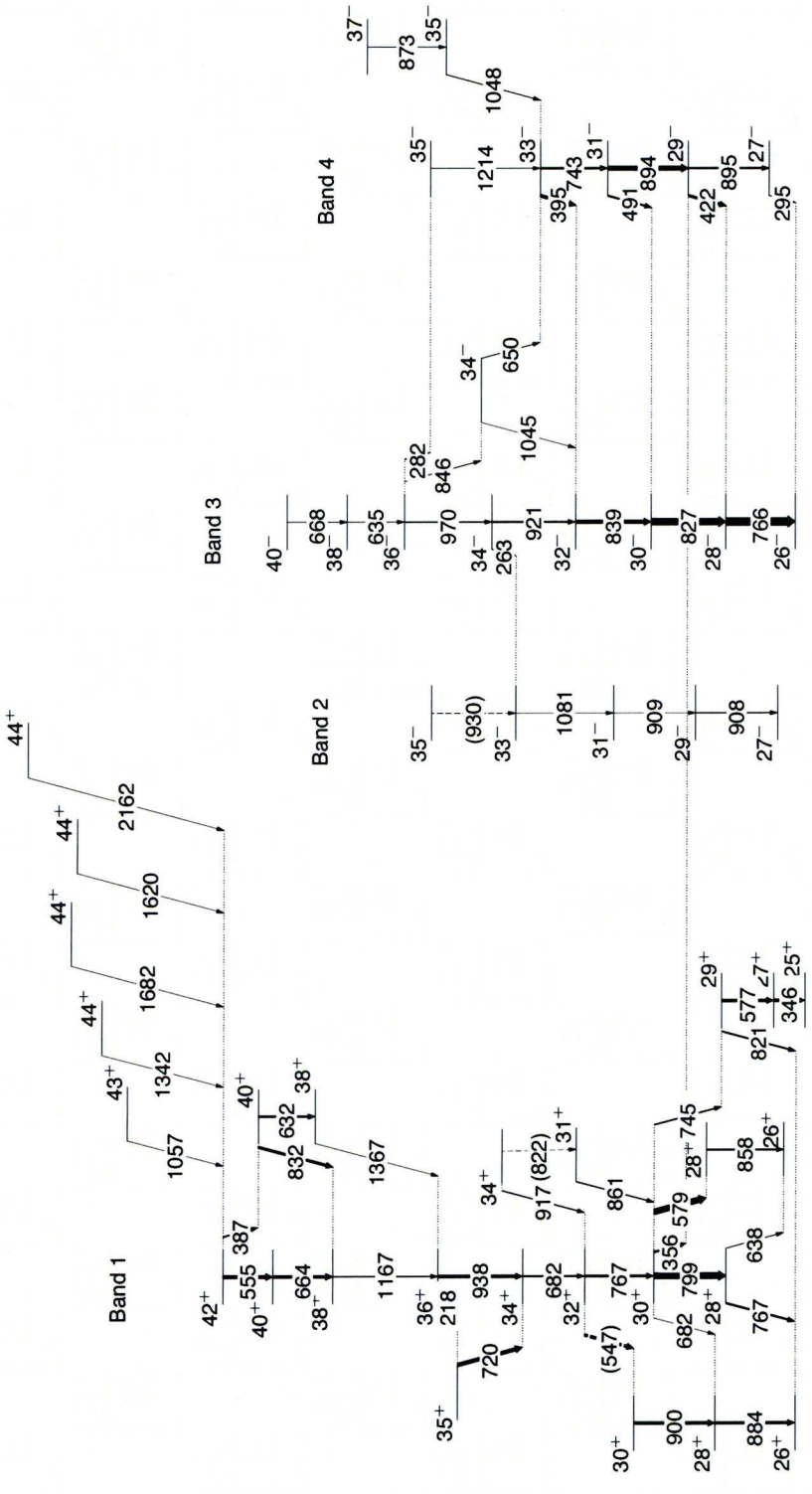

FIGURE 5.8: High spin part of the level scheme for ^{156}Er illustrating the states above spin $30\hbar$. Transition Energies are given in keV and the width of the arrows is proportional to the intensity of the γ rays.

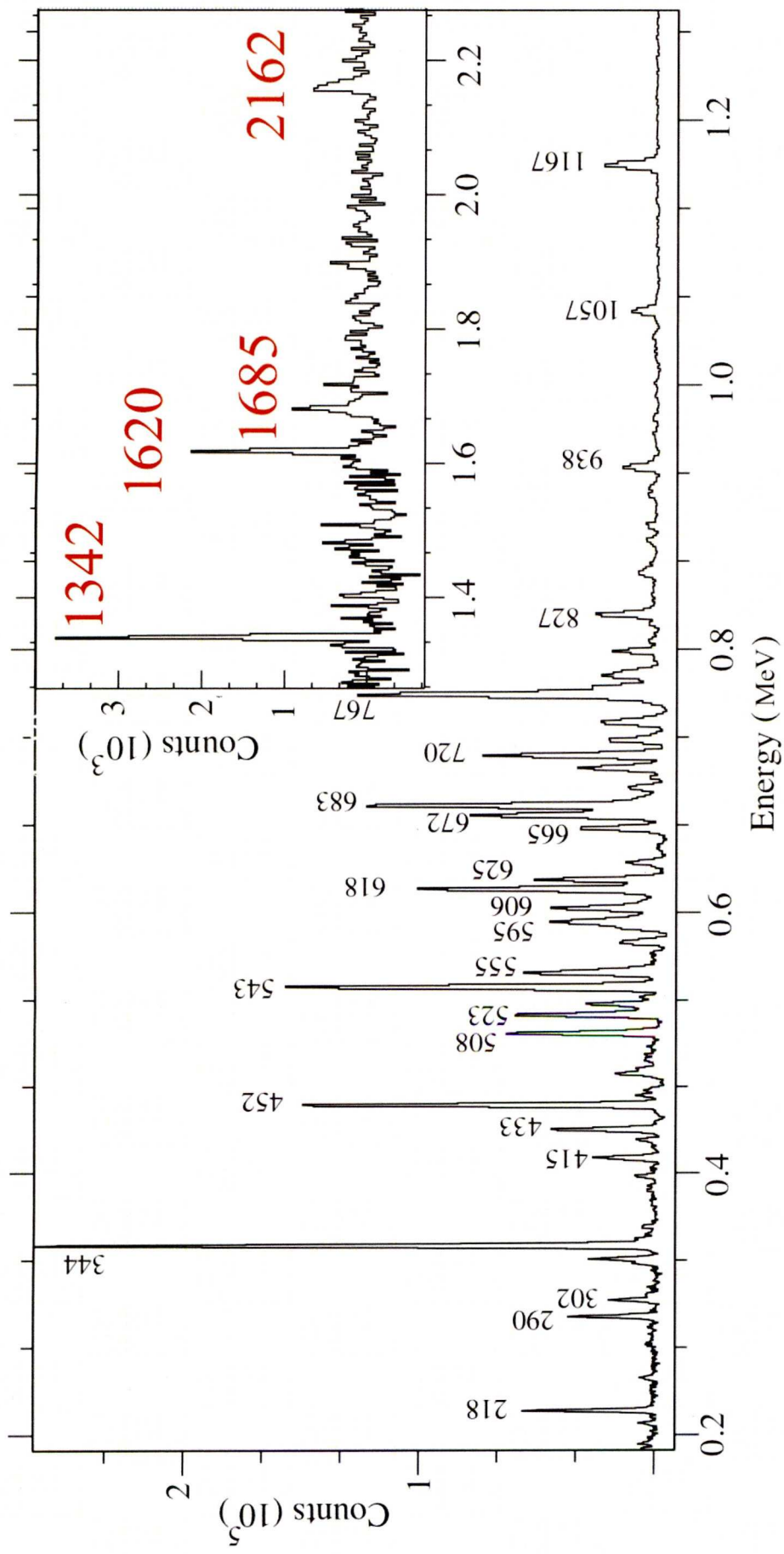

FIGURE 5.9: The spectrum illustrating three newly identified transitions feeding into 42^+ transitions in band 1. The part of the spectrum is magnified in order to illustrate the the transitions beyond terminating state(x= 218, y= 720, z= 799,664,682).

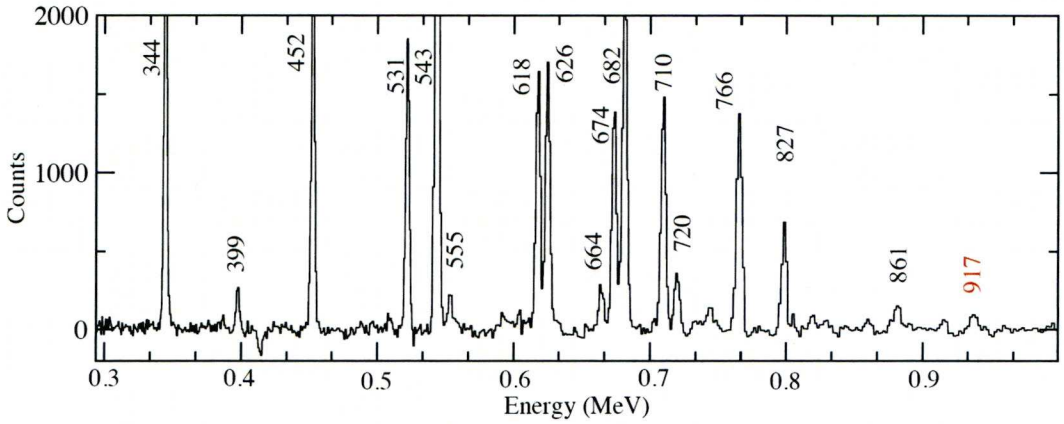

FIGURE 5.10: The spectrum illustrating the new γ-rays at energies of 917 keV in band 1(x= 773 y=765 z=799 keV).

36^+ state via a 1367 keV transition and therefore the 40^+state decay via a 632 keV transition to 38^+state (see Figure 5.6).

5.6.2 Band 2 (-,1)

Band 2 was previously established up to the 31^-state by [32] and through the investigation the ordering is confirmed. Two more γ rays at energies 1081 and 930(tentative) keV are identified decaying in 31^- and 33^-states. Figure 5.11 shows the spectrum including the γ-ray at energy of 1081 keV ($33^- \rightarrow 31^-$) in band 2.

5.6.3 Band 3 (-,0)

Band 3 was previously established up to 38^- state by Stephens et al. [32]. Through the investigation the ordering of this band and second decay path above 32^- state are confirmed. A new γ ray at an energy of 282 keV decaying from 36^- state in band 3 into 35^-state in band 4 has been identified. In addition a new γ ray at an energy of 668 keV has also been observed decaying into the 38^-state in band 3. The spectrum shown in Figure 5.12 illustrates the transition.

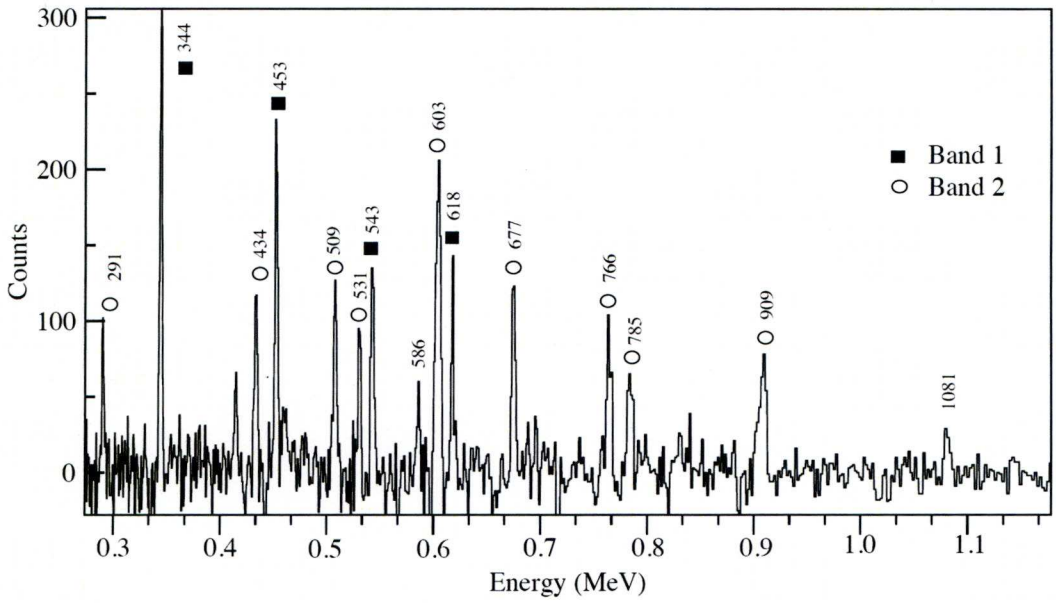

FIGURE 5.11: The spectrum illustrating the new γ ray at energy of 1081 keV ($33^- \rightarrow 31^-$) in band 2(x= 735 y=689 z=908 keV.

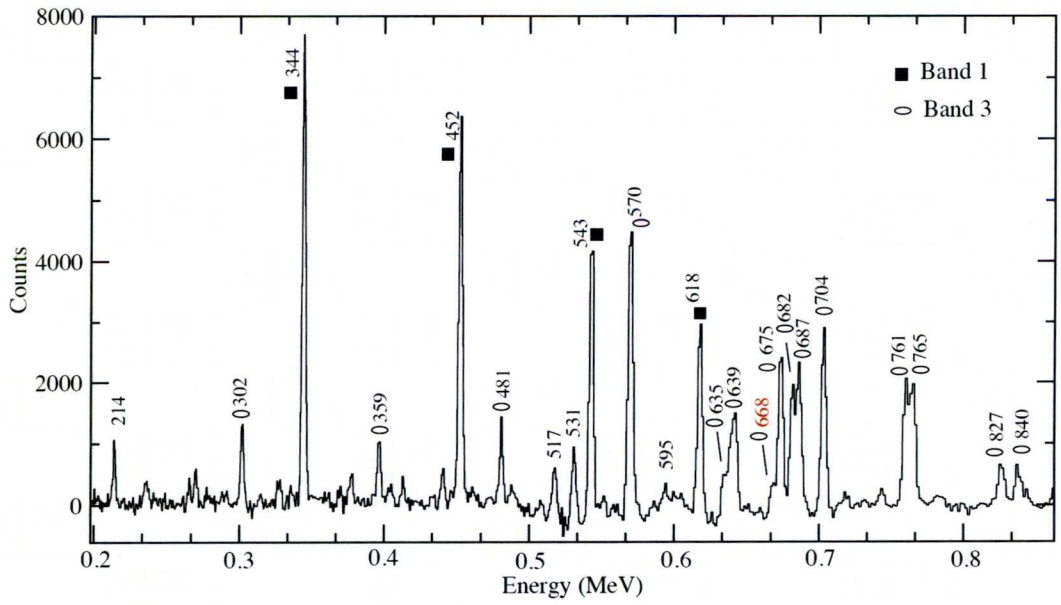

FIGURE 5.12: The spectrum illustrating the new γ-ray at energy of 668 keV in band 3(triple gated spectrum of list of gates including all clean gates from band 3) .

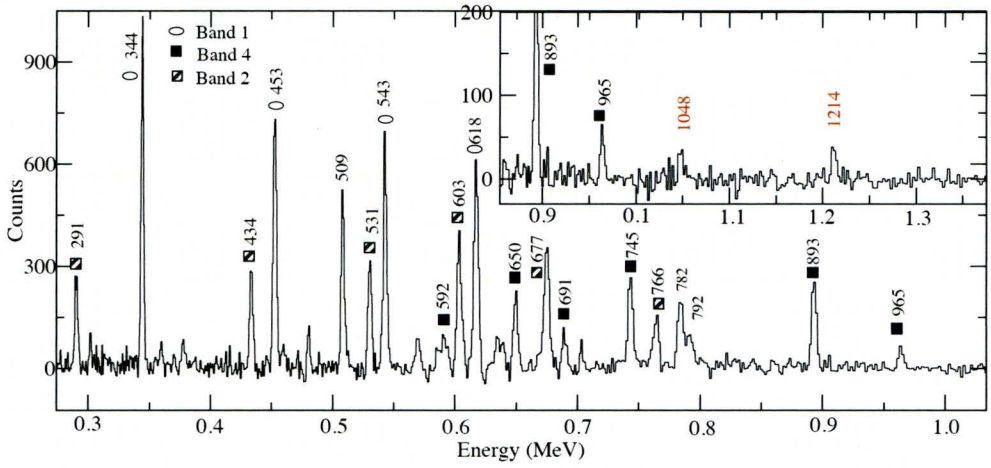

FIGURE 5.13: The spectrum illustrating the new γ rays at energy of 1214 and 1048 keV in band 4(x= 596 y=742 z=895 keV).

5.6.4 Band 4 (-,1)

Band 4 is previously established by Stephens et al. [32] up to the 33^-state. Through the observation of a 1214 keV transition this band has been extended up to a 35^-state. Additionally second 35^- and 37^- states have been observed in this band decaying by 873 and 1048 keV transitions. The spectrum shown in Figure 5.13 illustrates the new 1048 keV transition. A new γ-ray at an energy of 491 keV feeding into 30^- state in band 3 from 31^- state in band 4 has also been observed.

5.7 Discussion

5.7.1 Introduction

In transitional rare earth nuclei the prolate shaped nucleus can generate angular momentum through collective rotational motion. However after a certain number of alignments, the collective prolate shape nucleus changes to a non-collective oblate shape [30]. This demise of collectivity which occurs (at $I \geq 30$) in this region can be as a consequence of the crossing of the yrast low spin part of the rotational band by another less collective configuration which is more favoured in

energy, leading to the observation of an abrupt band termination state. In the case of ^{156}Er, the doubly closed-shell nucleus $^{146}_{64}Gd_{82}$ is assigned as the core of nucleus and therefore the valence nucleons are counted as 10 particles, 6 protons and 4 neutrons. Through the alignment of 10 particles, a maximum spin of $42\hbar$ can be reached when the band terminates and therefore in order to produce higher-spin states, particle-hole excitation is required.

In order to assign the specific single particle configuration to a specific state in the level scheme, the theoretical calculation which was previously performed by I.Ragnarsson [4] has been used. The theoretical calculation has been performed in the formalism of the Cranked-Nilsson Strutinsky framework [36, 37]. This type of calculation ignores the pairing effect and treats the collective and non-collective states in same way. It allows the construction of different bands in a fixed configuration, specified by a number of particles in a different oscillator N-shell and to search for the lowest energy state in that Particle configuration.

Figure 5.14 shows the prediction for the ^{156}Er nuclei from such a theoretical calculation. In this type of plot, known as rigid rotor plot, the excitation energy is plotted minus the standard rigid rotor reference versus angular momentum. The rigid rotor reference is defined in [3] :

$$E_\gamma = \frac{\hbar^2}{2\Im} I(I+1), \tag{5.2}$$

The rigid rotor moment of inertia [38] is normalised to ^{158}Er:

$$\frac{\hbar^2}{2\Im} = 0.007(\frac{158}{A})^{\frac{5}{3}} \tag{5.3}$$

5.7.2 Band 1, (+,0)

Band 1 which is the ground state band (GSB) was previously seen up to the 42^+ band terminating state and in addition to one more transition feeding to this state from a 43^+ state. Through the investigation, four more transitions belonging to

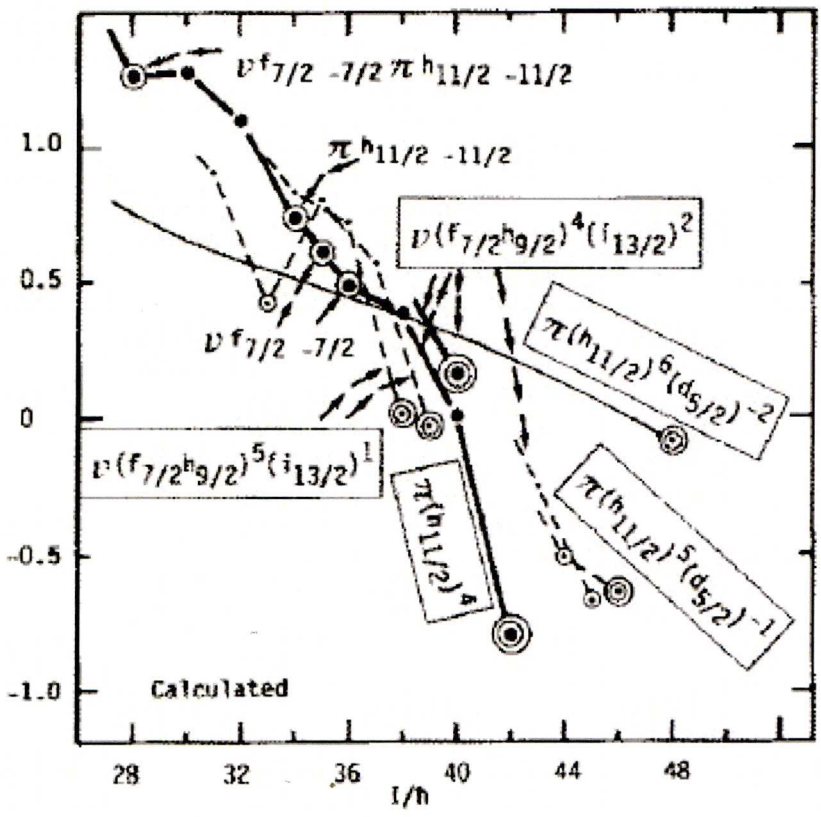

FIGURE 5.14: Calculated states in the yrast region of ^{156}Er with the configuration terminating at 42^+ specially marked (double circled). The calculated aligned states and the corresponding observed states are encircled. Two circles are used for the calculated fully aligned states. The plot is taken from [4].

the region of beyond band termination state have been observed and identified. Figure 5.15 shows a plot of experimental alignments as a function of rotational frequency for the GSB. The Harris parameters [39] used in this plot are $\Im_0$= 15 MeV^{-1} $\hbar^2$ and $\Im_1$= 90 MeV^{-3} $\hbar^4$.

The GSB which is the yrast (+,0) sequence starts off from the quasiparticle vacuum (or 0 qp) state at low spin and exhibits the collective rotational motion of a prolate shaped nucleus. It is followed by first alignment of a pair of $i_{13/2}$ neutrons at $\hbar\omega \simeq 0.3$ MeV, the crossing of two-quasineutron configuration, leading to the observation of backbend as is shown in Figure 5.15.

Through this crossing the band carries an alignment of $\simeq 10\hbar$. The GSB remains prolate up to $30\hbar$ where it suddenly changes its mode to oblate non-collective

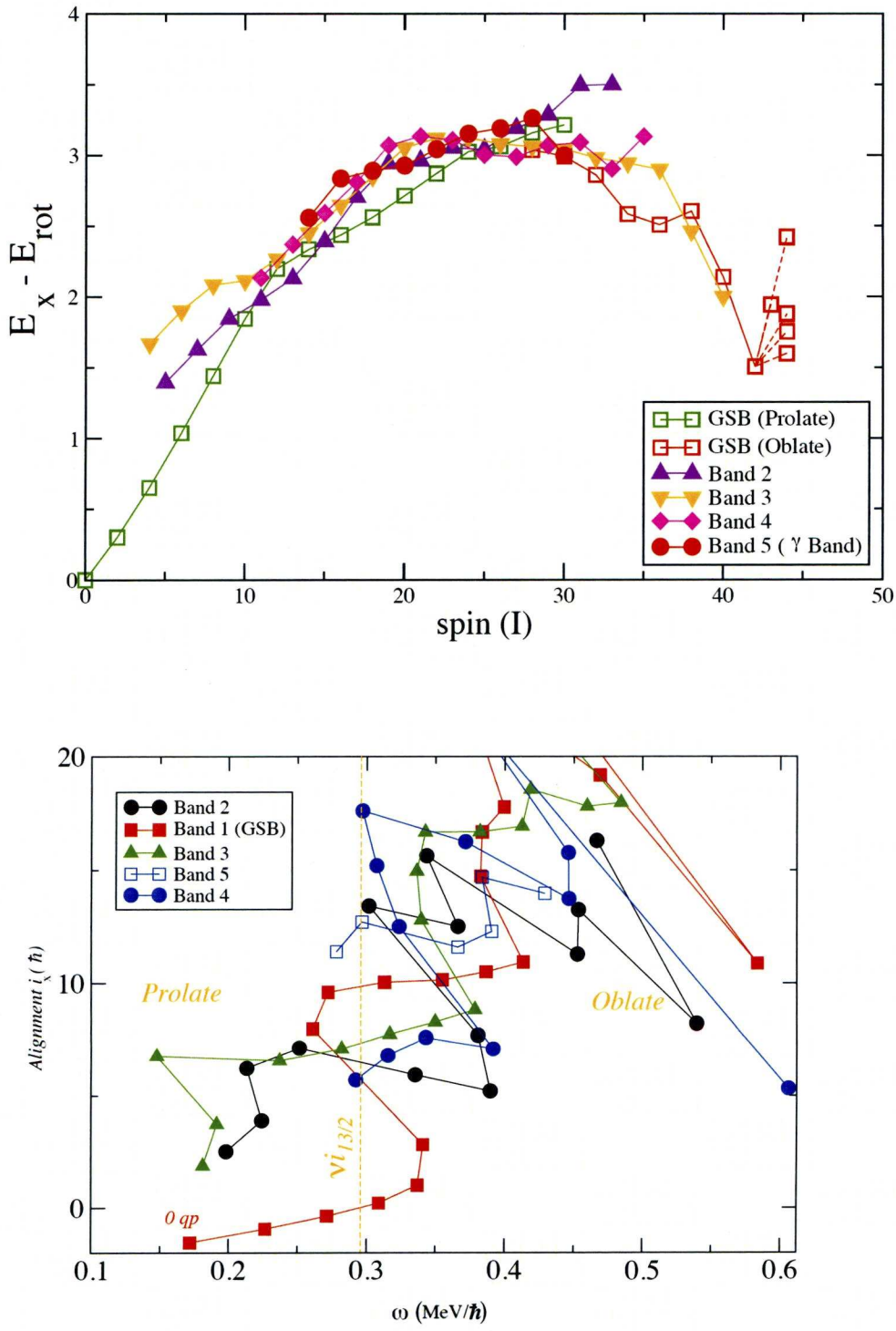

FIGURE 5.15: Experimental rigid rotor versus spin, $I\hbar$ (top) and alignment ,i versus rotational frequency $\hbar\omega$ for the bands in ^{156}Er. The band crossing which is illustrated in the bottom plot corresponds to first $i_{13/2}$ neutron crossing. The Harris parameters of J_0= 15 MeV^{-1} $\hbar^2$ and J_1= 90 MeV^{-3} $\hbar^4$ have been used.

mode. It then continues through oblate configurations up to 42 $^{+}$ state where all the valence particles' spin vectors are fully aligned. According to [4] and also as it is shown in Figure 5.14 the fully aligned 42^{+} state which is observed experimentally in this nucleus has the configuration of : $\pi[(h_{11/2})^4]\otimes \nu[(f_{7/2})^2(h_{9/2})^2(i_{13/2})^2]$. Figure 5.15(upper) shows the experimental rigid rotor plot for the different bands. It can be observed from the plot that the down sloping of the GSB which reveals the point that 42^{+} state is favoured in energy. According to [4], the 36^{+} state in the GSB compared to the 42^{+} state (the terminating state) is formed from the rearrangment of $\nu(f_{7/2,5/2}\rightarrow h_{7/2,-7/2})$. Also the 34^{+} state is formed from rearrangment of one proton, $\pi(h_{11/2,5/2}\rightarrow h_{11/2,-11/2})$. Similarly the observed 35^{+} state in the GSB is believed to be formed by rearrangment of one neutron, $\nu(h_{9/2,7/2}\rightarrow f_{7/2,-7/2})$. The second pathway, just before the terminating state in the GSB results in the observation of second 40^{+} and 38^{+} states in the band. According to the theoretical calculations [4], the 40^{+} state has a configuration of $\pi[(h_{11/2})^4]\otimes \nu[(f_{7/2})^3(h_{9/2})(i_{13/2})^2]$ and consequently the second 38^{+} state can be assigned as part of the band termination for this second 40^{+} state. As was previously suggested [4], the arrangement of this pathway, based on intensity argument is reorded. Based on the theoretical calculation [4], the yrast states of ^{154}Dy reported in Ref[5] in the I$\geqslant$40 region and ^{156}Er have similar configurations except that in ^{154}Dy, 2 more proton-holes in the $d_{5/2}$ subshell contributes to aligned 44^{+} and 46^{+} states (with addition of 2 and 4 spin units). Figure 5.16(right) shows the observed positive parity states in $^{156}_{68}Er_{88}$ and $^{154}_{66}Dy_{88}$ in I$\geqslant$30 spin region. One can observe the striking similarities between the two nuclei. It suggests that the 44^{+} state in ^{154}Dy can be formed from breaking the I = 0 coupling of the $d_{5/2}$ holes. Therefore, the 42^{+} state is less favoured in ^{154}Dy than in ^{156}Er. Similarly in the observed spectrum of ^{158}Yb reported in Ref. [40] , the positive-parity yrast band of this nucleus exhibits a very similar behaviour to that of ^{154}Dy and ^{156}Er. This might suggest that the I = 30-40 spin region in all of these three N = 88 isotones is formed by $4(h_{11/2})$ protons (together with the valence neutrons) while the additional two holes (for Z = 66) or two particles (for Z = 70) couple to spin zero.

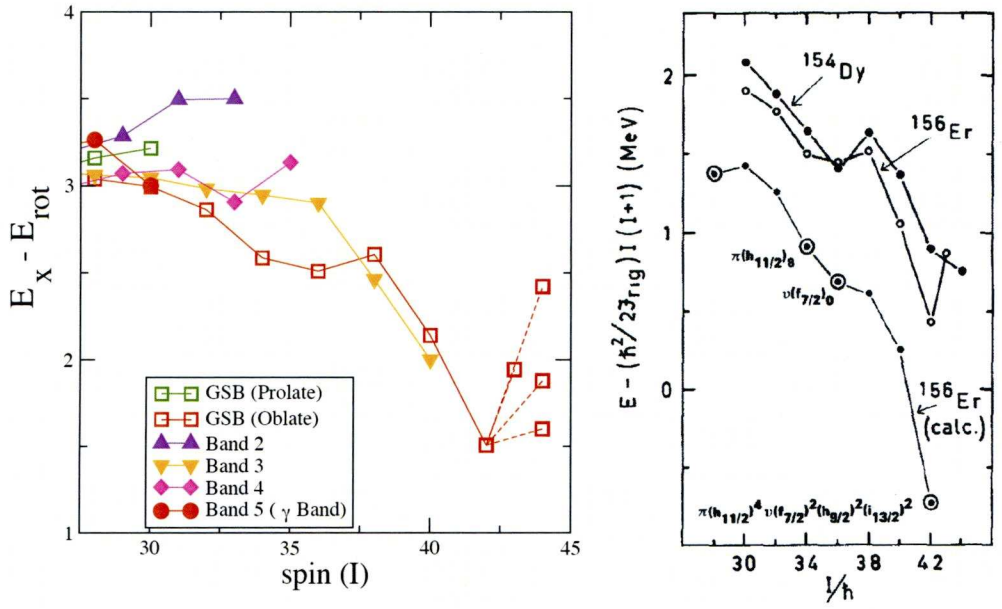

FIGURE 5.16: Experimental rigid rotor plot of bands in ^{156}Er deduced through current work (left) and the experimental rigid rotor plot of positive parity bands in ^{156}Er and ^{154}Dy (right) in the I≧30 spin region is depicted in Figure. One can observe the striking similarities beween two isotones, the plot is taken from [5].

5.7.3 The Side Bands

The other side bands in ^{156}Er have quasineutron configurations made by $i_{13/2}$ neutrons, the orbital which is the lowest energy positive parity orbital and another quasineutron occupying the next lowest in energy the negative parity. In these bands, the crossing of the first pair of $i_{13/2}$ neutrons due to presence of a quasineutron in orbital is blocked. The first alignment for these band would therefore be the second pair of $i_{13/2}$ neutrons.

The side bands 2, 3 and 4 remain prolate up to their first alignment (the second pair of $i_{13/2}$ neutrons) which occurs at $\hbar\omega \simeq 0.36$ MeV and carry the same amount of alignments ($\simeq 6\ \hbar$) for each (as is illustrated in Figure 5.17). Band 2 remains prolate and exhibits collective rotational motion up to about the first alignment. Just after the crossing, the band changes its mode from collective prolate to non-collective oblate shape and it reaches a maximum spin of $33^-\ \hbar$ (35^- tentatively).

The same senario occurs for band 4 where it faces the first alignment and changes to oblate mode and reaches the maximum spin of 35 $\hbar$. The 33^- state in band 4 is more favoured in energy and can be assigned to similar configuration to band 2. According to Ref [4] 33^-(35^-) state in ^{156}Er is formed by rearrangment of $\nu(h_{9/2,5/2} \rightarrow f_{7/2,-7/2})$ compared to 39^- state in band 3. Band 3, similar to other negative parity bands changes its mode from collective prolate to non-collective oblate shape after its first alignment at about the 21^- state. It then reaches to maximum spin state of 38^-(40^- tentativley) where it terminates. The teminating states in this band are very favoured energetically and it can be seen from the plot depicted in Figure 5.15 that they are much more favoured over the last two spin units as it is sloping strongly down. According to calculation [4] the 38^-, 39^- states are corresponding to the rearrangment of $\nu(i_{13/2} \rightarrow f_{9/2})$and $\nu(i_{13/2} \rightarrow h_{9/2})$ relative to the 42^+ state.

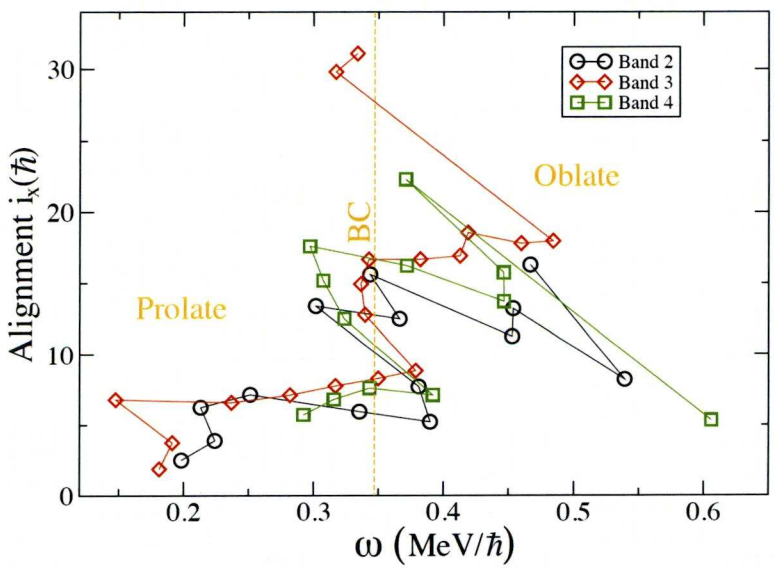

FIGURE 5.17: Experimental alignment, i versus rotational frequency $\hbar\omega$ for the negative parity bands in ^{156}Er. The band crossing which is illustrated in the plot corresponds to first $i_{13/2}$ neutron crossing. The Harris parameters of J_0= 15 MeV^{-1} $\hbar^2$ and J_1= 90 MeV^{-3} $\hbar^4$ have been used.

5.7.4 Beyond Band Termination State

From rigid rotor plot depicted in Figure 5.15, one can observe the favoured nature of 2 terminating states (GSB and band 2) and the transitions beyond band termination state in GSB which are much less favoured in energy. Four more transitions (five in total) at energy of 1345, 1620, 1685 and 2158 keV have been observed in ^{156}Er. In order to assign the multipolarities of these transitions, the DCO ratio measurement have been performed. The ratio of the previously known transition, 1057 keV is consistent with that of a stretched Dipole transition (and assumed as M1) and the three new transitions' are consistent with that of quadrupole transitions (and assumed as E2). They carry about $\simeq$30% of the total intensity of terminating state. The Nilsson-Strutinsky calculations were performed by Ingemar Ragnarsson and Tord Bengtsson for this nucleus (see Ref [4]) and for ^{157,158}Er [31][1]. It is suggested that the states are from particle-hole excitation across the Z=64 shell-gap. In particular, the 44^+ states which were observed during this work might have been formed through one-particle-one-hole excitation across the spherical Z=64 shell gap($\pi(d_{5/2}/g_{7/2} \rightarrow d_{3/2})$). The favoured way to create higher spin states in the I=40-50$\hbar$ yrast states is to make the holes in $d_{5/2}$ orbital below the Z=64 shell-gap and to place the excited particles to $h_{11/2}$ orbitals.

5.7.5 Conclusion

The present study investigates states of ^{156}Er up and beyond the band termination state. The measured properties and a theoretical calculations reveal the different behaviour of the nucleus as it reaches to higher spin states, especially at extreme values. Similar to the results obtained for the neighbouring ^{157,158}Er isotopes, several weak high-energy γ rays have been newly identifed feeding the terminating state in ^{156}Er. The high-lying levels from which these γ-rays arise are predicted to represent weakly deformed core-breaking configurations involving energetically expensive 1-particle-1-hole and 2-particle-2-hole proton excitations

across the spherical Z =64 shell gap [1]. The measured properties and the theoretical calculations of the transitions beyond the band terminating state reveal the nature of these transitions arising from particle-hole excitations across Z=64 shell-gap.

Chapter 6

High Spin study of ^{130}Ce

6.1 Introduction

The neutron-deficient Cerium isotopes near A≈130 have been previously reported to have a deformed prolate shape (β_2≈0.25) [41]. The ^{130}Ce nucleus lies in a well known region which manifests softness in the potential energy surface with respect to the γ, the triaxiality coordinate in polar representation of a rotating quadrupole shape [42]. Therefore, the overall shape of the nuclei is regulated by the occupied quasi-particle orbitals close to the Fermi surface which are able to polarise the core[43]. For instance, the orbitals from bottom of the $\pi_{h_{11/2}}$ (N=5) and from top of the $\nu_{h_{11/2}}$ shell drive the nuclear shape to near prolate shape (γ=0°) and collective oblate shape (γ = -60°) respectively. Furthermore ^{132}Ce, in this region, was the first case in which a superdeformed band of discrete γ-rays , corresponding to a (β_2≈0.4) prolate nuclear shape having a 3:2 ratio of the major to minor axes was established at high spin [44, 45]. The high spin structure of ^{130}Ce has been investigated using the Eurogam phase II spectrometer [25]. Previously through the study performed by E.S. Paul, et al [44] several weakly populated SD bands have been identified and assigned to ^{130}Ce and their properties were studied. The present study concentrates on the spectroscopy of normally deformed (β_2≈0.2) structures in ^{130}Ce.

Compared to previously reported structures [44–46], 6 new bands including four high spin coupled bands have been identified for the first time and existing structures have been extended to higher spin.

Two of the new configurations were found to be populated more weakly than the previously reported SD bands. The 6 new bands were placed in a comprehensive level scheme for ^{130}Ce; four ΔI=1 bands have been observed together with two ΔI=2 structures.

Cranked Wood-Saxon calculations have been performed for ^{130}Ce in order to interpret the configurations and the experimental features observed in this study.

6.1.1 Experimental Details

The high spin states in ^{130}Ce were populated using the ^{100}Mo(^{34}S,4n) fusion evaporation reaction. A 155 MeV ^{34}S beam provided by the Vivitron electrostatic accelerator at the Centre de Recherches Nucleaires, Strasbourg bombarded two self-supporting foils of ^{100}Mo of total thickness of 1.2 mg/cm^2. The Eurogam phase II spectrometer containing 54 Compton-suppressed HPGe [47] including 24 segmented (four element) "clover" detectors, was used to record high-fold γ -ray coincidence events. A total of 6.5×10^6 events were collected under the trigger condition that at least five Compton-suppressed HPGe detectors fired in prompt coincidence (γ^n, n $\geqq$5). Due to the neutron deficient nature of the compound nucleus (^{134}Ce), significant charged particle evaporation as well as pure nuetron evaporation occurred and a lot of nuclei in mass region of Z=54-56 were populated during the experiment. Table 6.1 illustrates the relative yields of nuclei produced in this experiment, as it can be seen from that ^{130}Ce represents approximately 50% of the data.

Relative yields of nuclei produced in this experiment		
Nucleus	Channel	Relative yield(%)
^{130}Ce	4n	≡100
^{129}Ce	5n	60
^{131}Ce	3n	16
^{132}Ce	2n	1
^{131}La	p2n	5
^{130}La	p3n	15
^{129}La	p4n	28
^{128}La	p5n	1
^{128}Ba	α2n	11
^{127}Ba	α3n	15
^{130}Ba	αn	10
^{126}Ba	α4n	19

TABLE 6.1: The yields of the nuclei are measured relative to 254 keV ($2^+ \rightarrow 0^+$) γ-ray in ^{130}Ce.

6.2 Data Analysis Techniques

Through analysing the data, each event can be unfolded into several lower fold event such as triple coincidence event and even quadruple coincident events. In this way, high-fold coincident events can contribute to the number of lower fold events. The events were unfolded off-line into quadruples (γ^4) events and replayed into a four-dimensional hypercube for subsequent level-scheme construction.

In this thesis, the 4GD8R program developed by D.C.Radford [33] has been used to analyse the γ-γ-γ-γ data. Setting the gates on the three axis of the hypercube(x,y,z axes) will project out the in coincidence events onto the fourth axis.The projected events will be in the form of 1 dimensional triple gated spectra.

However for the weak structures, a triple (γ^3) coincidence analysis has been done. Similar to analysis of ^{156}Er mentioned in Chapter 5 the new form of background subtraction [34] was used. The Directional Correlational of Oriented states (DCO) method was carried out to gain information on the multipolarities of transitions in ^{130}Ce. In this method the event recorded at 90° (by the central Clover detectors) with respect to beam direction along with, events recoded at extreme forward and backward detectors (5 detectors at 22.4° plus 5 at 157.6°) were sorted against each

other to form a 2D matrix. In order to find a clear spectrum (solely corresponding to ^{130}Ce) the matrix can be gated in the sort. An DCO ratio can be obtained from:

$$R = \frac{I(157°/22°)}{I(90°)}, \tag{6.1}$$

where I_γ is the measured γ-ray intensity.

The obtained DCO ratio will discriminate between dipole and quadrupole transitions. The plot illustrating the typical DCO ratio values for number of transitions is displayed in Figure.6.1 Stretched-quadruple character (ΔI=2) transitions give values of $\approx$1.0 while stretched dipole transition (ΔI=1) give values of $\approx$0.5. For weakly populated states where the DCO ratio measurement is not feasible the spin parity assignment is based on logical arguments.

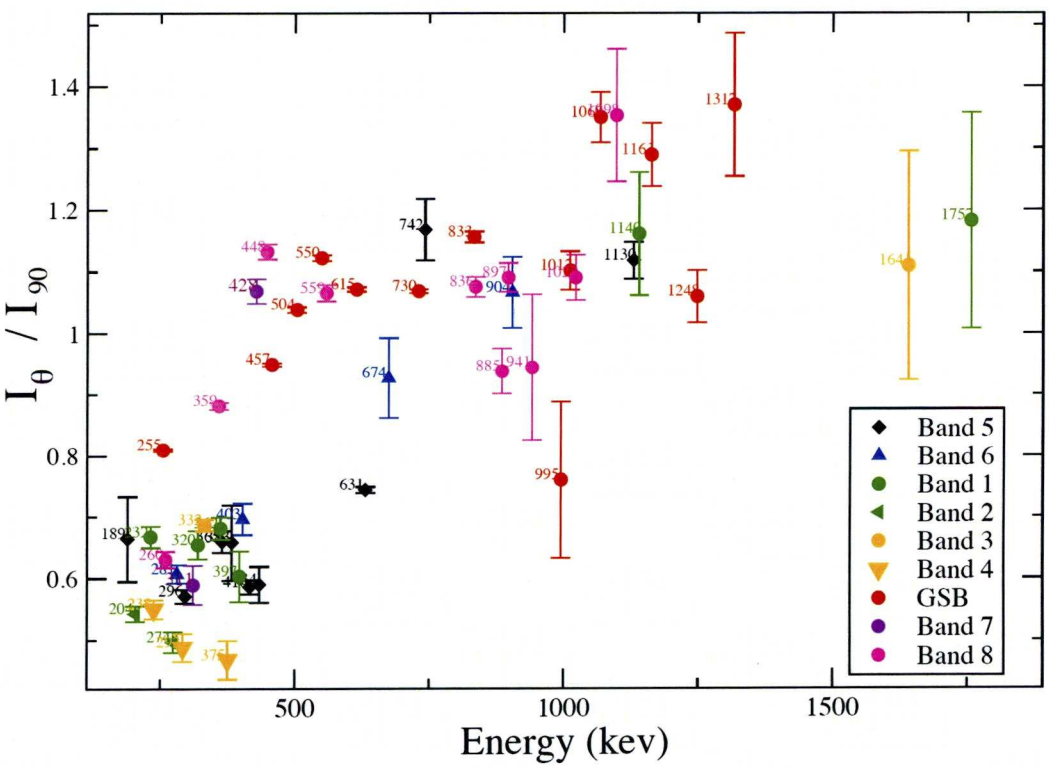

FIGURE 6.1: Typical measured DCO ratio values from the investigation, in order to validate the result some of the previously know γ rays are also included.

6.3 Experimental Results

In this section the results of the ^{130}Ce level scheme investigation will be discussed in two main parts, ΔI=2 where the collective E2 transitions dominated the in-band decays and ΔI=1 M1/E2 where dipole transitions dominate and manifest weak E2 crossover transitions. The complete level scheme illustrating new structures is shown in Figure 6.2.

6.3.1 The ΔI=2 bands

6.3.2 Ground state band(+,0)

The ground state band (GSB) is previously well established by E.S.Paul et al. [46] and D.M.Todd et al. [44] and the majority of the ordering has been investigated. Moreover, a second decay path above the yrast $8\hbar$ state has been found with the addition of a 994 keV transition. Through the observation of two more γ-rays at energies of 237 and 267 keV transitions the position of the new $10\hbar$ state is confirmed. A spectrum illustrating the new 994 keV transition is shown in Fig 6.3.

The energies and relevant properties of the γ-rays in the ^{130}Ce level scheme are shown in table 7.4.

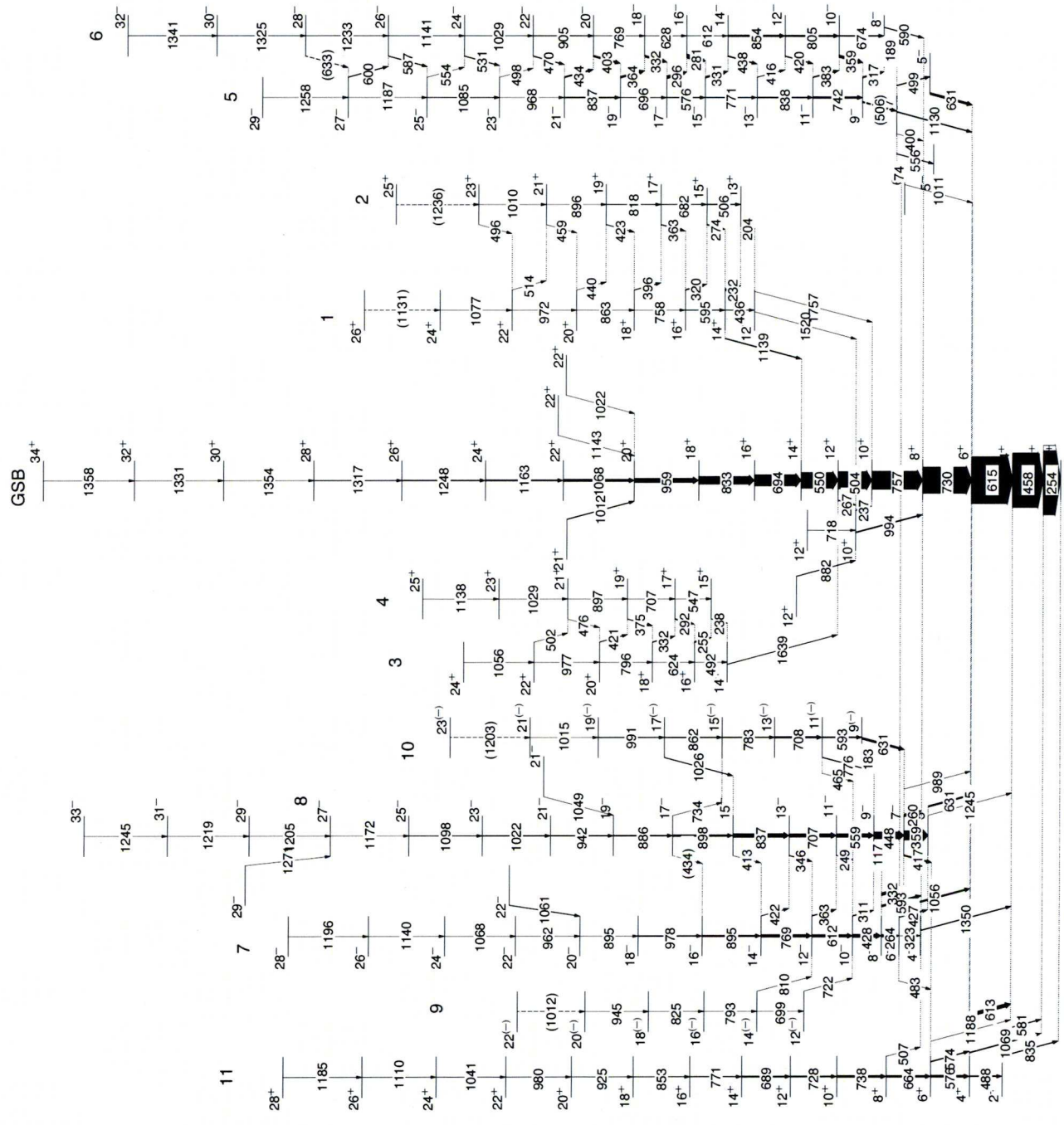

FIGURE 6.2: The level scheme for ^{130}Ce . Transition Energies are given in keV and the width of the arrows is proportional to the intensity of the γ rays .

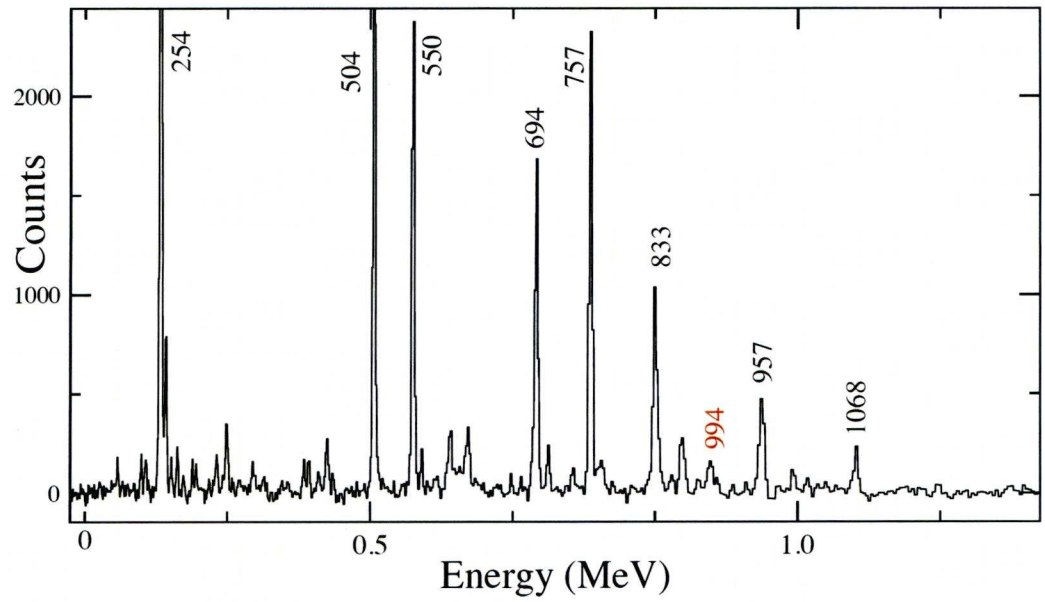

FIGURE 6.3: The triple gated spectrum (x = 730, y = 615 and z = 458) illustrating the new γ ray at energy of 994 keV in ground state band .

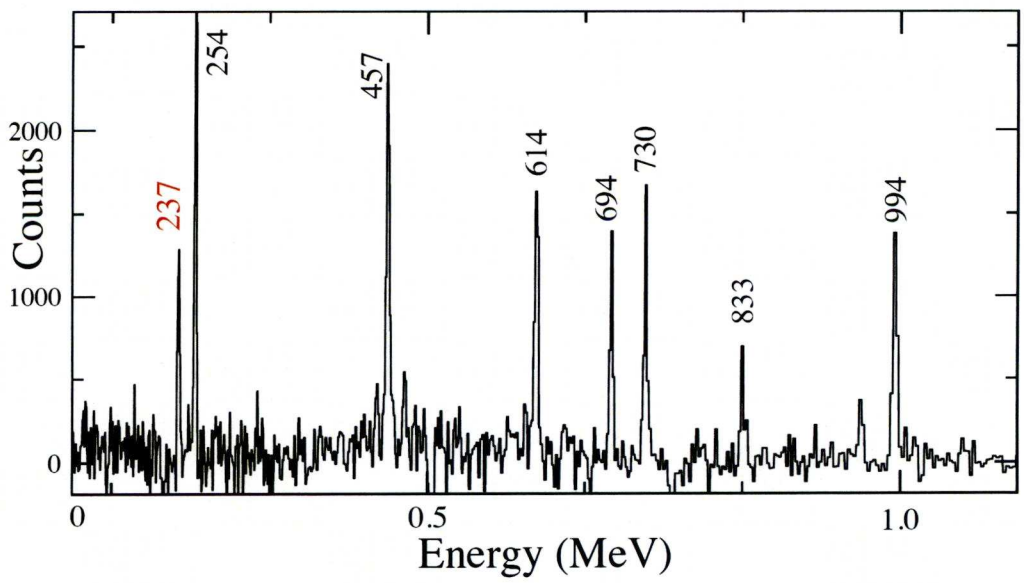

FIGURE 6.4: The double gated spectrum (x = 267 and y = 550) illustrating the new γ rays at energy of 994 and 236 keV in ground state band.

E_γ (keV)	I_γ (%)	R	Multipolarity	$I_i \rightarrow I_f$	Band
254	≡100	0.81(16)	E2	$2^+ \rightarrow 0^+$	GSB
458	83.97	0.95(8)	E2	$4^+ \rightarrow 2^+$	GSB
615	66.45	1.071(37)	E2	$6^+ \rightarrow 4^+$	GSB
730	41.12	1.068(9)	E2	$8^+ \rightarrow 6^+$	GSB
757	26.17		(E2)	$10^+ \rightarrow 8^+$	GSB
504	26.03	1.038(3)	E2	$12^+ \rightarrow 10^+$	GSB
550	23.29	1.12(1)	E2	$14^+ \rightarrow 12^+$	GSB
694	16.9			$16^+ \rightarrow 14^+$	GSB
833	11.58	1.15(2)	E2	$18^+ \rightarrow 16^+$	GSB
959	796			$20^+ \rightarrow 18^+$	GSB
1068	3.67	1.35(16)	E2	$22^+ \rightarrow 20^+$	GSB
1163	1.74	1.289(40)	E2	$24^+ \rightarrow 22^+$	GSB
1248	1.12	1.05(4)	E2	$26^+ \rightarrow 24^+$	GSB
1317		1.37(12)	E2	$28^+ \rightarrow 26^+$	GSB
1354				$30^+ \rightarrow 28^+$	GSB
1331				$32^+ \rightarrow 30^+$	GSB
1358				$34^+ \rightarrow 32^+$	GSB
994	1.57	0.76(15)	(M1)	$10^+ \rightarrow 8^+$	→GSB
237				$10^+ \rightarrow 10^+$	→GSB
267				$12^+ \rightarrow 10^+$	→GSB
718				$12^+ \rightarrow 10^+$	→GSB
882				$12^+ \rightarrow 10^+$	→GSB
1022				$22^+ \rightarrow 20^+$	→GSB
1012				$22^+ \rightarrow 20^+$	→GSB
1143				$22^+ \rightarrow 20^+$	→GSB
260	4.29	0.63(1)	M1	$7^- \rightarrow 8^+$	8 →GSB
590				$8^- \rightarrow 8^-$	6→GSB
674	1.37			$10^- \rightarrow 8^-$	6
805	2.26	0.98(10)	E2	$12^- \rightarrow 10^-$	6
854	2.62	0.63(1)	M1	$14^- \rightarrow 12^-$	6
612				$16^- \rightarrow 14^-$	6
628				$18^- \rightarrow 16^-$	6
769				$20^- \rightarrow 18^-$	6
905		1.06(5)	E2	$22^- \rightarrow 20^-$	6
1029				$24^- \rightarrow 22^-$	6
1141				$26^- \rightarrow 24^-$	6
1233				$28^- \rightarrow 26^-$	6
1325				$30^- \rightarrow 28^-$	6
1341				$32^- \rightarrow 30^-$	6
631				$5^- \rightarrow 6^+$	8→GSB
499	1.25			$7^- \rightarrow 5^-$	5→8

E_γ (keV)	I_γ (%)	R	Multipolarity	$I_i \rightarrow I_f$	Band
1130	1.28			$7^- \rightarrow 6^+$	5→ GSB
400				$7^- \rightarrow 8^+$	5→GSB
556				$7^- \rightarrow 5^-$	5→
1011				$11^- \rightarrow 9^-$	5→GSB
742	1.98	1.17(5)	E2	$13^- \rightarrow 11^-$	5
838	1.48			$15^- \rightarrow 13^-$	5
771				$17^- \rightarrow 15^-$	5
576	1.15			$19^- \rightarrow 17^-$	5
696				$21^- \rightarrow 19^-$	5
837	1.56			$23^- \rightarrow 21^-$	5
968				$25^- \rightarrow 23^-$	5
1085				$27^- \rightarrow 25^-$	5
1187				$29^- \rightarrow 27^-$	5
1258				$31^- \rightarrow 29^-$	5
189	3.86	0.66(6)	M1	$8^- \rightarrow {}^-$	6→5
317	2.13			$9^- \rightarrow 8^-$	5→6
359	3.79			$10^- \rightarrow 9^-$	6→5
383	1.54			$11^- \rightarrow 10^-$	5→6
420	1.05			$12^- \rightarrow 11^-$	6→5
416				$13^- \rightarrow 12^-$	5→6
438	1.3			$14^- \rightarrow 13^-$	6→5
331				$15^- \rightarrow 14^-$	5→6
281	6.4	0.61(1)	M1	$16^- \rightarrow 15^-$	6→5
296	4.26	0.57(1)	M1	$17^- \rightarrow 16^-$	5→6
332			M1	$18^- \rightarrow {}^-$	6→5
364	2.71	0.66(1)	M1	$19^- \rightarrow 18^-$	5→6
403	2.46	0.69(2)	M1	$20^- \rightarrow 19^-$	6→5
434	2.71	0.59(2)	M1	$21^- \rightarrow 20^-$	5→6
470		0.47(21)	M1	$22^- \rightarrow 21^-$	6→5
498				$23^- \rightarrow 22^-$	5→6
531				$24^- \rightarrow 23^-$	6→5
554				$25^- \rightarrow 24^-$	5→6
587				$26^- \rightarrow 25^-$	6→5
600				$27^- \rightarrow 26^-$	5→6
632				$28^- \rightarrow 27^-$	6→5
359	14.03			$7^- \rightarrow 5^-$	8
448	10.38	1.13(1)	E2	$9^- \rightarrow 11^-$	8
559	5.45	1.06(1)	E2	$11^- \rightarrow 13^-$	8
707	5.11			$13^- \rightarrow 15^-$	8
837	5.63	1.07(1)	E2	$15^- \rightarrow 17^-$	8
898	2.48			$17^- \rightarrow 19^-$	8
886	1.5			$19^- \rightarrow 21^-$	8

E_γ (keV)	I_γ (%)	R	Multipolaritiy	$I_i \rightarrow I_f$	Band
942	1.18	0.94(1)	E2	$21^- \rightarrow 23^-$	8
1022	1.07	0.81(4)	M1/E2	$23^- \rightarrow 25^-$	8
1098		1.35(2)	E2	$25^- \rightarrow 27^-$	8
1172				$27^- \rightarrow 29^-$	8
1205				$29^- \rightarrow 31^-$	8
1219				$31^- \rightarrow 33^-$	8
631				$5^- \rightarrow 6^+$	8→GSB
1245				$5^- \rightarrow 4^+$	8→GSB
989				$7^- \rightarrow 6^+$	8→GSB
417	2.06			$7^- \rightarrow 6^+$	8→11
1056				$4^- \rightarrow 6^+$	7→GSB
332	4.3			$8^- \rightarrow 7^-$	7→8
117				$9^- \rightarrow 8^-$	8→7
249				$11^- \rightarrow 10^-$	8→7
363				$12^- \rightarrow 11^-$	7→8
346				$13^- \rightarrow 12^-$	8→7
422				$14^- \rightarrow 13^-$	7→8
413				$15^- \rightarrow 14^-$	8→7
427				$6^- \rightarrow 5^+$	7→GSB
1271				$29^- \rightarrow 27^-$	→8
1049				$21^- \rightarrow 19^-$	→8
734				$17^- \rightarrow 15^-$	8→10
323				$6^- \rightarrow 4^-$	7
264				$8^- \rightarrow 42^-$	7
428	4.81	1.06(2)	E2	$10^- \rightarrow 42^-$	7
612	3.74			$12^- \rightarrow 10^-$	7
769	3.96			$14^- \rightarrow 12^-$	7
895				$16^- \rightarrow 14^-$	7
978	1.16			$18^- \rightarrow 16^-$	7
895				$20^- \rightarrow 18^-$	7
962				$22^- \rightarrow 20^-$	7
1068				$24^+ \rightarrow 22^+$	→GSB
1140				$26^+ \rightarrow 24^+$	→GSB
1196				$28^+ \rightarrow 26^+$	→GSB
1056	2.29			$4^- \rightarrow 6^+$	7→GSB
1350				$4^- \rightarrow 4^+$	7→GSB
483				$6^- \rightarrow 6^+$	7→11
1061				$22^+ \rightarrow 20^+$	→GSB
722				$12^- \rightarrow 10^-$	9→7
699				$14^- \rightarrow 12^-$	9
793				$16^- \rightarrow 14^-$	9

E_γ (keV)	I_γ (%)	R	Multipolarity	$I_i \rightarrow I_f$	Band
824				$18^- \rightarrow 16^-$	9
945				$20^- \rightarrow 18^-$	9
810				$14^- \rightarrow 12^-$	9→7
631				$5^- \rightarrow 6^+$	8→GSB
593	2.43			$8^- \rightarrow 8^+$	7→GSB
708	2.33			$13^- \rightarrow 11^-$	10
783	1.27	1.02(1)	M1	$15^- \rightarrow 13^-$	10
862				$17^- \rightarrow 15^-$	10
991				$19^- \rightarrow 17^-$	10
1015				$21^- \rightarrow 19^-$	10
776				$11^- \rightarrow 9^-$	10→8
465				$11^- \rightarrow 10^-$	10→7
183				$9^- \rightarrow 9^-$	10→8
1001				$15^- \rightarrow 13^-$	10→8
1024				$17^- \rightarrow 15^-$	10→8
488	1.44			$4^+ \rightarrow 2^+$	11
576	3.07			$6^+ \rightarrow 4^+$	11
664	2.73			$8^+ \rightarrow 6^+$	11
738	3.05			$10^+ \rightarrow 8^+$	11
689	1.42			$12^+ \rightarrow 10^+$	11
728	1.56			$14^+ \rightarrow 12^+$	11
771				$16^+ \rightarrow 14^+$	11
853				$18^+ \rightarrow 16^+$	11
925				$20^+ \rightarrow 18^+$	11
980				$22^+ \rightarrow 20^+$	11
1041				$24^+ \rightarrow 22^+$	11
1110				$26^+ \rightarrow 24^+$	11
1185				$28^+ \rightarrow 26^+$	11
835				$2^+ \rightarrow 0^+$	11→GSB
274	1.51	0.51(2)	M1	$15^+ \rightarrow 14^+$	2→1
363				$17^+ \rightarrow 16^+$	1→2
320				$16^+ \rightarrow 15^+$	2→1
396				$18^+ \rightarrow 16^+$	1→2
423		0.57(2)	E2	$19^+ \rightarrow 18^+$	2→1
440			(M1)	$20^+ \rightarrow 19^+$	1→2
459			(M1)	$21^+ \rightarrow 20^+$	2→1
514			(M1)	$22^+ \rightarrow 21^+$	1→2
496			(M1)	$23^+ \rightarrow 22^+$	2→1
506			(E2)	$15^+ \rightarrow 13^+$	2
682			(E2)	$17^+ \rightarrow 15^+$	2
818			(E2)	$19^+ \rightarrow 17^+$	2

E_γ (keV)	I_γ (%)	R	Multipolarity	$I_i \rightarrow I_f$	Band
896			(E2)	$21^+ \rightarrow 19^+$	2
1010			(E2)	$23^+ \rightarrow 21^+$	2
1639		1.12(30)	M1/E2	$14^+ \rightarrow 12^+$	3→GSB
492			(M1)	$16^+ \rightarrow 42^+$	3
624			(M1)	$18^+ \rightarrow 42^+$	3
796			(M1)	$20^+ \rightarrow 42^+$	3
977			(M1)	$22^+ \rightarrow 42^+$	3
1056			(M1)	$24^+ \rightarrow 42^+$	3
238			(M1)	$15^+ \rightarrow 14^+$	4→3
255			(M1)	$16^+ \rightarrow 15^+$	3→4
292	1.3	0.49(2)	M1	$17^+ \rightarrow 16^+$	4→3
332	1.1	0.69(3)	M1	$18^+ \rightarrow 16^+$	3→4
375		0.47(2)	M1	$19^+ \rightarrow 17^+$	4→3
421		0.58(1)	M1	$20^+ \rightarrow 21^+$	3→4
476			(M1)	$21^+ \rightarrow 23^+$	4→3
502			(M1)	$22^+ \rightarrow 21^+$	3→4
547			(E2)	$17^+ \rightarrow 15^+$	4
707			(E2)	$19^+ \rightarrow 17^+$	4
897			(E2)	$21^+ \rightarrow 19^+$	4
1029			(E2)	$23^+ \rightarrow 21^+$	4
1138			(E2)	$25^+ \rightarrow 23^+$	4
1757		1.18(20)	(E2)	$12^+ \rightarrow 10^+$	1→GSB
1139		1.16(10)	(E2)	$14^+ \rightarrow 12^+$	3→GSB

TABLE 6.2: Measured properties of γ ray transitions ^{130}Ce. The intensities (I_γ) are measured relative to 254 keV ($2^+ \rightarrow 0^+$) γ ray. The γ-ray energy accuracy is of $\pm$0.3 keV in energy for strong transitions and $\pm$0.6 keV for weaker transitions. The intensities less than 1% of 254 keV($\equiv$100%) are neglected. The errors on the intensities are %5 of the obtained values for strong transitions and for the weaker transitions to be %10 of the obtained values.

6.3.3 Band 11- the gamma band(+,0)

The gamma band was previously observed and established up to 26^+. However, a new 728 keV transition has been identified in coincidence with the band which based on intensity measurement it is believed to be an in-band transition. The transition is the decay of 12^+ to 10^+ state in the gamma band. A spectrum of the gamma band including the new 728 keV transition is illustrated in Fig 6.5 and 6.6.

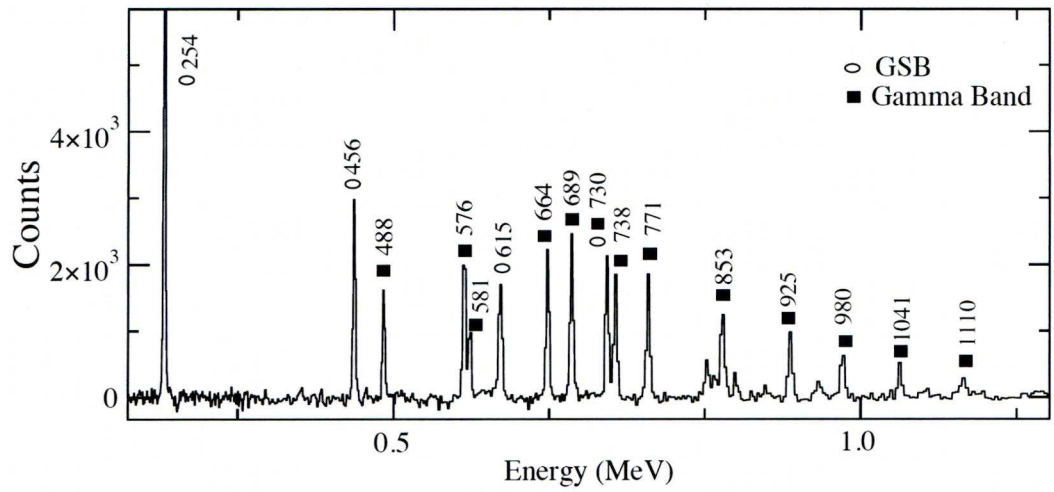

FIGURE 6.5: Sum-of-Triple-gates spectrum, gated on each of the transitions illustrating the band 11(gamma band).

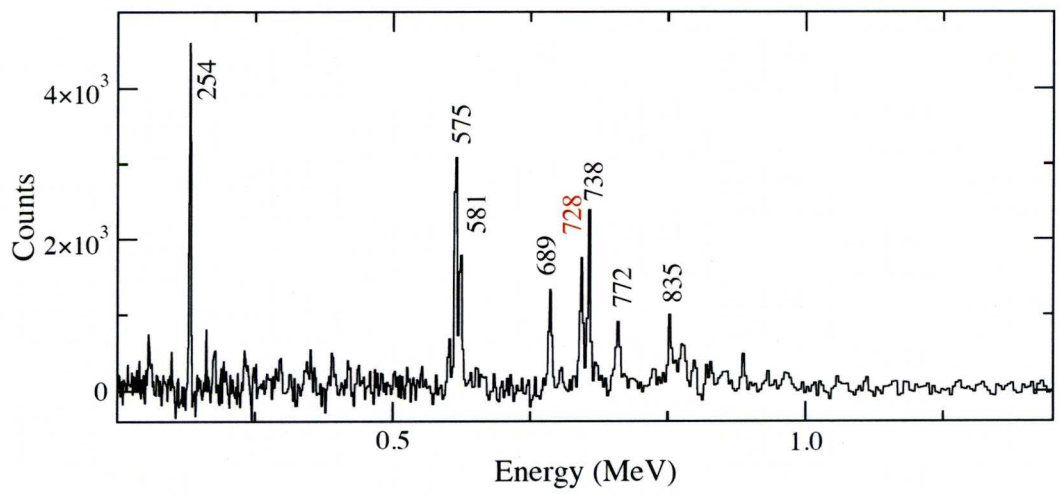

FIGURE 6.6: The double gated spectrum (x = 664 and y = 488) illustrating the new γ ray at energy of 728 keV in the band 11.

6.3.4 Band 10 (-,1)

A new band was observed at low spin decaying to the 7^- state in the band 8. The observation of a 183 keV transition decaying from 9^- to the 9^- in band 8 and 4 more feeding transitions from the band 10 to bands 8 and 7 confirmed the correctness of this new band despite the number of the doublets in bands 7 and 8(631 and 593 keV). The band has been seen up to a 21 $^-$ (23^- tentatively) state. A number of spectra displaying this band are shown in Figures 6.8,6.9,6.10, 6.11. Due to the weak intensity of this band the parity of the band has been assumed as (-) and the in-band transitions have been assumed as stretched electric quadrupole transitions.

6.3.5 Band 9 (-,0)

Another new configuration which was identified through our investigation is feeding to band 7. This structure is populated with extremely low intensity. A 722 keV transition linking the band to band 5 was observed . In addition, 810 keV transition decaying from 14^- in band 9 to 12^- state in band 7 was observed. The band has been extended up to a 20^- (22 $^-$ tentatively) state. Due to the very weak intensity of the structure, the DCO measurement was not feasible and the parity assignment were assumed to be (-). A number of spectra illustrating the new configuration are shown in Fig. 6.3.5, 6.3.5, 6.13, 6.14.

6.4 ΔI=1 bands

6.4.1 Bands 5 and 6 (-,0)

Two coupled bands 5 and 6, were previously established Ref.[46][44] up to 29^- and 30^- respectively. Through the investigation the ordering and the structure of the bands have been confirmed. Moreover, one more dipole (M1/E2) transitions at energy of 587 keV have been observed, decaying from 26^- to 25^- in band 5. In

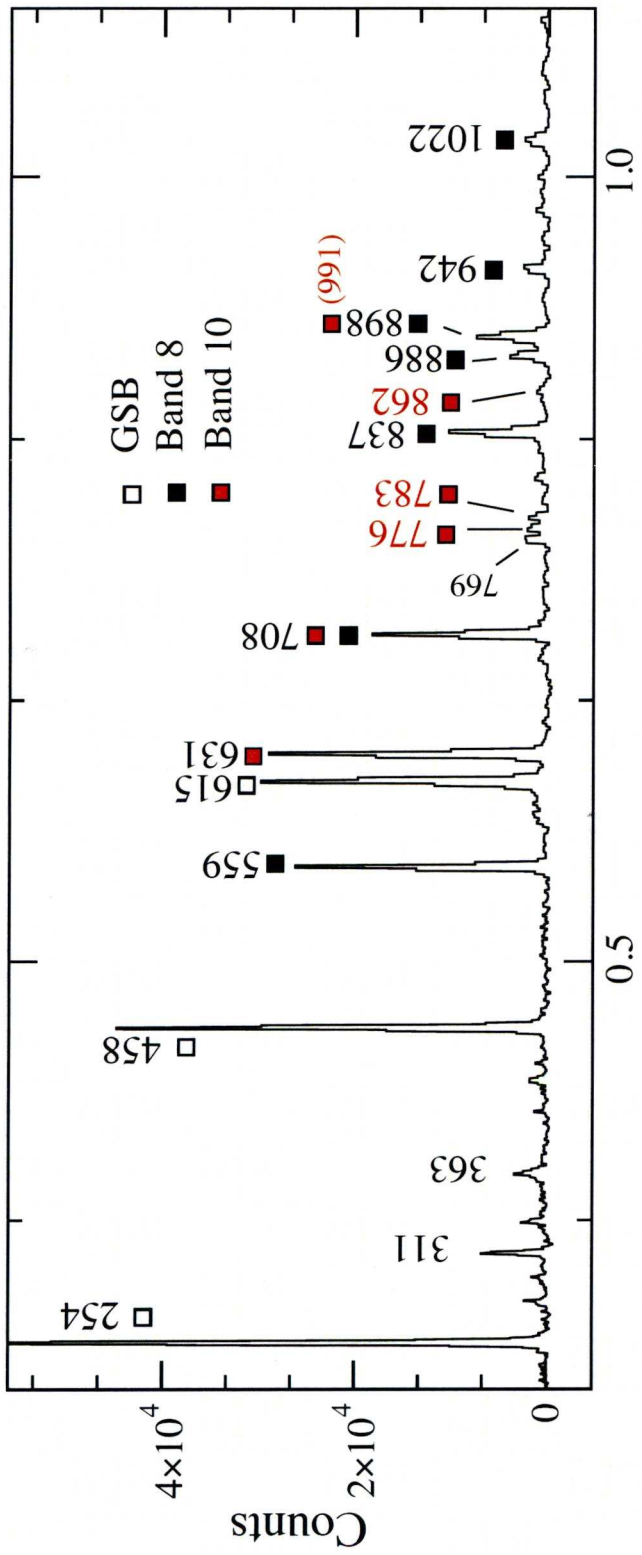

FIGURE 6.7: The double gated spectrum (x = 359 and y = 448) illustrating the newly found band 10.

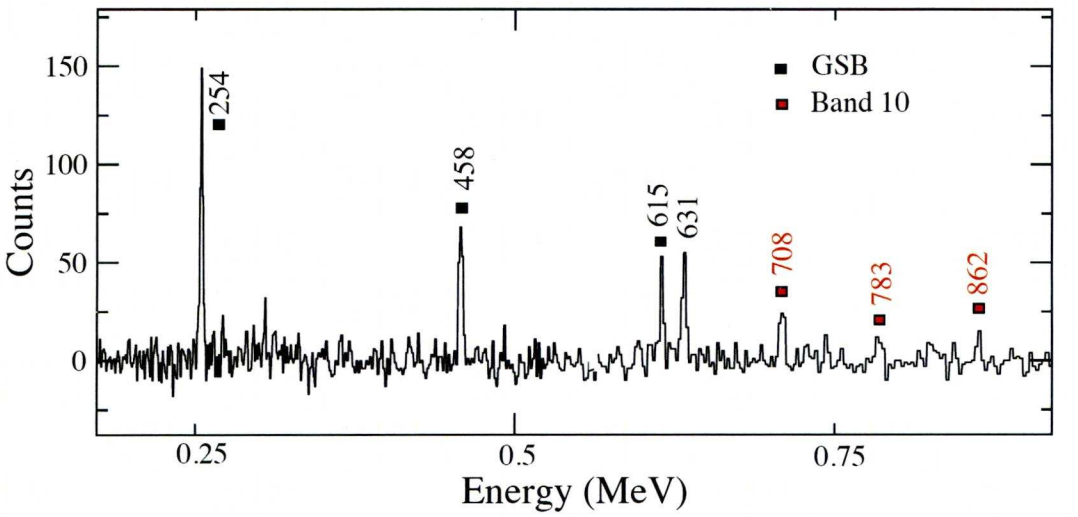

FIGURE 6.8: The triple gated spectrum (x = 448, y = 359 and z = 776) illustrating the newly found band 10.

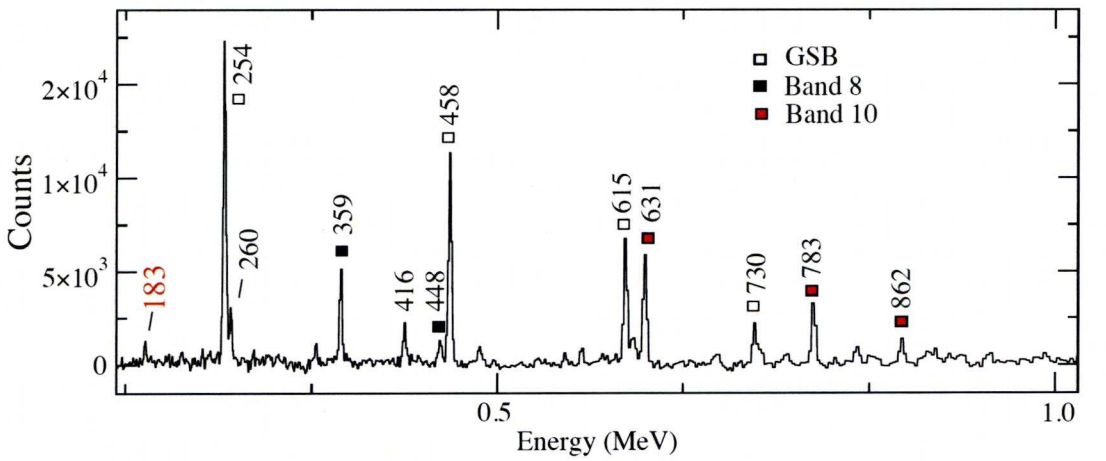

FIGURE 6.9: The double gated spectrum (x = 708 and y = 593)illustrating the new γ rays at in the band 10 including the 183 keV γ ray.

addition, through observation of a new γ-ray of 1258 keV in band 5 and γ-ray at energy of 1341 keV in band 6, the bands have been extended up to 29^- and 32^- state respectively. Spectra illustrating the new transitions in coupled bands of 5 and 6 are shown in Fig.6.18, 6.4.1, 6.4.1.

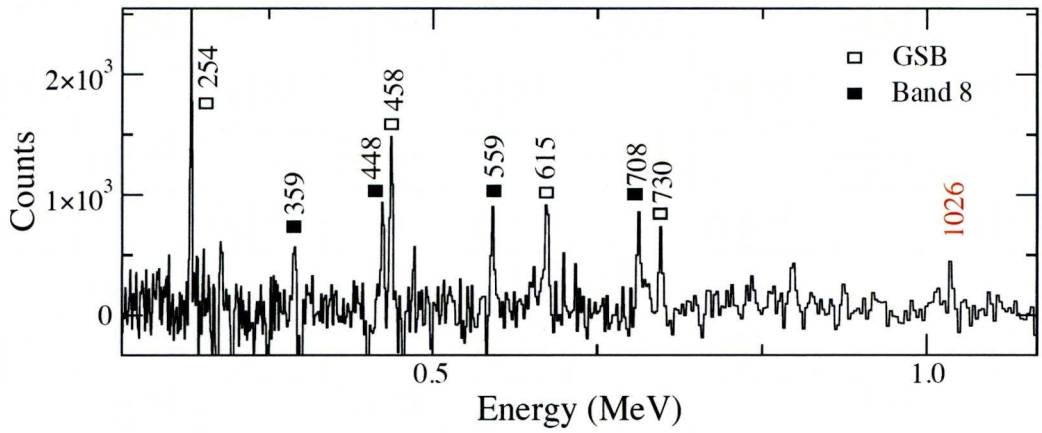

FIGURE 6.10: The double gated spectrum (x = 991 and y = 837)illustrating the new γ ray energy of 1026 keV.

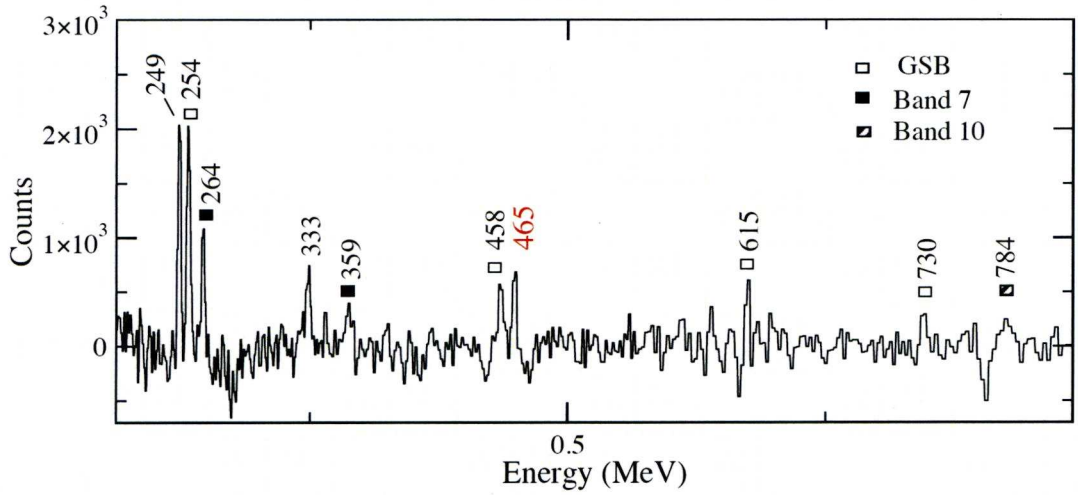

FIGURE 6.11: The double gated spectrum (x = 708 and y = 428)illustrating the new γ rays at energy of 465 kev.

6.4.2 Bands 7 and 8 (-,0)

Band 8 was previously reported Ref.([46][44]) and established up to a 27^- state. Through the investigation the ordering and structure of the band were confirmed and in addition, new gamma rays at energies of 1205 and 1219 keV have been identified(shown in Fig.6.4.2)) which extended the band to $31\hbar$.

Band 7 has been extended down from previously reported 6^- state Ref([46][44]) to 4 state with the addition of quadruple transition of 323 keV. This 4^- state

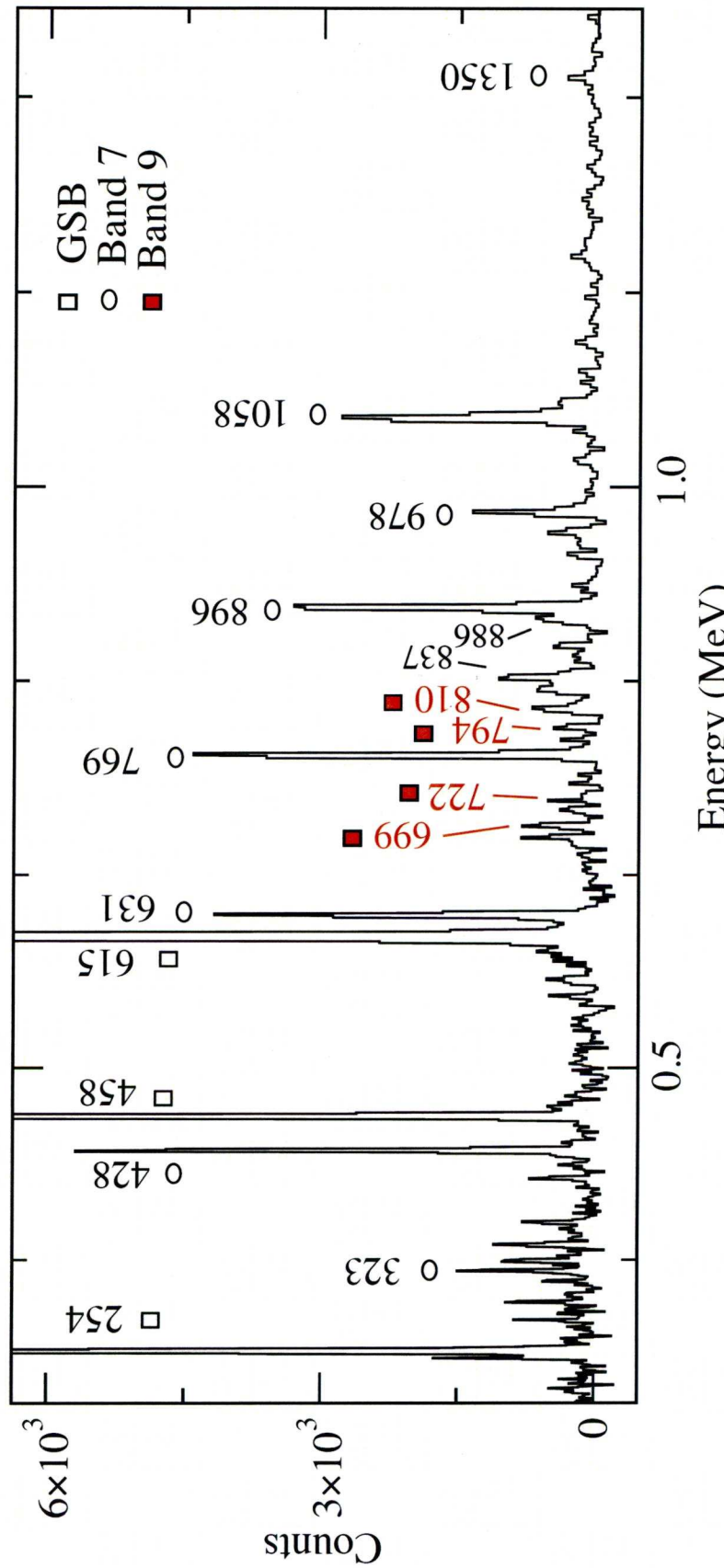

FIGURE 6.12: The double gated spectrum (x = 264 and y = 428)illustrating the newly found γ rays in the band 9.

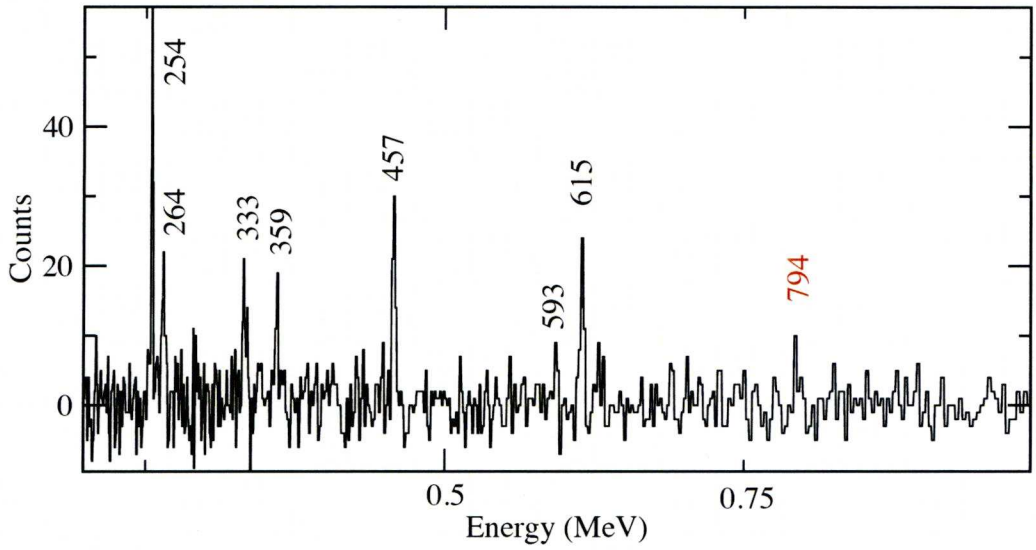

FIGURE 6.13: The triple gated spectrum (x = 699, y = 722 and z = 428)illustrating the newly found γ rays in the band 9.

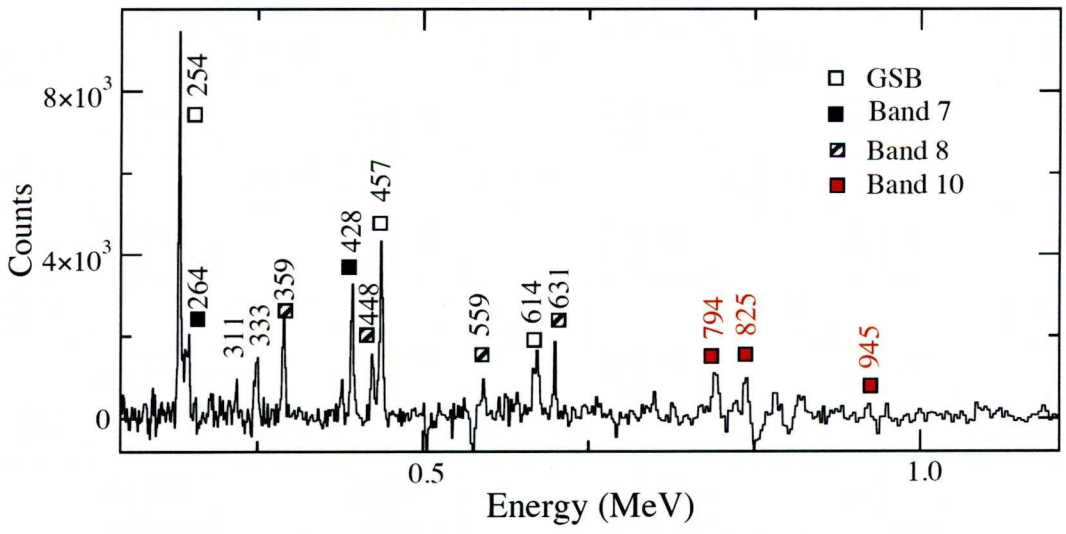

FIGURE 6.14: The double gated spectrum (x = 810 and y = 612)illustrating the newly found γ rays in the band 9.

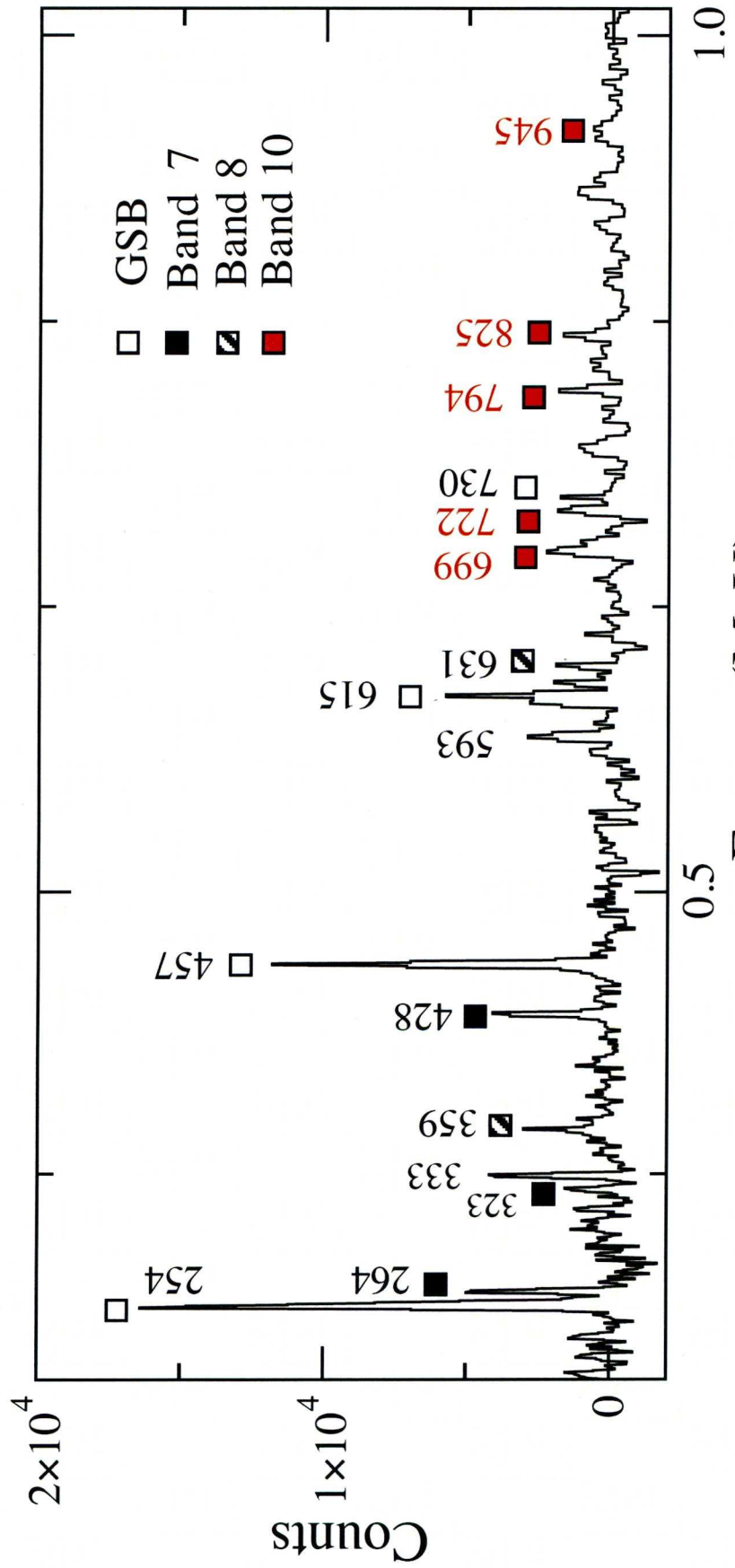

FIGURE 6.15: Sum-of-Triple-gated spectra, gated on each of the transitions in band 9 illustrating the newly found γ rays in the band 9.

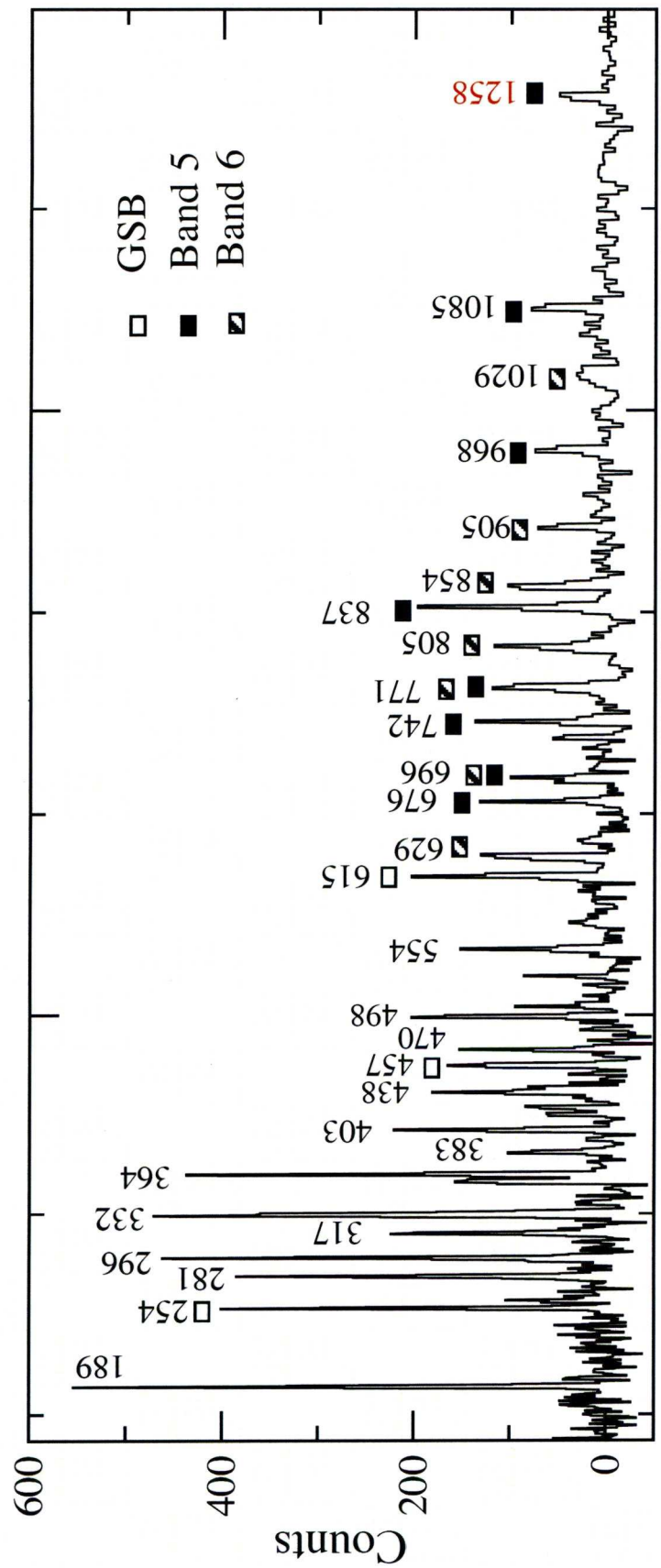

FIGURE 6.16: The triple gated spectrum (x ,y = list of γs in band 5 and z = 1187) illustrating the newly found γ ray at energy of 1258 keV in band 5.

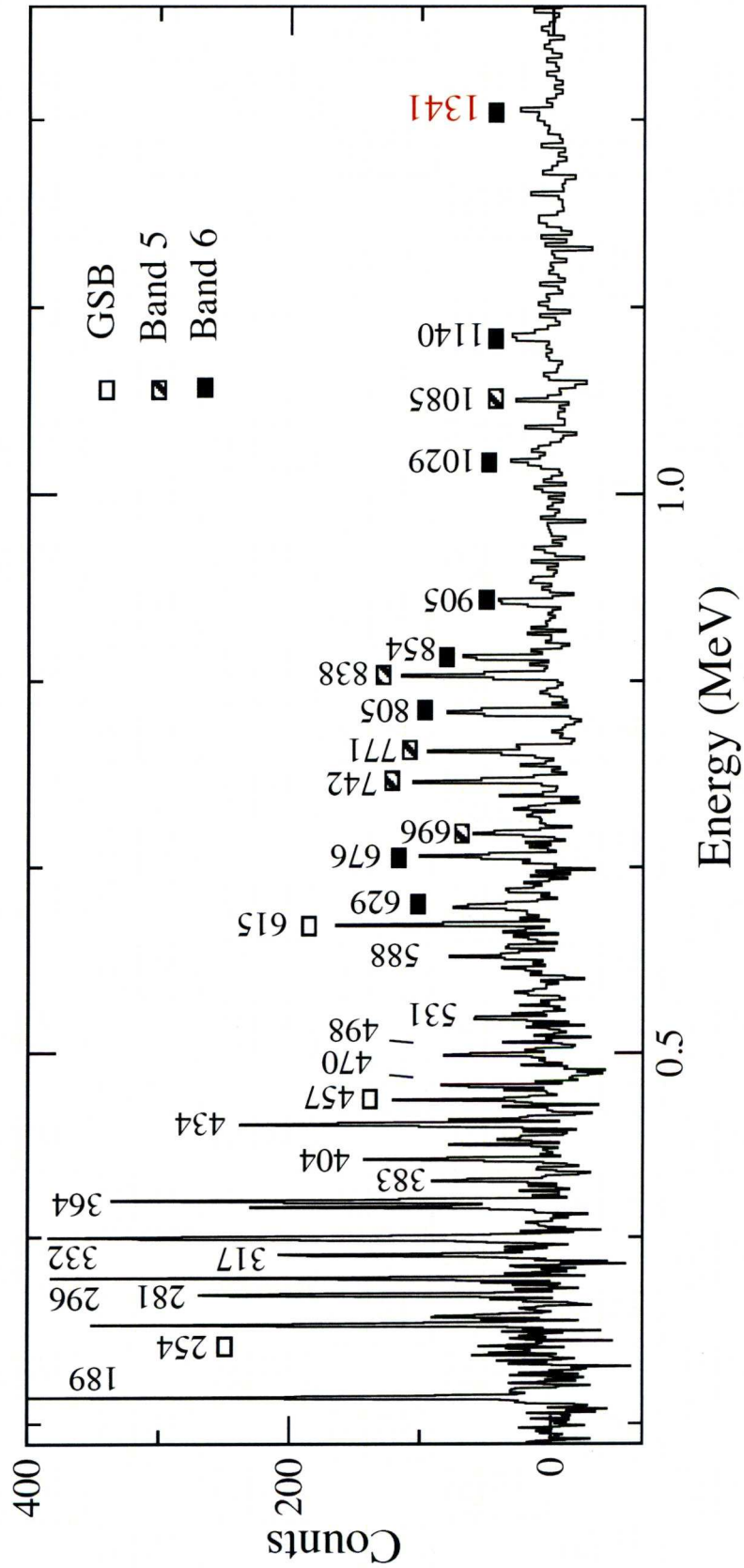

FIGURE 6.17: The triple gated spectrum (x ,y = list of γs in bands 5 and 6 and z = 1232) illustrating the newly found γ ray at energy of 1341 keV in band 6.

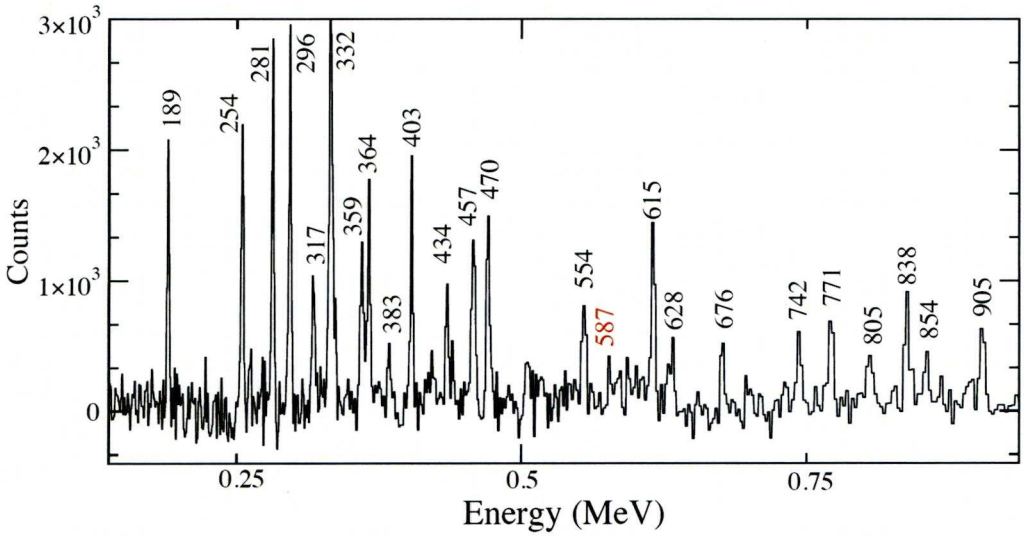

FIGURE 6.18: The triple gated spectrum (x =531 and y = 498) illustrating the newly found γ rays at energy of 587 keV in band 5.

decays to 2^+) state in GSB via a 1350 keV transition. Moreover, 4 new in-band transitions at energy of 962, 1098, 1140 and 1196 keV have been identified and consequently extended the band 7 to a 28^- state. A spectrum illustrating the new γ-rays is shown in Fig.6.22.

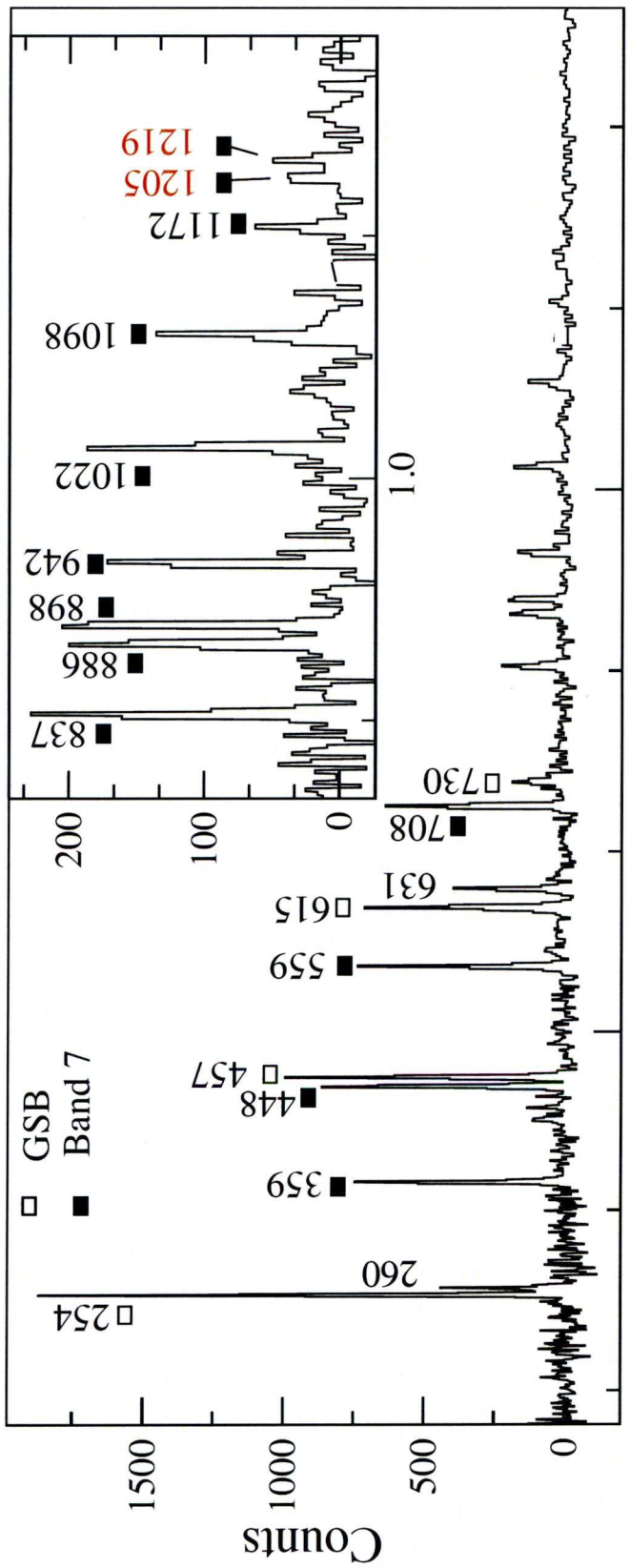

FIGURE 6.19: Sum-of-Triple-gated spectrum, gated on transitions each of the transitions in band 8 illustrating the newly found γ rays at energy of 1205 and 1219 keV in band 8.

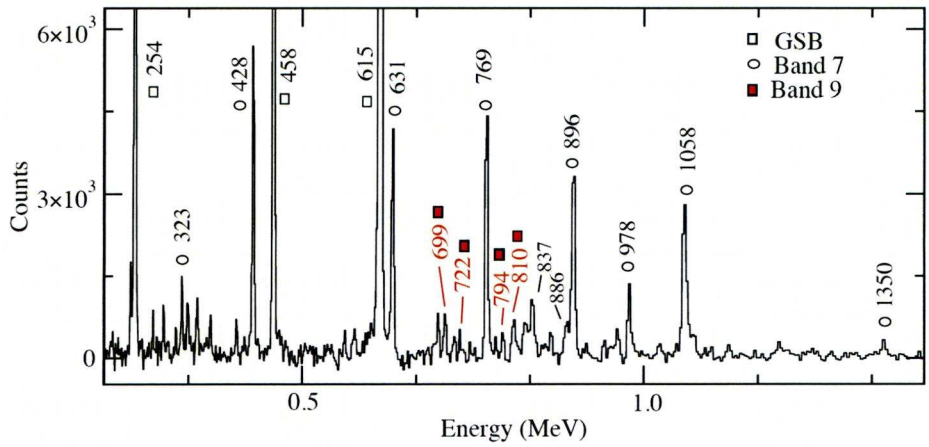

FIGURE 6.20: The triple gated spectrum (x = 264 and y = 428) illustrating the newly found γ rays at energy of 323 and 1350 keV in band 7.

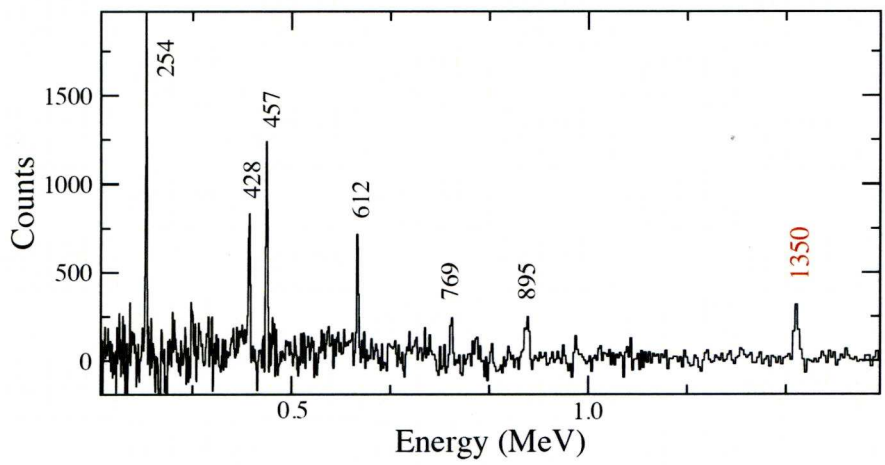

FIGURE 6.21: The double gated spectrum (x = 323 and y = 264) illustrating the newly found γ ray at energy of 1350.

6.4.3 Bands 1 and 2 (+,0)

New relatively high spin coupled configurations have been observed in this work (band 1 and 2 Fig [6.23]).Three linking transitions of 1139, 1520 and 1757 keV decaying from the band 1 to the GSB have been found which confirm the position of the structures (bands 1 and 2). Through DCO ratio measurement the quadrupole character of the transitions have been investigated. However, due to the large errors associated with the values (1757:R=1.18(20), 1139:R=1.16(10))

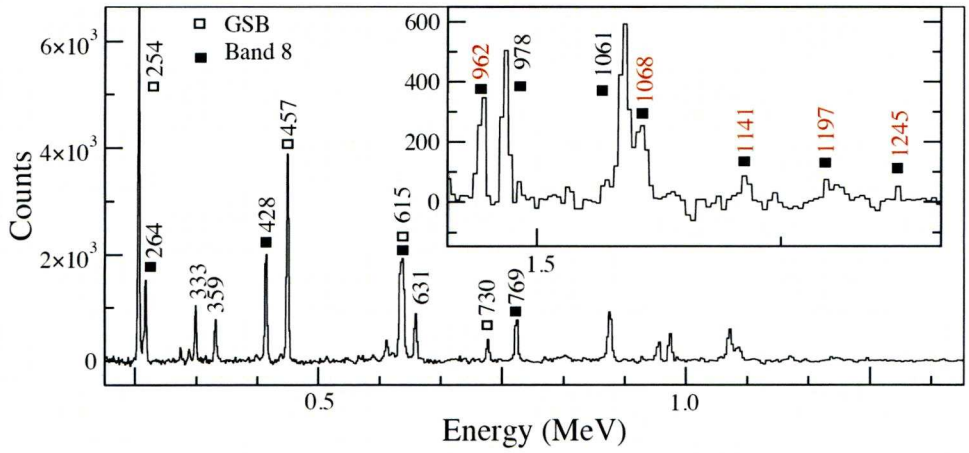

FIGURE 6.22: Sum-of-Triple-gates spectrum, gated on each of the transitions in band 7(below $20\hbar$) illustrating the newly found γ rays at energy of 962,1068,1140 and 1196 keV in band 7.

the quadrupole character of the linking transitions is inconclusive. Band 1 and 2 have been seen to the 26^+ and 25^+ states respectively. The band head of the bands 1 and 2 have assigned as 12 and $13\hbar$ respectively. Two spectra containing the newly found γ-rays of the bands 1 and 2 are shown in Fig.[6.23].

6.4.4 Bands 3 and 4 (+,0)

Similar to the previous section, two more new coupled bands(4 in total) have been observed in this work. One linking transition at an energy of 1639 keV, a decay to a 12^+ in the GSB has been identified and confirmed the position of the bands. The measured properties of the 1639 keV γ-ray again led to an inconclusive quarople charter of the transition, due to large error associated with the DCO ratio value. The band heads of the bands 3 and 4 are assigned as 14^+ and 15^+ and the bands have been extended up to 24^+ and 25^+ state respectively. Spectra shown in Fig. [6.23] illustrate these γ-rays.

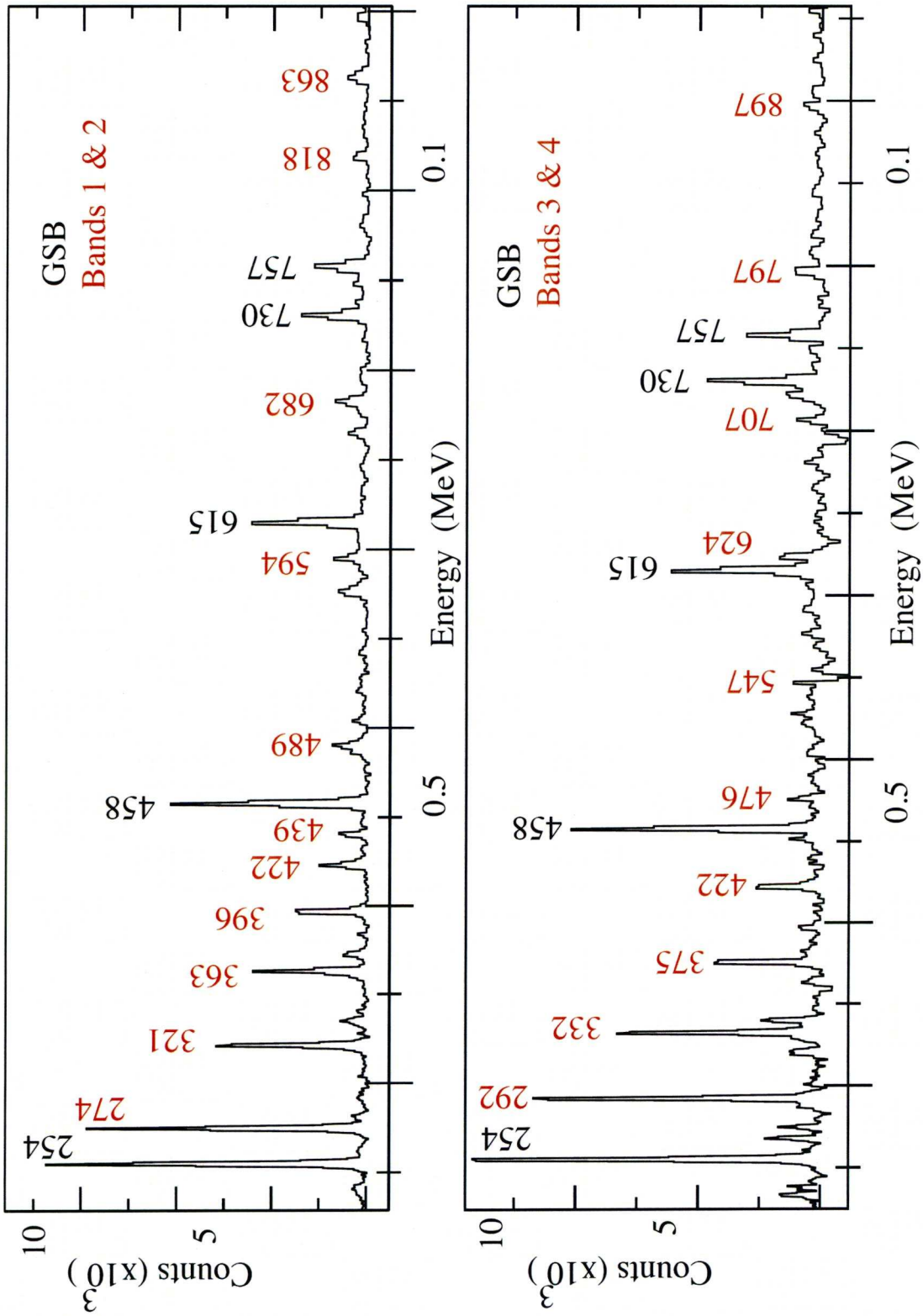

FIGURE 6.23: The double gated spectrum (x = 323 and y = 264) illustrating the newly found γ rays belonging to four four-quasiparticle configurations 1 and 2 (top panel) and 3 and 4 (bottom panel).

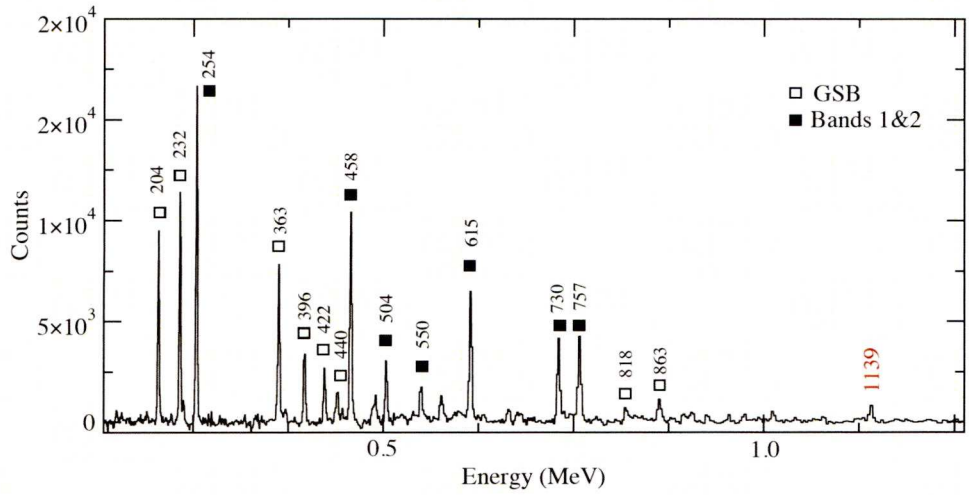

FIGURE 6.24: The double gated spectrum (x = 320 and y = 274) illustrating the newly found linking transition from band 1 to the GSB.

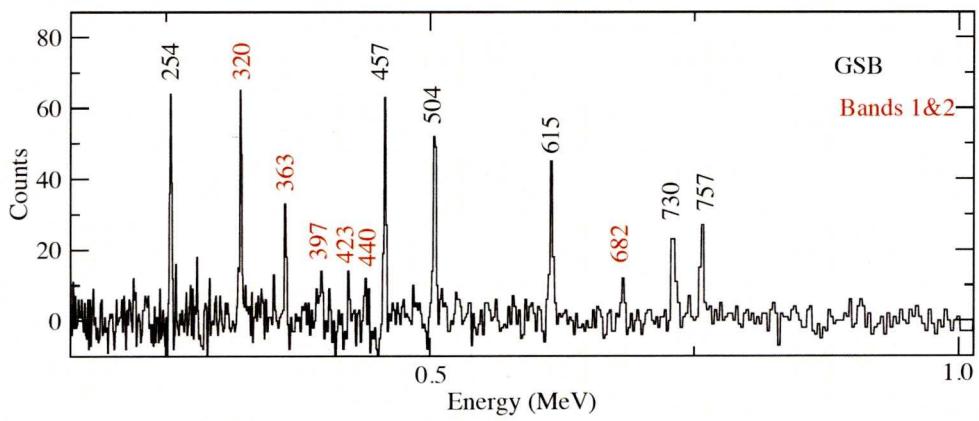

FIGURE 6.25: The double gated spectrum (x = 274 and y=1139).

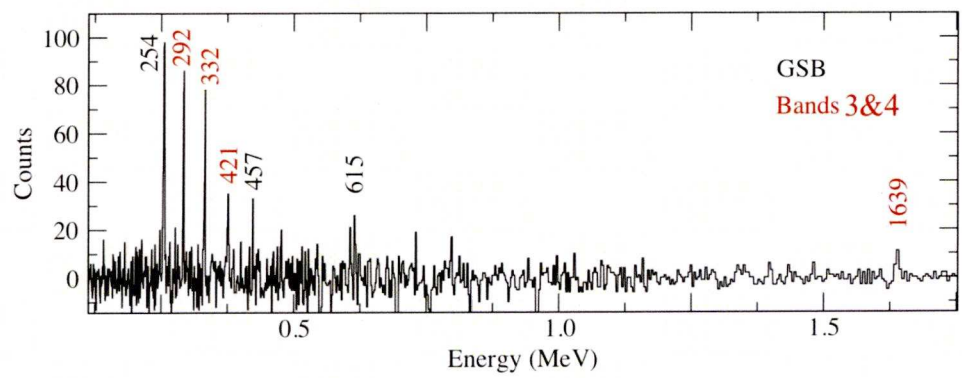

FIGURE 6.26: The triple gated spectrum (x = 255, y = 238 and z= 292) illustrating the newly found linking transition from band 3 to the GSB.

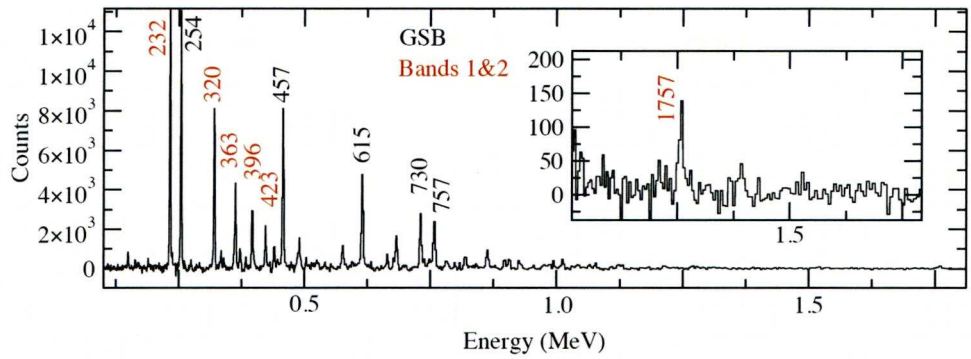

FIGURE 6.27: The double gated spectrum (x = 274 and y = 204) illustrating the newly found linking transition from band 1 to the GSB.

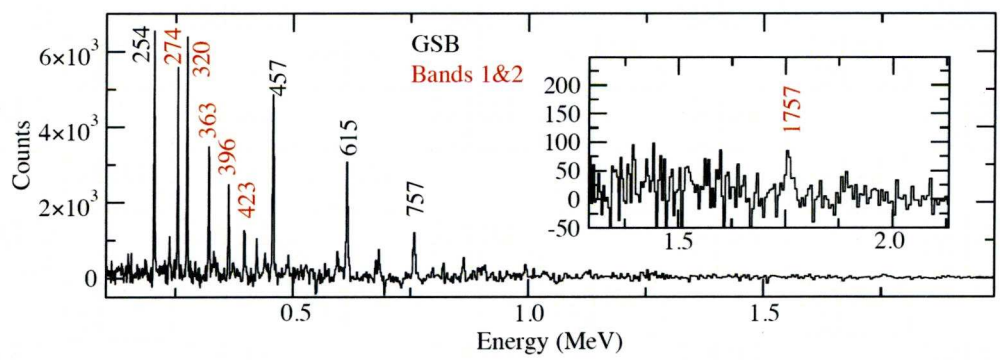

FIGURE 6.28: The double gated spectrum (x = 232 and y = 204) illustrating the newly found linking transition from band 1 to the GSB.

Chapter 7

Discussion of ^{130}Ce Results

7.1 Introduction

The question of how the properties of nuclei evolve with increasing excitation energy and angular momentum is one of the current frontiers in nuclear physics. To investigate this, light rare-earth nuclei with mass A ~130 have been studied. The nucleus $^{130}_{58}Ce_{72}$ lies in a well-known region of nuclei which show a soft potential-energy surface with respect to γ, the triaxiality coordinate description of rotating quadrupole shapes [42]. In this region the overall shape of nuclei is regulated by the various occupied quasiparticle orbitals at the nuclear Fermi surface which are able to polarise the γ-soft core[42].

Through quadruples analysis (γ^4) of the data several bands have been identified for the first time and the previously reported structures [44–46] have been extended to high spin. This chapter is devoted to the interpretation of the results gained during this investigation along with results from previous attempts [44–46]. In order to discuss and compare the results with theoretical calculations the experimental data are presented in terms of alignment i_x and routhian e' plots as function of rotational frequency

$$\omega = \frac{E_\gamma}{2\hbar} \tag{7.1}$$

In each case, a reference based on a configuration with variable moment of inertia

$$\Im_{ref} = \Im_0 + \omega^2 \Im_1 \tag{7.2}$$

, has been subtracted where the Harris parameters of Ref. [39] of $\Im_0$= 17 MeV^{-1} $\hbar^2$ and $\Im_1$= 25.8 MeV^{-3} $\hbar^4$; derived from the S band of $^{130}_{58}Ce_{72}$ over the spin range 16 $\leq$I$\leq$ 24 were used as reference.

A Woods-Saxon cranked shell model calculation has been performed and where possible it was compared to the experimental data. However, in some cases due to a number of reasons (such as poor intensity population of the bands or lack of theortical reproduction of the data) the configurations assignments have been performed tentativley and inconclusively. In addition, in order to strengthen the configuration assignments; for both the previously reported and the new configurations the B(M1)/B(E2) ratios of reduced transition probabilities have been measured directly from the experimental results and compared with geometrical model (the semi classical model of Dönau and Fraeundorf [48, 49]). In the Woods-Saxon calculation, the triaxial Woods-Saxon potential was used and the pairing which is calculated at zero frequency has fallen to 50% of initial value at $\omega \cong 0.70$ MeV/$\hbar$.

Table 7.1 and Table 7.2 illustrate the labelling of the quasiparticle orbitals in the CSM calculation and the quasiparticle configurations assigned to the bands in $^{130}_{58}Ce_{72}$ along with experimental and predicted alignments (i_x) and crossing frequencies.

7.2 ΔI=2 bands

This section is devoted to discuss and interpert the possible configurations assigments for ΔI=2 structures.

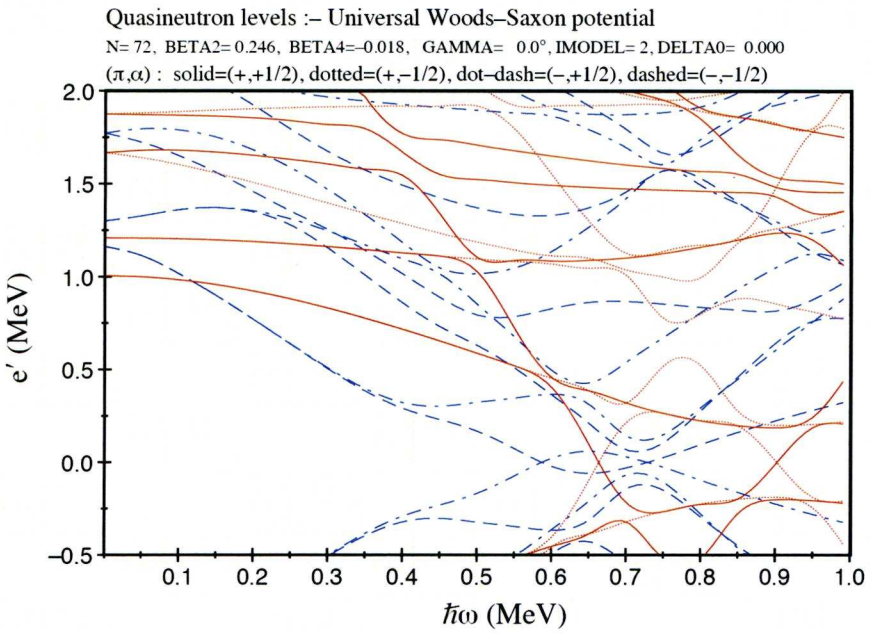

FIGURE 7.1: Single-particle neutron calculation using deformation using deformation parameters relevant (γ=0,β_2=0.246)

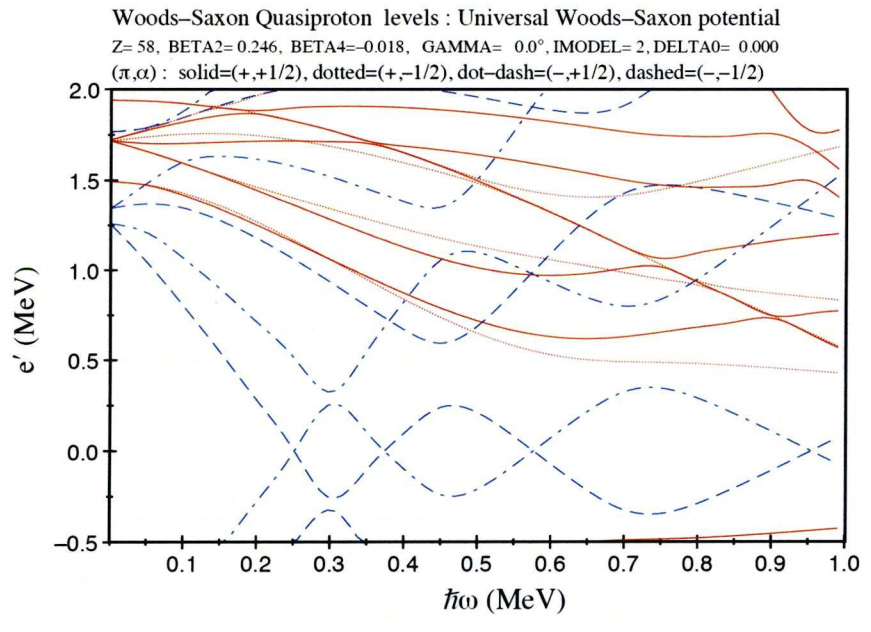

FIGURE 7.2: Single-particle proton calculation using deformation using deformation parameters (γ=0,β_2=0.246)

Protons			Neutrons		
Label	Nilsson State	(π,α)	Label	Nilsson State	(π,α)
E	$h_{11/2}$[541]3/2	(-,+1/2)	e	$h_{11/2}$[514]9/2	(-,+1/2)
F	$h_{11/2}$[541]3/2	(-,-1/2)	f	$h_{11/2}$[514]9/2	(-,-1/2)
G	$h_{11/2}$[550]1/2	(-,+1/2)	g	$h_{11/2}$[523]7/2	(-,+1/2)
H	$h_{11/2}$[550]1/2	(-,-1/2)	h	$h_{11/2}$[523]7/2	(-,-1/2)
A	$d_{5/2}$[422]3/2	(+,+1/2)	a	$g_{7/2}$[402]5/2	(+,+1/2)
B	$d_{5/2}$[422]3/2	(+,-1/2)	b	$g_{7/2}$[402]5/2	(+,-1/2)

TABLE 7.1: Quasiparticle labels regarding to ^{130}Ce including the dominant Nilsson components and their parity and signature, (π,α).

	Experiment			CSM	
Band	i_x	ω_c	Quasiparticle configuration	i_x	ω_c
GSB	8.5	0.32	vac→EF	9.0	0.3
GSB(S)	5.2	0.65	EF→efEF	5.4	-
Band 1	7	-	EB ⊗ ea	11.3	-
Band 2	7.2	-	EB ⊗ eb	11.3	-
Band 3	9	-	EA ⊗ ea	11.5	-
Band 4	9	-	EA ⊗ eb	11.5	-
Band 5	8.1	0.31	eb→EFeb	8	0.3
Band 6	8.1	0.31	ea→EFea	8	0.3
Band 7	5	0.45	EA→FGEA	7.05	0.45
Band 8	5	0.45	EB→FGEB	7.24	0.45

TABLE 7.2: Quasiparticle configuration regarding to ^{130}Ce including the experimental and theoretical crossing frequency in each.

7.2.1 Ground state band GSB

The GSB in this nucleus has been previously reported and established in Ref [44–46].

Fig 7.3 and Fig 7.4 show plots of the experimental alignment i_x and the routhian e' of the quasiparticles as a function of rotational frequency.

The GSB which is the yrast (0,+) sequence starts off from the quasiparticle vacuum (or 0 qp) state at low spin and exhibits collective rotational motion of such a deformed nucleus. It is followed by first alignment of a pair of $h_{11/2}$ protons (EF) at $\hbar\omega = 0.32$ MeV, the crossing of the two-quasiproton configuration, EF with the GSB leading to the observation of backbend as it is shown in Fig 7.3 . Through

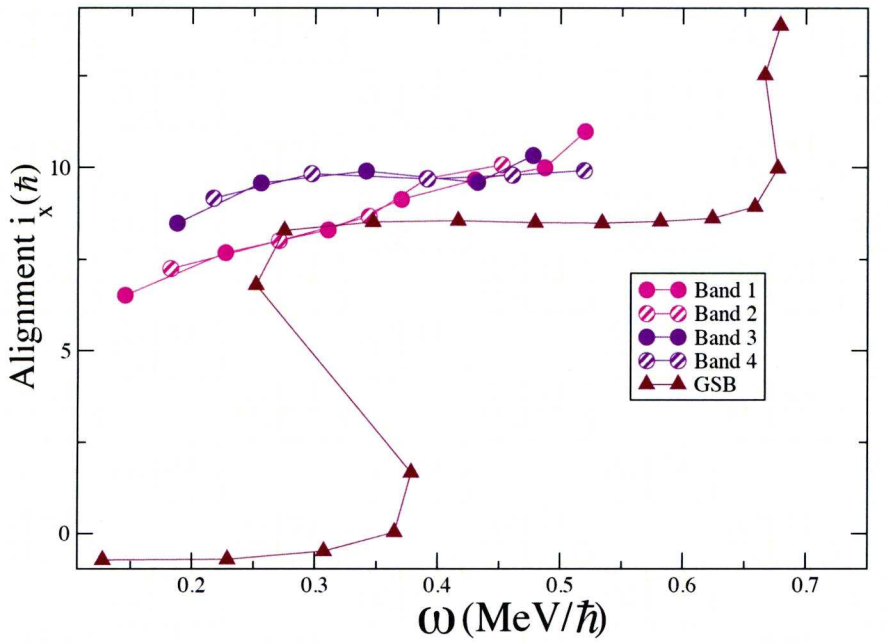

FIGURE 7.3: Experimental alignment, i versus rotational frequencyω for the positive parity bands in ^{130}Ce. The Harris parameters of $\Im_0$= 17 MeV^{-1} $\hbar^2$ and $\Im_1$= 25.8 MeV^{-3} $\hbar^4$ have been used.

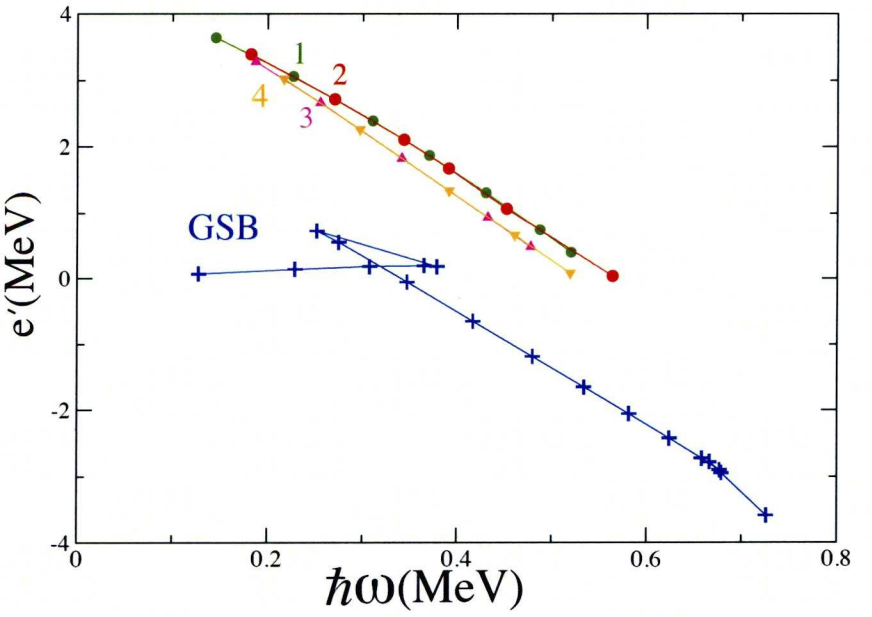

FIGURE 7.4: Experimental routhian, e' versus rotational frequency ω for the positive parity bands in ^{130}Ce. The Harris parameters of $\Im_0$= 17 MeV^{-1} $\hbar^2$ and $\Im_1$= 25.8 MeV^{-3} $\hbar^4$ have been used.

this alignment the S-band carries an alignment of 8.5 $\hbar$ which is consistent with the theoretical prediction(i.e. the slopes of the crossing orbitals in the CSM plots Fig7.2). A second backbend has been identified in this work which can be assigned as the alignment of the first pair of quasineutrons (ef) at $\hbar\omega$ =0.65 MeV. The band gains 5.2 $\hbar$ alignment through this crossing. The four-quasiparticle configuration of the ground state band after these crossing can be the assigned as : $(\pi_{h_{11/2}})^2(\nu_{h_{11/2}})^2$.

7.2.2 The Band 11- the Gamma Band

It is the lowest energy extracted band observed in this nucleus and was previously reported as a gamma-vibrational band by [44–46]. The newly found γ-ray increments the states of the band by another 2 $\hbar$.

7.2.3 The Band 9 and 10

Two new extremely weakly populated bands have been observed for the first time, however no interpretation or configuration can be assigned for the bands. Further data are required in order to assign any configuration.

7.3 ΔI=1 bands

This section is devoted to discuss and interpert the possible configurations assigments for ΔI =1 structures. The previously reported configurations along with the new bands will be discussed. In some cases the disagreement with previous reports will be underlined too.

7.3.1 The Bands 5 and 6

Two strongly coupled bands (5 and 6) have been previously identified and reported [44–46]. As it can be seen from Fig 7.5 and Fig 7.6 no signature splitting can be

seen. The configurations for bands 5 and 6 are based on the nearest neutron orbits to the Fermi surface eb and ea respectively. The Deformation Aligned (DAL) bands 5 and 6 have been assumed to have K=7 [44–46] which is consistent with the assignment ($h_{11/2}$[514]9/2, $g_{7/2}$[402]5/2). The first alignment of a pair of $h_{11/2}$ protons (EF) at $\hbar\omega$ = 0.31 MeV, the crossing of the two-quasiproton configurations EF with bands 5 and 6 (7.6) leads to the observation of backbends (Fig 7.5). Through this alignment the bands carry an alignment of 8.1 $\hbar$. The bands remain almost flat in alignment after the first crossing.

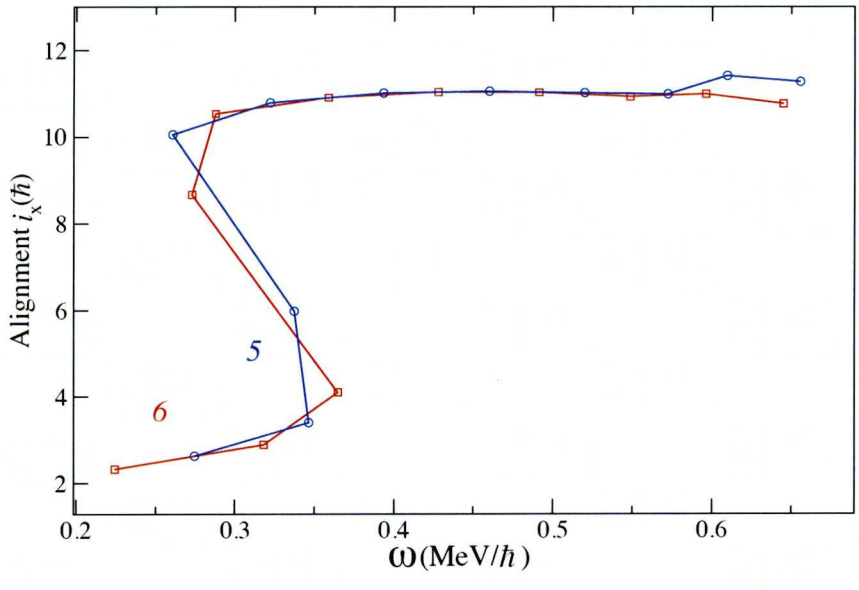

FIGURE 7.5: Experimental alignment, i versus rotational frequencyω for the bands 5 and 6 in ^{130}Ce. The Harris parameters of $\Im_0$= 17 MeV^{-1} $\hbar^2$ and $\Im_1$= 25.8 MeV^{-3} $\hbar^4$ have been used.

7.3.2 The Bands 7 and 8

The bands 7 and 8 have been previously identified by D. M.Todd et al.[46] and later developed by E.S .Paul et al [45] up to the 22 $^-$ and 29 $^-$ states respectively. Through this investigation band 7 was extended up to 28$^-$ state and also it's band head were extended down from 6 $^-$ to a 4 $^-$ state. Bands 7 and 8 are assigned as the two-quasiproton configurations of EA and EB respectively. As it can be seen from Fig 7.7 at lower frequency ($\hbar\omega \leq$ 0.3 MeV) bands exhibits a reduction

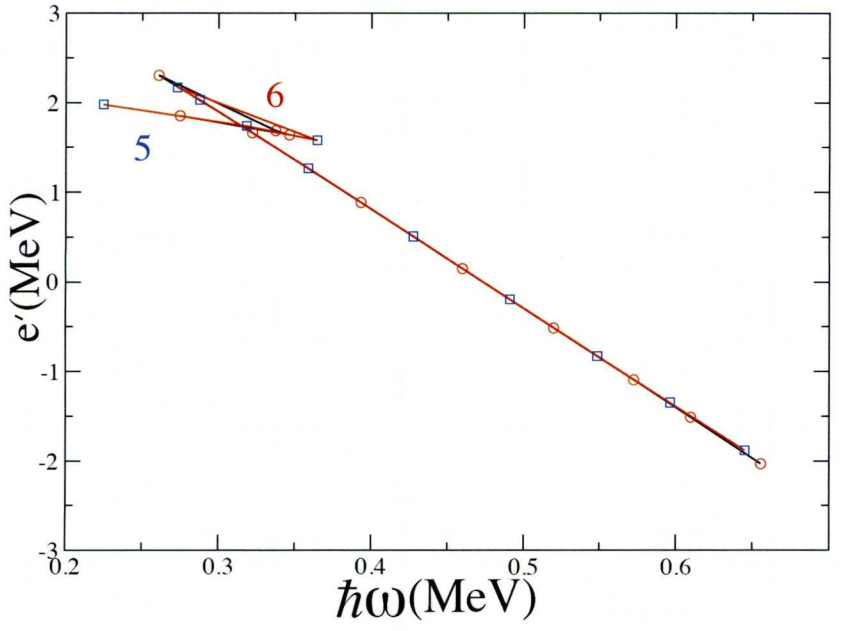

FIGURE 7.6: Experimental routhian, e' versus rotational frequency ω for the bands 5 and 6 in ^{130}Ce. See Fig7.5 for Harris parameters.

in alignment (down slope) whilst in this frequency range there is an increasing signature splitting. Previous attempts to interpret these features ([46]) have come up with possibility of a mixture of the odd spin sequence (band 8) with an unseen octupole band. As can be seen from the Fig 7.8 the signature splitting of the bands tends to reduce until the occurance of first backbend. The alignment occurs at 0.45 MeV frequency and through this alignment the bands carry an alignment of 5 $\hbar$. There are two possibilities for the nature of this alignment; the crossing of two-quasiprotons of $\pi[h_{11/2}[541]3/2 \otimes h_{11/2}\ [550]1/2]$ (FG) or crossing of two-quasineutron of $\nu[h_{11/2}[514]9/2]^2$ (ef) with the bands. However, as the former crossing possibility (FG) has not been seen in GSB and the alignment is shown in Fig 7.7 illustrates a relatively sharp and upbend type of crossing, it has been assigned for the alignment. Therefore the configuration of π[EA]$\otimes$ π [FG] and π[EB] $\otimes\pi$[FG] have been assigned for bands 7 and 8 respectivly. As shown in Fig 7.7 just after $\hbar\omega$=0.5 MeV frequency the bands start to manifest the second alignment. This alignment could be crossing of two-quasineutrons (ef) as a similar crossing has been seen in the GSB. However further experimental data are needed to confirm this.

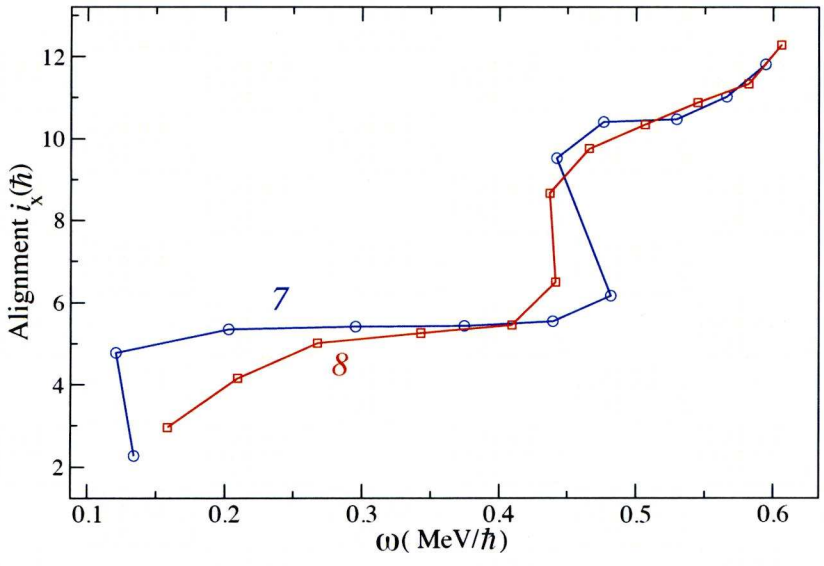

FIGURE 7.7: Experimental alignment, i versus rotational frequencyω for the bands 7 and 8 in ^{130}Ce. The Harris parameters of $\Im_0$= 17 Mev^{-1} $\hbar^2$ and $\Im_1$= 25.8 Mev^{-3} $\hbar^4$ have been used.

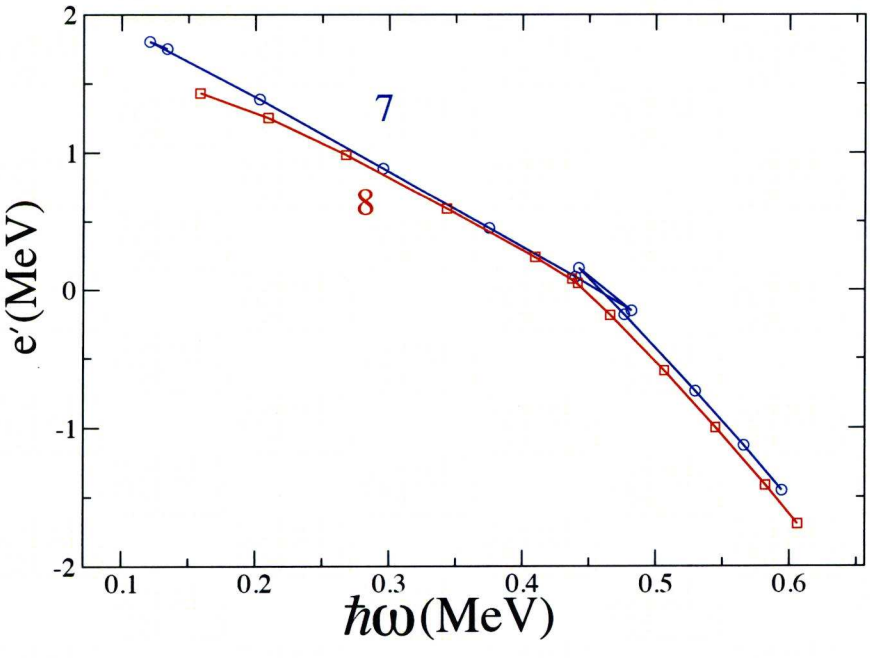

FIGURE 7.8: Experimental routhian, e' versus rotational frequency ω for the bands 7 and 8 in ^{130}Ce. See Fig7.7 for Harris parameters

7.3.3 The Bands 1 and 2

In this investigation two strongly coupled relatively high spin bands have been observed which feed the 10^+ and 14^+ states in the GSB. The bands exhibit relatively weak E2 in-band and very strong M1/E2 cross over transitions. As it can be seen from the Fig 7.9 and Fig 7.10 no sign of backbending is evident and the bands illustrate a downsloping alignment at lower frequencies ($\hbar\omega \leq$ 0.3 MeV). The bands 1 and 2 have initial alignment of $\approx$ 7 $\hbar$ which is equal to sum of initial alignment of band 8 (about 5 $\hbar$) by initial alignment of band 6 ($\approx$ 2 $\hbar$). Thus the band have been assigned as two four-quasiparticle configurations. The bands can be based on the four-quasiparticle configuration of π[EB] $\otimes$ ν[ea] and π[EB] $\otimes$ ν[eb]. This configuration assignments have been confirmed through M1/E2 ratio measurement which will be dealt in next section.

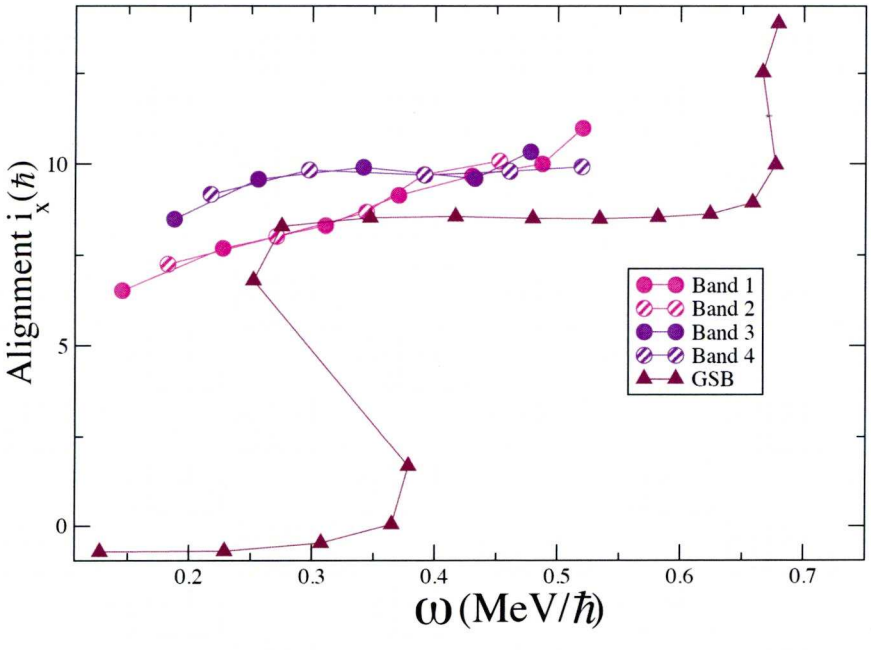

FIGURE 7.9: Experimental alignment, i versus rotational frequencyω for the positive parity bands in ^{130}Ce. The Harris parameters of $\Im_0$= 17 Mev^{-1} $\hbar^2$ and $\Im_1$= 25.8 Mev^{-3} $\hbar^4$ have been used.

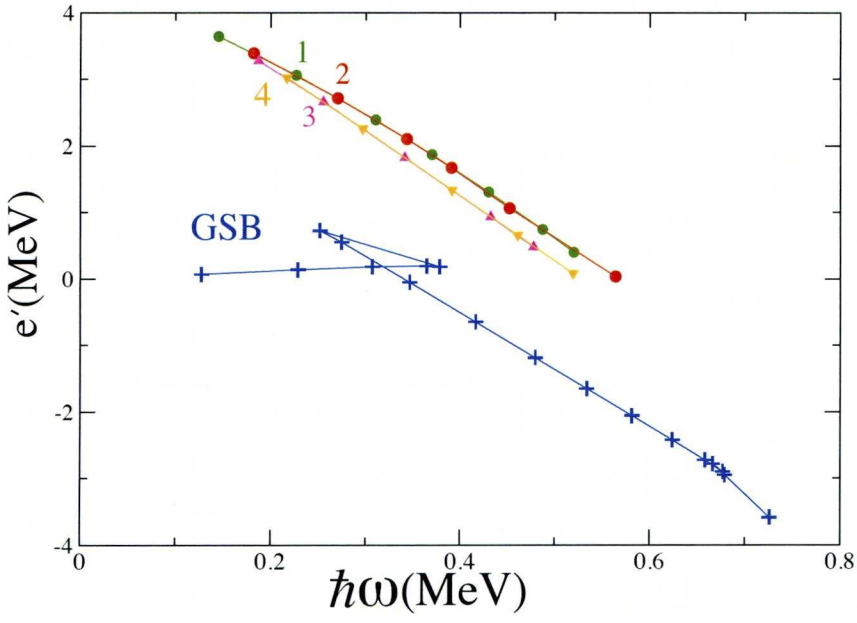

FIGURE 7.10: Experimental routhian, e' versus rotational frequency ω for the positive parity bands in ^{130}Ce. The Harris parameters of $\Im_0$= 17 MeV^{-1} $\hbar^2$ and $\Im_1$= 25.8 MeV^{-3} $\hbar^4$ have been used.

7.3.4 The Bands 3 and 4

Similar to bands 1 and 2, two more (four in total) relatively high spin strongly coupled bands have been identified for the first time. The bands again have been assigned as two, four-quasiparticle configurations as the initial alignment of bands 3 and 4 ($\approx$ 9 $\hbar$ is $\approx$ sum of initial alignment of band 7($\approx$5 $\hbar$) and 5 ($\approx$ 3 $\hbar$). As can be seen from the Fig 7.9 and Fig 7.4 the bands do not show any sign of backbend and remain almost flat in the alignment diagram. The assigned configuration for the bands 3 and 4 are; π[EA] $\otimes$ ν[ea] and π[EA] $\otimes$ ν[eb]. Similar to the bands 1 and 2 the configuration assignments have been confirmed through M1/E2 ratio measurements which will be dealt in next section.

7.3.5 Electromagnetic Transitions Strengths

In order to determine the absolute value of B(M1)and B(E2) reduced transition probabilities the nuclear lifetime measurement should be performed. The

B(M1)/B(E2) ratio however, can be extracted from the experimental γ-ray branching ratio λ of two strongly coupled bands when both quadrupole (E2) and M1/E2 transitions are observed. It can be measured through using the following relationship:

$$\frac{B(M1;I\rightarrow I-1)}{B(E2;I\rightarrow I-2)} = 0.697\frac{[E_\gamma(I\rightarrow I-2)]^5}{[E_\gamma(I\rightarrow I-1)]^3} \times \frac{1}{\lambda}\frac{1}{[1+\delta^2]}[\frac{\mu^2 N}{e^2 b^2}] \tag{7.3}$$

where the branching ratio λ is just the ratio of intensity of two competing γ-rays

$$\lambda = \frac{I_\gamma(I\rightarrow I-2)}{I_\gamma(I\rightarrow I-1)} \tag{7.4}$$

and the E_γ are measured in MeV.

Figures 7.11, 7.12,7.13 illustrate the experimental ratios of the reduced transition probabilities obtained for the different bands accompanied with theoretical estimates obtained for the given configurations which will be discussed later in this chapter. In this work, in order to measure the intensity branching ratio (the ratio of the decay probabilities for competing ΔI=2 and ΔI =1 γ-ray transitions), double or triple gated γ- ray spectra were generated and studied. The exact energy and relative intensity of the two competing ΔI=2 and ΔI =1 γ-rays can be obtained the spectra. The E2/M1 multipole mixing ratio which is typically $\ll$1 and was assumed to be zero.

To perform theoretical calculations, the semiclassical model of Dönua and Frauendorf [48, 49] has been used and the results were compared to the experimental data shown in Figures 7.11, 7.12,7.13. The parameters used in this calculation are summarised in Table 7.3. The Z/A relationship was used to extract the core's g-factor ($\approxeq$0.452) and its quadrupole moment Q_o($\approxeq$4.7 eb) was calculated from previously reported [44–46] deformation parameters (β = 0.247)

As can be seen from Fig 7.11 reasonable agreement with expected data has been obtained by the $h_{11/2}$[514]9/2 and $g_{7/2}$[402]5/2 combination which strengthens the configuration assignments made in the investigation. This configuration with K=7

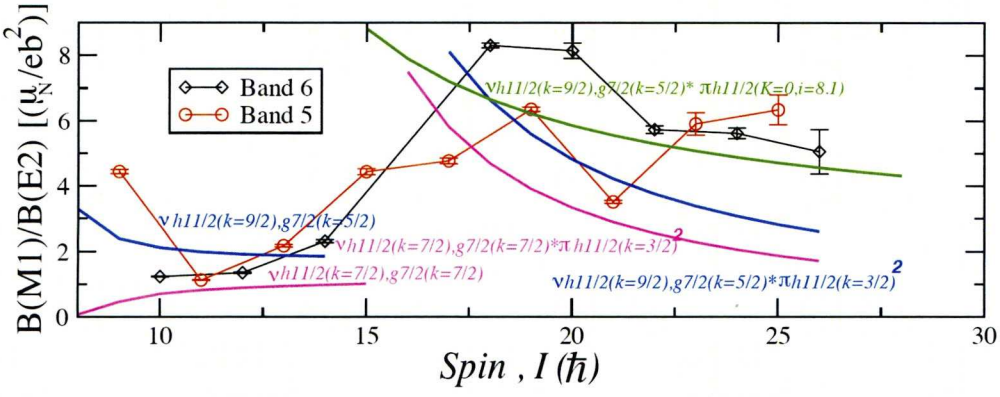

FIGURE 7.11: Experimental B(M1)/B(E2) ratios of reduced transition probabilities for the bands in ^{130}Ce. The lines show theoretical estimates obtained for the given configurations 5 and 6 in ^{130}Ce.

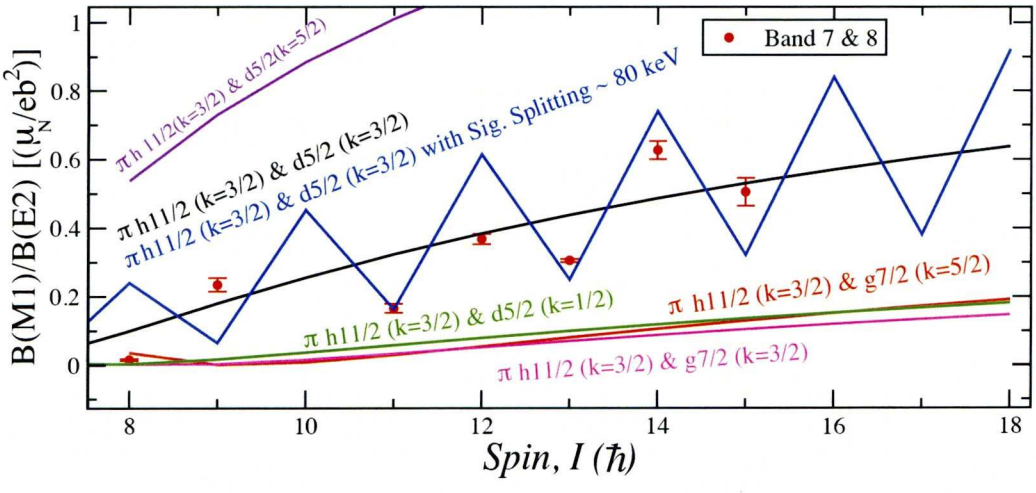

FIGURE 7.12: Experimental B(M1)/B(E2) ratios of reduced transition probabilities for the bands in ^{130}Ce. The lines show theoretical estimates obtained for the given configurations 7 and 8 in ^{130}Ce.

	Protons			Neutrons			
Nilsson State	g	i	Ω	Nilsson State	g	i	Ω
$h_{11/2}[541]3/2$	1.214	4.5	1.5	$h_{11/2}[514]9/2$	-0.209	2.5	4.5
$h_{11/2}[550]1/2$	1.214	5.5	0.5	$h_{11/2}[523]7/2$	-0.209	2.5	3.5
$d_{5/2}[422]3/2$	1.47	1.5	1.5	$g_{7/2}[402]5/2$	0.255	0.5	2.5
$g_{7/2}[550]1/2$	0.739	1.5	2.5				

TABLE 7.3: Parameters were used in B(M1)/B(E2) estimation.

is in contrary with the previous assignment made by D. M. Todd al Ref.[46]. Fig 7.11 also illustrates the estimate made for the bands after the first alignment I

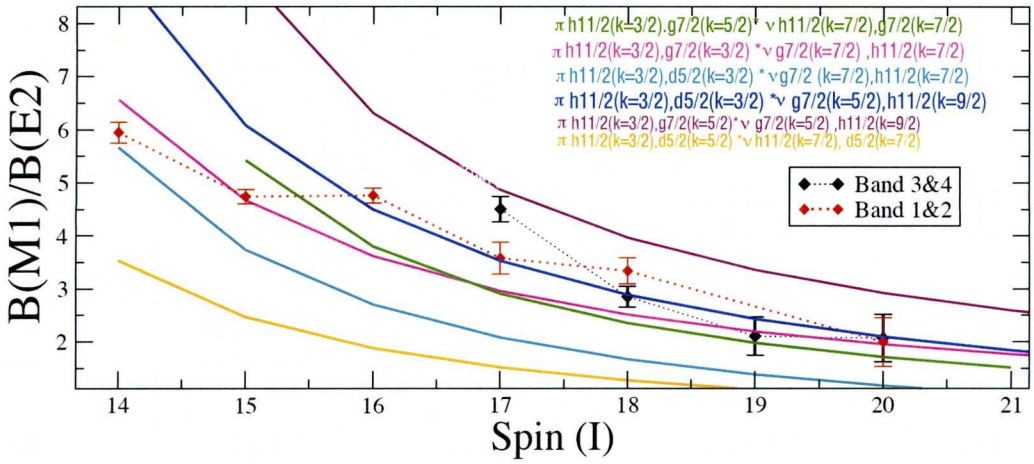

FIGURE 7.13: Experimental B(M1)/B(E2) ratios of reduced transition probabilities for the bands in ^{130}Ce. The lines show theoretical estimates obtained for the given configurations 1, 2, 3 and 4 in ^{130}Ce.

> 17). The ($\nu h_{11/2}[514]9/2$, $g_{7/2}[402]5/2 \otimes \pi h_{11/2}[541]3/2^2$) assignment has reasonably good agreement with the data, suggesting the angular momentum of the aligning particles has almost zero projection on symmetry axis. In case of bands 7 and 8(Fig7.12), the best estimate was made by $h_{11/2}[541]3/2$ and $d_{5/2}[422]3/2$ combination. Several attempts were made to include the signature splitting into the the calculation. As is shown in Fig7.12, the calculation with no signature splitting gives an overall a good result. From the routhian (Fig7.8), values of the signature splitting in the spin range 8-15$\hbar$ can be obtained and consequently, a calculation with 80 keV has been included to show the effect. In the case of newly found four-quasiparticle bands 1 - 4 the best estimate (Fig7.13) can be found in combintion of ;

$h_{11/2}[541]3/2$, $d_{5/2}[422]3/2 \otimes \nu g_{7/2}[402]5/2$, $h_{11/2}[514]9/2$ (blue line).

However one cannot rule out the possibility of other combinations such as:

$h_{11/2}[541]3/2$,$g_{7/2}[422]3/2 \otimes \nu g_{7/2}[404]7/2$,$h_{11/2}[523]7/2$(purple line) and

$h_{11/2}[541]3/2$,$g_{7/2}[402]5/2 \otimes \nu h_{11/2}[523]7/2$,$g_{7/2}[404]7/2$(green line).

E_γ (keV)	I_γ	$I_i \rightarrow I_f$	Band
742	39852(207)	$13^- \rightarrow 11^-$	5
838	15732(133)	$15^- \rightarrow 13^-$	5
771	9286(100)	$17^- \rightarrow 15^-$	5
576	6075(77)	$19^- \rightarrow 17^-$	5
696	18010(138)	$21^- \rightarrow 19^-$	5
837	16753(129)	$23^- \rightarrow 21^-$	5
968	4247(70)	$25^- \rightarrow 23^-$	5
674	45677(238)	$10^- \rightarrow 8^-$	6
805	24485(162)	$12^- \rightarrow 10^-$	6
854	11613(117)	$14^- \rightarrow 12^-$	6
628	21647(158)	$18^- \rightarrow 16^-$	6
769	2743(63)	$20^- \rightarrow 18^-$	6
905	5669(82)	$22^- \rightarrow 20^-$	6
1029	2573(56)	$24^- \rightarrow 22^-$	6
189	40934(204)	$8^- \rightarrow 7^-$	6→5
590	8851(97)	$8^- \rightarrow 8^+$	6→GSB
359	38434(200)	$10^- \rightarrow 9^-$	6→5
383	23456(157)	$11^- \rightarrow 10^-$	5→6
420	15043(124)	$12^- \rightarrow 11^-$	6→5
416	12738(120)	$13^- \rightarrow 12^-$	5→6
438	10418(108)	$14^- \rightarrow 13^-$	6→5
331	138846(385)	$15^- \rightarrow 14^-$	5→6
296	24841(161)	$17^- \rightarrow 16^-$	5→6
332	12733(123)	$18^- \rightarrow ^-$	6→5
364	70059(268)	$19^- \rightarrow 18^-$	5→6
403	11263(115)	$20^- \rightarrow 19^-$	6→5
434	21956(149)	$21^- \rightarrow 20^-$	5→6
470	11571(109)	$22^- \rightarrow 21^-$	6→5
498	7632(90)	$23^- \rightarrow 22^-$	5→6
531	3001(62)	$24^- \rightarrow 23^-$	6→5
274	45461(214)	$15^+ \rightarrow 14^+$	2→1
363	7626(115)	$17^+ \rightarrow 16^+$	1→2
232	5638(78)	$14^+ \rightarrow 13^+$	1→2
320	6333(80)	$16^+ \rightarrow 15^+$	2→1
423	6281(108)	$19^+ \rightarrow 18^+$	2→1
440	2439(49)	$20^+ \rightarrow 19^+$	1→2
682	2894(60)	$17^+ \rightarrow 15^+$	2
818	2913(68)	$19^+ \rightarrow 17^+$	2
624	3452(65)	$18^+ \rightarrow 42^+$	3
796	1177(34)	$20^+ \rightarrow 42^+$	3
292	3919(67)	$17^+ \rightarrow 16^+$	4→3

332	11407(115)	$18^+ \rightarrow 16^+$	3→4
375	4192(65)	$19^+ \rightarrow 17^+$	4→3
421	2203(49)	$20^+ \rightarrow 19^+$	3→4
547	2551(51)	$17^+ \rightarrow 15^+$	4
707	2155(48)	$19^+ \rightarrow 17^+$	4
595	2394(52)	$21^+ \rightarrow 19^+$	1
863	1997(50)	$21^+ \rightarrow 19^+$	1
436	1441(42)	$21^+ \rightarrow 19^+$	1

TABLE 7.4: Energy intensities were used in B(M1)/B(E2) calculations. The energies are in KeV and in order to measure the intensity of the transitions gates were put above the level of interest.

7.3.6 Conclusion

The level structures of the $^{130}_{58}Ce_{72}$ nucleus has been investigated and through this analysis has been extended up to higher spin. In addition four new high spin four-quasiparticle bands and two weakly populated structures have been identified. Where possible, the comparison of experimental data with cranked shell model calculations have been performed to help assign the configurations and interpret the results. In order to strengthen the configuration assignments made for different bands, the B(M1)/B(E2) ratio measurment have been performed and compared with theoretical estimates based on semi-classical formula of Dönau and Fraeundorf [48, 49].

Bibliography

[1] P. A. Pipidis. *Structural Behavior Of 157,158,159 Dy In the I = 30-50 Spin Regime and the High-Spin Domain of 158 Er up to and Above Band Termination. The Florida State University. PhD thesis,.* 2006.

[2] R.B. Firestone. *Table of Isotopes. John Wiley and Sons Inc.* 1996.

[3] E. S. Paul. *Postgraduate Lectures. Liverpool Nuclear Physics Group, unpublished.* Dec 2008.

[4] I. Ragnarsson and T. Bengtsson. *Band Crossing and Band Terminations in Rapidly Rotating Nuclei. Nuclear Physics A,*, volume A447, Pages 251-256. 1985.

[5] H.W. Cranmer-Gordon. *et al., Nuclear Physics. Nuclear Physics*, volume A465 506-528. 1987.

[6] C.F. von Weizsacker. *Z Phys*, volume 96 431. 1935.

[7] R.D. Woods and D.S. Saxon. *Physical Review*, volume 95 577. 1954.

[8] P. Ring and P. Schuck. *The Nuclear Many-Body Problem. Springer-Verlag Inc, 1980.*

[9] J.H.D. Jensen O. Haxel and H.E. Suess. *Physical Review*, volume 75, 1766. 1980.

[10] A. Bohr and B.R. Mottelson. *Nuclear Structure. W.A. Benjamin Inc, 1969.*

[11] B. Nilsson. *Nucl. Phys. A*, volume 129, 445. 1969.

[12] Selskab Mat. Fys. Medd S.G. Nilsson, K. Danske Videnskab. *Nuclear Structure. Selskab Mat. Fys. Medd*, volume 29. 1955.

[13] S. G. Nilsson et al. *Nucl. Phys. A*, volume 1, 445. 1969.

[14] V. M. Strutinsky. *Nuclear Physics*, volume A95 420. 1967.

[15] V. M. Strutinsky. *Nuclear Physics*, volume A122 1. 1968.

[16] A. Bohr and B. R. Mottelson. *Nuclear Structure, volume II, W.A. Benjamin Inc.* 1975.

[17] D. R. Inglis. *Particle Derivation of Nuclear Rotation Properties Associated with a Surface Wave. Physical Review*, volume 103, 1786-1795. 1956.

[18] D. R. Inglis. *Nuclear Moments of Inertia due to Nucleon Motion in a Rotating Well. Physical Review*, volume 103:1786-1795. 1956.

[19] R. Bengtsson and S. Frauendorf. *Quasiparticle Spectra Near the Yrast Line. Nuclear Physics A*, volume 327, 139-171. 1979.

[20] P.E. Hodgson. *Nuclear Heavy Ion Reactions. Oxford Clarendon Press.* 1978.

[21] N. Bohr. *Nature*, volume 137, 344. 1936.

[22] R. Bass. *Nuclear Reactions with Heavy Ions. Springer-Verlag Berlin.* 1980.

[23] R.M. Steffen K.S. Krane and R.M. Wheeler. *Nuclear Data Tables. Springer-Verlag Berlin*, volume A11 351. 1973.

[24] I. Y. Lee. *Nuclear Physics*, volume A520 641c. 1990.

[25] F. A. Beck P. J. Nolan and D. B. Fossan. *Nuclear Data Tables. Ann. Rev. Nucl. Part. Sci*, volume 44, 561. 1994.

[26] G.F.Knoll. *Radiation Detection and Measurement. John Wiley and Sons.* 2000.

[27] C.W. Beausang and J. Simpson. *Nuclear Data Tables. J. Physics G: Nuclear and Particle Physics*, volume 22 527. 1996.

[28] E. S. Paul. *et al., Physical Review Letter*, volume 98, 012501. 2007.

[29] E. S. Paul. *et al., The Return of Collective Rotation in 157Er and 158Er at Ultra High Spin. Phys, Rev, lett*, volume 98, 012501. 2007.

[30] A. O. Evans. *et al., High Spin Structure in 157Er up to and Above Band Termination. Physical Review C*, volume 73, 064303. 2006.

[31] A. O. Evans. *Lifetime Measurements in 112,110 Te and Band Termination and Beyond in 157 Er.,Oliver Lodge Laboratory, University of Liverpool, PhD thesis.* 2004.

[32] F. C. Stephens, M. A. Deleplanque, and R. M. Diamond. *Structure changes in ^{156}Er at high spin, Physical Review Letters*, volume 54, 2584-2587. 1985.

[33] D. C. Radford. *ESCL8R and LEVIT8R:Software for Interactive Graphical Analysis of HPGe Coincidence Data Sets.* URL `http://radware.phy.ornl.gov/rw/esclev/esclev.html`.

[34] B. Crowell M. P. Carpenter R. G. Henry R. V. F. Janssens T. L. Khoo T. Lauritsen and D. Nisius. *Background Subtraction for High -Fold Gamma-Ray Coincidence Data. Nuclear Instruments and Methods in Physics Research A*, volume 355, 575-581. 1995.

[35] K. Lagergren. Florida State University. Private communication. 2004.

[36] J. Simpson. *et al., Rotational Alignment in 158Er and 159Er. Journal of Physics G: Nuclear of Physics*, volume 10, 383-416. 1984.

[37] R. Bengtsson and S. Frauendorf. *An Interpretation of Backbending in Terms of the Crossing of the Ground State Band with an Aligned Two-Quasiparticle Band. Nuclear Physics A*, volume 314, 27-36. 1979.

[38] A. V. Afanasjev D. B. Fossan G. J. Lane and I. Ragnarsson. *Termination of Rotational Bands: Disappearance of Quantum Many Body Collectivity. Physics Reports. Physics Reports*, volume 322. 1999, 1-124.

[39] S. M. Harris. *Physical Review*, volume 138. 1965. B509.

[40] S.B. Patel. *et al. Phys. Rev. Lett*, volume 54, 62. 1986.

[41] W. D. Myers P. Moller, J. R. Nix and W. J. Swiatecki. *Atomic Data Nucl. Data Tables*, volume 59, 185. 1995.

[42] Y.S. Chen. *et al. Phys. Rev.C*, volume 28, 2437. 1983.

[43] S. Frauendorf and F. R. May. *Phys. Lett. B*, volume 125, 245. 1983.

[44] E. S. Paul. *et al., Acta. Phys. Hungary, N.S, Heavy Ion Phys.*, volume 6, 281-284. 1997.

[45] A. T. Semple. *et al., J. Phys. G*, volume 24. 1998, 1125.

[46] D. M. Todd. *et al., Acta. Phys. Hungary, N.S, Heavy Ion Phys.*, volume 10. 1984, 1407.

[47] P. J. Nolan. *et al., Ann. Rev.Nucl. Part. Sci.*, volume 44,. 1994, 561.

[48] F. Dönau and S. Frauendorf. *in Proceedings of the Conference on High Angular Momentum Properties of Nuclei, Oak Ridge, 1982, edited by N. R. Johnson (Harwood Academic, New York, 1983)*, volume p. 143. 1983.

[49] F. Dönau. *Nucl. Phys. A*, volume 471, 469. 1987.